The Viscous and Inviscid Strato-Rotational Instabilities

Luke James Montgomery Robins

Submitted in accordance with the requirements for the degree of
Doctor of Philosophy

The University of Leeds
School of Mathematics

August 2017

To my grandparents:

Nana-by-the-Seaside,

Grandad-with-the-Stick,

Nan and Grandad.

Acknowledgements

I must thank both my supervisor, Evy Kersalé, and my co-supervisor, Chris Jones. Over the course of my studies, the two of you have been consistently patient and helpful. You have both kept your doors open to me, provided regular and constructive feedback, and have never considered any of my questions to be too ridiculous to answer. I truly could not have done this work without your help.

To my family... well, Mum and Dad, I'm afraid I can only humbly apologise, once again, for pursuing the very subject whose name was banned within our household as myself and Sarah grew up. I am afraid to say that I seem to have fallen for Fluid Dynamics, despite your warnings to steer otherwise. I do hope you can forgive this act of rebellion!

I must also express my gratitude for, over the past 27 years, instilling within me the values that I use to navigate the world, inspiring my passion for astrophysics (Blame TNG!), and for teaching me to look at the world with an analytic, critical eye. You have supported me every step of the way, and for that I am immeasurably grateful.

To my sister Sarah and brother-in-law Lyle, I must thank you both for multiple occasions of surviving zombies, mining diamonds, and battling with titans online. Those activities were some of the many ways that I managed to remain sane during the past few years! It was also my honour to (twice!) be the Master of Ceremonies for the wedding celebrations between the two of you last year.

To my friends, including those of you whom I knew before I started this PhD, and all those who I met during it... well, what can I say? From BSG-games, to shared-workspace days; coffee meet-ups discussing maths, society, religion, free will, quantum physics, and everything in-between; from RPG-nights, to conversations providing support when I needed it. You have, each of you, helped make the person that I am today, and I value you all.

Finally, I would like to thank the Science and Technologies Facilities Council (STFC), without whose generous funding this work could not have happened.

Abstract

Using computational and analytical methods, we investigate the viscous and inviscid forms of the Strato-Rotational Instability (SRI) for the stratified Taylor-Couette system.

We use an eigenfunction solver to find instability modes. We are able to vary the stratification, radius ratio η and rotation-rate ratio μ, and optimise the Reynolds number and relevant wavenumbers.

We investigate the viscous and inviscid stability limits, extending the range of instability compared to prior results. Our results are consistent with the findings of Yavneh et al. [2001], Shalybkov and Rüdiger [2005], Le Bars and Le Gal [2007], Rüdiger and Shalybkov [2009], and Ibanez et al. [2016].

Building upon the results of Park and Billant [2013], we demonstrate that the $\mu < 1$ inviscid system is unconditionally unstable if the buoyancy frequency is more than twice the inner cylinder rotation rate. For any given weaker stratification, we provide sufficient conditions for instability upon η and μ.

We explore the structure of the SRI's critical mode throughout the $[\eta, \mu]$-parameter space, for fixed stratification. The considerable variation in structural appearance suggests that various instability mechanisms exist. We also find closed domain loops, for which the SRI becomes unstable for only a finite range of Reynolds numbers. This phenomenon is associated with a discontinuous change in the critical mode within the $[\eta, \mu]$-parameter space. We find considerable differences between the viscous and inviscid systems, including a region of the parameter space which for weak stratifications is only unstable in the presence of viscosity.

For the SRI to persist as a critical mode in the narrow-gap limit, we show that a near-solid-body-rotation limit is also necessary. This leads to the rotating stratified shear flow system described by Yavneh et al. [2001] for inviscid flows.

Contents

List of figures

List of tables

Chapter 1

Introduction

Astrophysical discs are, broadly speaking, any astrophysical object in a disc shape. These range from the rings around planets such as Saturn, up to disc-shaped galaxies such as the Milky Way. Astrophysical discs typically have some sort of central massive object, such as a planet, a star or a black hole.

In the case of accretion discs, matter is steadily moving radially inwards through the disc towards the central object. Such discs typically have a similar scale to the size of our solar system, and are generally made up of a gaseous fluid. Examples of accretion discs include protoplanetary discs around young stars, or the case of matter being steadily drawn in and consumed by a black hole. It is also a suggested mechanism behind a type 1a supernova, known as the single-degenerate model. This involves a large companion star orbited by a smaller and more dense white-dwarf star. Gas from the outer layers of the companion star is accreted onto the white-dwarf, with an accretion disc forming around the white-dwarf. Once the white-dwarf reaches critical mass, the increased gravitational pressure re-ignites fusion reactions within the white-dwarf star, triggering a supernova [Hillebrandt and Niemeyer, 2000].

Accretion discs require radially outward angular momentum transport to account for inward mass transport. However, accretion discs have been observed to exhibit stronger angular momentum transport than their expected viscosity can account for. This discrepancy can be explained if astrophysical discs can be shown to be turbulent, which would significantly increase their effective viscosity. However, astrophysical discs follow Keplerian rotation profiles, which are centrifugally stable to axisymmetric perturbations. The astrophysical fluids community is therefore interested in any mechanisms that can produce linear instabilities within centrifugally stable flows.

Many of these accretion flows can be made turbulent via the Magneto-Rotational Instability (MRI) [Balbus and Hawley, 1991] [Velikhov, 1959]. However, the MRI relies upon the presence of ionised fluid flow, which is not expected in all cases.

One instability of interest is the Strato-Rotational Instability (SRI), first described by Yavneh et al. [2001] for the Taylor-Couette system. The majority of prior research on the SRI has looked at the inviscid system, however viscous analyses and direct experiments have also been performed.

1.1 The Taylor-Couette system

Taylor-Couette fluid flow [Taylor, 1923] consists of two tall concentric cylinders with different radii. The gap between the cylinders is filled with fluid, and the cylinders themselves are rotated at distinct angular velocities to stimulate the flow. (See Figure 1.1.)

The unstratified flow is very well understood, and can be tested in laboratory conditions. This makes Taylor-Couette flow useful for the purposes of investigating rotational instabilities, such as those that an astrophysical disc may be susceptible to.

We work in cylindrical co-ordinates $[\hat{r}, \hat{\theta}, \hat{z}]$ with the $\hat{z}$-axis aligned with the central axis of the cylinders. (The notation $\hat{a}$ is used to denote that these terms are dimensional.) The radii of the inner and outer cylinders are denoted by $\hat{r}_{\text{in}}$ and $\hat{r}_{\text{out}}$, and the appropriate angular velocities are denoted by $\hat{\Omega}_{\text{in}}$ and $\hat{\Omega}_{\text{out}}$. For the purposes of this analysis, it is assumed that the cylinders are infinitely tall.

We define the following dimensionless ratios:

$$\eta = \frac{\hat{r}_{\text{in}}}{\hat{r}_{\text{out}}}, \quad \mu = \frac{\hat{\Omega}_{\text{out}}}{\hat{\Omega}_{\text{in}}}. \tag{1.1}$$

By construction, $0 < \eta < 1$, with small values of η corresponding to an experimental set-up with a wide-gap width, and $\eta \simeq 1$ corresponding to a narrow-gap width.

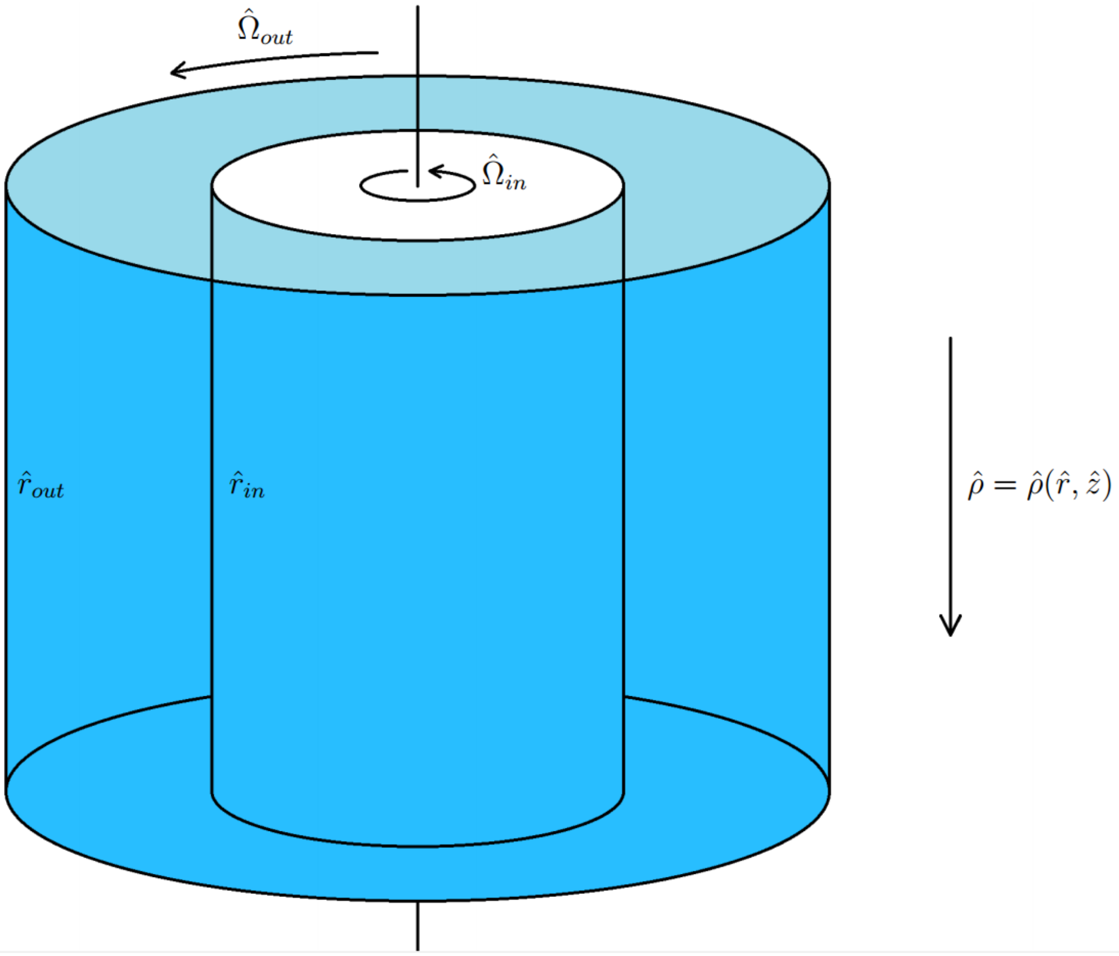

Figure 1.1: The Taylor-Couette experiment. The gap between two concentric cylinders is filled with fluid, and the cylinders are rotated at different rates. The inner cylinder has radius $\hat{r}_{\text{in}}$ and angular velocity $\hat{\Omega}_{\text{in}}$; the outer cylinder has radius $\hat{r}_{\text{out}}$ and angular velocity $\hat{\Omega}_{\text{out}}$. Stratification $\hat{\rho}$ could be the result of an imposed temperature gradient, or from varying concentrations of a solute. It is primarily vertical in nature, increasing as $\hat{z}$ decreases, with a weak radial dependence.

The ratio μ is unconstrained and can take any value, with negative values representing counter-rotation and positive values representing co-rotation. Throughout this work we will primarily be considering the case $0 \leq \mu \leq 1$. The case of $\mu = 0$ corresponds to the case where the outer cylinder is stationary, whereas $\mu = 1$ corresponds to the case where the two cylinders have the same rate of rotation, which is also known as solid-body rotation.

We define the Reynolds number:

$$Re = \frac{\hat{r}_{\text{in}}\hat{\Omega}_{\text{in}}\left(\hat{r}_{\text{out}} - \hat{r}_{\text{in}}\right)}{\hat{\nu}}. \tag{1.2}$$

This can be considered to be a non-dimensional ratio between the rotation of the inner cylinder against the viscosity of the system $\hat{\nu}$. Higher Reynolds numbers correspond to higher input rotations or lower viscosities, and the inviscid limit of $\hat{\nu} \to 0$ can also be considered to be the limit of $Re \to \infty$. Therefore, if a system is unstable in the inviscid limit, it is typically also unstable for sufficiently large Reynolds numbers.

Finally, we have the vertical stratification of the system, measured in terms of the vertical buoyancy frequency $\hat{N}$. The larger the buoyancy frequency, the stronger the stratification. A related term is the dimensionless Froude number, which is defined as $Fr = \hat{\Omega}_{\text{in}}/\hat{N}$. For further details on the stratification, buoyancy frequency and Froude Number see section 2.2.6.

The unstratified Taylor-Couette system is well understood (see e.g. Andereck et al. [1986]). It is known to have an axisymmetric centrifugal instability for flows with $\mu < \eta^2$. In the case of $\mu < 0$, non-axisymmetric instabilities can also dominate over the axisymmetric mode. However, the unstratified system is known to be stable for $\mu \geq \eta^2$, which includes the domain of Keplerian flows such as accretion discs.

1.2 Inviscid research

Kushner et al. [1998] discussed the existence of a Kelvin wave instability in a rotating inviscid stratified semi-geostrophic channel flow. Here Kelvin waves are transverse waves within a rotating flow which travel adjacent to a boundary. They are driven by both a vertical restoring force, such as buoyancy, and by the Coriolis force from the rotation of the system.

Yavneh et al. [2001] extended this result to inviscid stratified Taylor-Couette flow. Their results suggested that centrifugally stable flows could be destabilised by the presence of a stable stratification, suggesting a larger domain of instability than had been considered previously. The instability, which would come to be known as the strato-rotational instability, was non-axisymmetric in nature. Working with narrow gaps, Yavneh et al suggested that a sufficient condition for instability was for $d\Omega^2/dr < 0$ to occur at any point in the flow, i.e. any $\mu < 1$, provided that moderate to strong stratification was present ($|Fr| \ll 1$). They also concluded that the instability mechanism was driven by shear-modified Kelvin waves.

Considering the potential astrophysical applications, Dubrulle et al. [2005] examined the energy integral for stratified Taylor-Couette flow, and derived a sufficient condition for stability given periodic, stress-free, or rigid boundary conditions. The energy integral is a quantity representing the sum of all the kinetic and potential energy in a system. Here periodic boundary conditions require that flow properties adjacent to one boundary be equal to those adjacent to the opposite boundary. Stress-free boundary conditions require that there be zero gradient for velocities at the boundary. Rigid boundary conditions require for inviscid systems that there be no flow through the boundary, and are used in this thesis in section 2.2.7. Dubrulle et al. [2005] introduced the idea of using WKBJ analysis on the SRI, which was subsequently further developed by Le Dizès and Riedinger [2010] and Park and Billant [2013].

Brandenburg and Dintrans [2006] considered non-axisymmetric perturbations in stratified shearing sheet disc flow with periodic boundary conditions. The shearing sheet approximation considers a small section of a rotating flow, such that length-scales within this section are much smaller than the radial distance to the axis of rotation. The shearing sheet system is also known as the rotating shear flow system, which is discussed in detail in section 7.3 of this thesis. Using an eigenfunction analysis, they concluded that the SRI was absent in this context, further concluding that the SRI must be a global instability not a local instability. This implied that the boundary conditions always play a significant role in the SRI.

Also using a large shearing sheet model, Umurhan [2006] investigated the effects of vertically varying the buoyancy frequency of the inviscid system, such that $\hat{N} = \hat{N}(z)$. It was shown that the SRI persists in this case, provided that rigid boundary conditions are used. The instability structure was largely unchanged by the presence of vertically varying stratification.

Performing energy analysis of the rotating shear flow system, Vanneste and Yavneh [2007] found that when the inviscid system is rapidly rotating and strongly stratified, then it is unconditionally unstable with a growth rate exponentially dependent on the Rossby number.

For the inviscid Taylor-Couette system, Normand [2010] found that as μ increases for $\mu < 1$, then the band of unstable vertical wavenumbers decreases in width and moves to larger values. During this analysis, an inviscid dispersion relation for the SRI was derived.

Performing WKBJ analysis, Park and Billant [2013] concluded that the Taylor-Couette system could always be made inviscidly unstable with a suitable choice of stratification $\hat{N}$, so long as the system was not in solid body rotation, i.e. $\mu \neq 1$. This result significantly extended the domain of inviscid instability for the SRI.

1.2.1 Radiative Instability

Le Dizès and Billant [2009] performed WKBJ analysis on the stability of a columnar vortex in an inviscid stratified fluid, drawing attention to an unstable mode which radiated energy radially away from the vortex. Le Dizès and Riedinger [2010] further showed that this Radiative Instability (RI) could also arise in the wide gap limit of potential flow in the stratified Taylor-Couette system. Potential flow is here defined as any flow for which $\mu = \eta^2$, i.e. any flow that exists just at the point of centrifugal stability, along the stability line for axisymmetric instabilities. The SRI continuously morphs to become the RI as the wide-gap limit is approached. Comparing different gap widths, Le Dizès and Riedinger [2010] showed that the RI is present for a much larger range of vertical wavenumbers than the SRI.

Riedinger et al. [2011] experimentally confirmed the existence of the radiative instability, using a wide tank of stratified fluid with a spinning cylinder in the centre. Various cylinder sizes were used, and the experimental results were found to be in good agreement with the theory. The RI was also found for linear analysis of viscous Taylor-Couette flows with a finite gap width by Leclercq et al. [2016], although only for flows that were already unstable to the SRI.

1.3 Viscous research

The viscous SRI was originally investigated by both Yavneh et al. [2001] and Molemaker et al. [2001], who numerically verified that the SRI persisted in the presence of weak viscosity for near narrow-gap flows.

Shalybkov and Rüdiger [2005] demonstrated the necessity of a centrifugal approximation to allow for purely vertical stratification in the context of stratified Taylor-Couette flow. This centrifugal approximation required that the gravitational force be significantly stronger than any centrifugal forces that were exerted upon the flow. Shalybkov and Rüdiger [2005] also performed numerical analyses to find the critical Reynolds number for a range of rotation ratios for both $\eta = 0.78$ and $\eta = 0.3$, with a Froude number of $Fr = \hat{\Omega}_{\text{in}}/\hat{N} = 0.5$. From these numerical simulations, they concluded that $\mu \simeq \eta$ appeared to be the stability limit, rather than $\mu < 1$ as suggested by Yavneh et al. [2001], as the critical Reynolds number was seen to sharply increase as μ approached the value of η.

Gellert and Rüdiger [2009] used fully 3-dimensional nonlinear viscous simulations of Taylor-Couette flows to argue that a heat stratification could be used in physical experiments of the SRI rather than a solute density stratification. They also noted that all experimental investigations would be limited by issues relating to the physical aspect ratio of the cylinders. This is primarily because theoretical analyses of the SRI typically assume that the perturbation is periodic and unbounded in the vertical direction. However experiments have physical end-boundaries, which restrict the choice of vertical wavenumbers.

Rüdiger and Shalybkov [2009] investigated the influence of magnetic fields on the SRI for ionised Taylor-Couette flows. They concluded that stratification appears to stabilise both the classical axisymmetric Taylor instability and the MRI, increasing the critical Reynolds number in both cases. They noted that magnetic effects amplified the SRI when the magnetic Prandtl number $Pm > 1$, and that it suppressed the SRI when $Pm < 1$. They also noticed that the previously suggested $\mu = \eta$ stability limit could in fact be surpassed for sufficiently high Reynolds numbers, regardless of the presence or absence of magnetic fields.

Rüdiger et al. [2017] performed numerical simulations of Taylor-Couette flows for $\eta = 0.52$, and identified that the SRI appeared to only be present for a range of Froude numbers such that $Fr_{min} < Fr < Fr_{max}$, with $Fr_{min} \simeq 0.3$ and $Fr_{max} \simeq 5.5$. They also discussed the dependence of wavenumbers on the Froude number and Reynolds number.

Leclercq et al. [2016] numerically examined the linear instabilities of the viscous stratified Taylor-Couette system for a range $\mu < 1$ and a large range of Reynolds numbers. Various values of η and of the stratification $\hat{N}$ were used. Although the domain of viscous instability was not extended by their results, they identified the modes of instability with the strongest growth rates beyond the point of marginal stability.

1.4 Experimental analysis

The SRI was first tested experimentally by Le Bars and Le Gal [2007], using a salt stratification and a radius ratio of $\eta = 0.8$ and a Froude number of $Fr = 0.5$. They found good agreement with the results of Shalybkov and Rüdiger [2005], validating that the SRI was capable of crossing the Rayleigh line.

Ibanez et al. [2016] also used a salt stratification experiment, but used sodium polytungstate salt rather than sodium chloride, allowing for a significantly larger density differential and therefore a taller experiment, permitting large vertical wavelengths. They used a radius ratio of $\eta = 0.877$, and various fixed values of the buoyancy frequency N. The experiment was performed by starting the system in solid body rotation and bringing it up to specific Reynolds numbers, then decreasing μ by reducing the outer-rotation rate. The value of μ where the system became unstable would be noted for each Reynolds number.

They showed that, for given values of μ, the SRI can sometimes require a finite range of Reynolds numbers to be unstable, i.e. flows can stabilise at large values of Re. This suggests that in some regions of the parameter space the SRI may be viscously unstable but inviscidly stable. A non-axially-periodic mixing instability was also discovered for high Reynolds numbers close to the Rayleigh line of $\mu = \eta^2$.

It should be noted that the experimental set up of Ibanez et al. [2016] did in some cases violate the centrifugal assumption that Shalybkov and Rüdiger [2005] drew attention to, implying the stratification may not have always been purely vertical in this experiment (See section 5.3). Interestingly the SRI was still seen in these circumstances, implying that the centrifugal assumption may not be vital for the existence of the SRI.

Rüdiger et al. [2017] performed an experimental analysis of the SRI in addition to their numerical exploration of the viscous system. This particular experimental analysis is of interest since it utilised a heat stratification rather than a direct density stratification, as originally suggested in Gellert and Rüdiger [2009]. Their experimental analysis was mostly used to check their numerical results, for which they saw a good correlation.

1.5 This Thesis

As we have described, there have been two primary strands to SRI research: the inviscid and viscous approaches. Mostly these have been separate lines of research, and one aim of this thesis is to reconcile these two approaches.

In the course of the research we established that the SRI takes significantly different forms in different parts of the parameter space, and we have analysed and investigated these within the thesis.

In chapter 2 of this thesis, we describe the system of perturbation equations which describe the SRI, and a few common limits of the system. In chapter 3, we describe the computational algorithms used to find solutions to the SRI perturbation equations. In chapter 4, we explore the stability limit of the SRI for various strengths of stratification, and derive that the inviscid system with non-solid-body-rotation is unconditionally unstable for $Fr < 0.5$. In chapter 5, we provide an in-depth review of prior experimental results for the SRI. In chapter 6, we explore how the SRI instability mode changes as the radius ratio and rotation-rate ratio are varied. In chapter 7, we investigate where the critical mode of instability changes from an axisymmetric mode to a non-axisymmetric mode, and describe how the near-solid-body narrow-gap limit of the SRI is mathematically equivalent to a system of stratified rotating shear flow. In chapter 8, we present our conclusions.

Chapter 2

The Equations of the Strato-Rotational Instability

2.1 Non-dimensionalisation of the Taylor-Couette system

The structure of the stratified Taylor-Couette system is described in detail in section 1.1 and shown in figure 1.1.

To express the system in dimensionless units, we use the gap width between the cylinders, $\hat{\lambda} = \hat{r}_{\text{out}} - \hat{r}_{\text{in}}$, as our length-scale and the reciprocal of the inner rotation rate, $\hat{\tau} = 1/\hat{\Omega}_{\text{in}}$ as our time-scale. We shall use these units throughout this work, although section 2.6 discusses several alternative choices of units.

We will be measuring the density in terms of a constant reference density $\hat{\rho}_q$. This means that our pressure will be measured in units of $\hat{P}_q = \hat{\rho}_q \hat{\lambda}^2 \hat{\Omega}_{\text{in}}^2$.

We define the following dimensionless terms $[r_1, r_2, \Omega_1, \Omega_2]$ such that $\hat{r}_{\text{in}} = r_1 \hat{\lambda}$, $\hat{r}_{\text{out}} = r_2 \hat{\lambda}$, $\hat{\Omega}_{\text{in}} = \Omega_1/\hat{\tau}$, and $\hat{\Omega}_{\text{out}} = \hat{\Omega}_2/\hat{\tau}$. We can make use of the ratios η and μ to express these as:

$$r_1 = \frac{\eta}{1-\eta}, \quad r_2 = \frac{1}{1-\eta}, \quad \Omega_1 = 1, \quad \Omega_2 = \mu. \tag{2.1}$$

The Reynolds number Re (1.2) is also a non-dimensional measure of the system. We repeat the definition here for ease of reading:

$$Re = \frac{\hat{r}_{\text{in}}\hat{\Omega}_{\text{in}}\left(\hat{r}_{\text{out}} - \hat{r}_{\text{in}}\right)}{\hat{\nu}}.$$

We also define the dimensionless gravitational term g such that $\hat{g} = g\lambda\tau^{-2}$, where $\hat{g}$ is the acceleration due to gravity (equal to $9.81ms^{-2}$ in SI units on Earth). We shall see later that the non-dimensional gravity g is related to the buoyancy frequency of the stratification of the system (section 2.2.6).

We now make the transition to dimensionless co-ordinates $[r, \theta, z]$, using the following transformations:

$$\hat{r} = r\hat{\lambda}, \quad \hat{\theta} = \theta, \quad \hat{z} = z\hat{\lambda}. \tag{2.2}$$

2.2 System equations

2.2.1 The Navier-Stokes equations

Applying our non-dimensional terms with the three-dimensional Navier-Stokes equation, we have:

$$\frac{\partial \boldsymbol{u}}{\partial t} + \boldsymbol{u}.\boldsymbol{\nabla}\boldsymbol{u} = -\frac{1}{\rho}\boldsymbol{\nabla}P - \boldsymbol{g} + \frac{\eta}{(1-\eta)}\frac{1}{Re}\nabla^2\boldsymbol{u}, \tag{2.3}$$

Here $\boldsymbol{u} = [u, v, w]$ is the flow velocity, ρ is the fluid density, P is the pressure and $\boldsymbol{g} = g\boldsymbol{e_z}$ is the acceleration due to gravity. All terms are non-dimensional.

2.2.2 Incompressible flow

For simplicity, we make the assumption that the flow is incompressible:

$$\boldsymbol{\nabla}.\boldsymbol{u} = 0. \tag{2.4}$$

2.2.3 The Mass Conservation equation

Since we are including stratification in the system, the density is not necessarily constant with regards to location. This means that we must also consider the mass conservation equation:

$$\frac{\partial \rho}{\partial t} + \boldsymbol{\nabla .} \left(\rho \boldsymbol{u} \right) = 0.$$

Expanding out the second term and applying (2.4) allows us to write the mass conservation equation as:

$$\frac{\partial \rho}{\partial t} + \boldsymbol{u.\nabla} \rho = 0. \tag{2.5}$$

It is important to note the difference in meaning between equations (2.4) and (2.5), and to consider the implications of including both equations.

The incompressible equation (2.4), also known as the divergence free equation, means fluid elements cannot change their volume; they cannot be compressed or stretched. Therefore the density of an individual fluid element is unchanging. This is an approximation since in the real world fluid elements can change their own volume, however we are assuming that we are dealing with a fluid with very small compressibility.

The presence of density gradients means that distinct fluid elements will have distinct densities, dependent on initial location. This requires that we apply the mass conservation equation, (2.5), since the mass within a region can be changed by the flow of fluid elements through that region. Note that we also neglect any diffusion of density in the fluid. Diffusion will occur in real fluids, but on a significantly longer time-scale than is relevant to the SRI.

Overall, the combination of equations (2.4) and (2.5) means that, although the density of a specific fluid element cannot change, there are different fluid elements present with different densities. Therefore the density at a specific point can be changed, dependent upon the flow pattern.

Temperature gradient

The stratification can be understood in terms of a temperature gradient rather than a density gradient. Assuming a weak temperature gradient and taking the Boussinesq approximation (see section 2.2.5), we can write:

$$\rho = \rho_q \left[1 - \alpha \left(T - T_q \right) \right].$$

$$\therefore T = T_q \left[1 - \beta \left(\rho - \rho_q\right)\right]. \tag{2.6}$$

Here ρ_q and T_q are known density and temperature values at some reference location. The coefficient of volume expansion, α, is assumed to be very small, (for water with $\hat{T}_q = 293$ K and $\hat{\rho}_q = 998$ kg m^{-3}, then $\hat{\alpha} \simeq 2.1 \times 10^{-4}$ K^{-1} (appendix 1(c) of Batchelor [1991]), and we have defined $\beta = 1/\alpha\rho_q T_q$.

Assuming conservation of temperature within a single fluid element (i.e., we're working on time-scales much shorter than that of heat exchange):

$$\frac{\partial T}{\partial t} + \boldsymbol{\nabla}\boldsymbol{.}\left(T\boldsymbol{u}\right) = 0. \tag{2.7}$$

Substituting equation (2.6) into (2.7), with some simplification, brings us back to equation (2.5). Hence (2.5) can be considered to be an expression of the Boussinesq temperature equation.

2.2.4 Centrifugal approximation

We ultimately wish to consider a system with constant vertical stratification and an azimuthal basic state flow which only depends on the radius, i.e. a basic state of the form: $\boldsymbol{u_0} = r\Omega\boldsymbol{e_\theta}$ with $\Omega = \Omega(r)$. (See section 2.3.)

Consider the three-dimensional Navier-Stokes equation (2.3). Substituting in the above proposed basic state yields the following set of conditions on the basic state pressure P_0 and basic state density ρ_0:

$$\frac{\partial P_0}{\partial r} = \rho_0 r\Omega^2, \quad \frac{\partial P_0}{\partial \theta} = 0, \quad \frac{\partial P_0}{\partial z} = -\rho_0 g. \tag{2.8}$$

Note that the first and last of these equations can be combined by deriving $\partial_r\partial_z P_0$:

$$\begin{aligned} \frac{\partial^2 P_0}{\partial r \partial z} &= r\Omega^2 \frac{\partial \rho_0}{\partial z} = -g\frac{\partial \rho_0}{\partial r}, \\ \implies r\Omega^2 \frac{\partial \rho_0}{\partial z} &+ g\frac{\partial \rho_0}{\partial r} = 0. \end{aligned} \tag{2.9}$$

Consider the case of purely vertical stratification, i.e. $\partial_r\rho_0 = 0$. In this case, equation (2.9) would tell us that either there is no flow, $\Omega(r) = 0$, or that there is no stratification,

$\partial_z \rho_0 = 0$. Equation (2.9) therefore tells us that the system cannot be considered to have purely vertical stratification in combination with a purely azimuthal basic state flow $\boldsymbol{u_0} = r\Omega \boldsymbol{e_\theta}$. However, we can consider the following limit:

$$\frac{|r\Omega^2|}{g} \ll 1. \tag{2.10}$$

In this limit, we have $\partial_r \rho_0 \ll \partial_z \rho_0$, and can therefore treat the radial stratification as negligible. Note that, from (2.8), this assumption is equivalent to $\partial_r P_0 \ll \partial_z P_0$.

The requirement of this approximation was originally noted by Shalybkov and Rüdiger [2005]. The same argument holds for the dimensional system, and hence the approximation can be expressed as:

$$\frac{\left|\hat{r}\hat{\Omega}^2\right|}{\hat{g}} \ll 1.$$

2.2.5 The Boussinesq approximation

We make the assumption that throughout the flow, the density ρ is approximately equal to a constant average background density $\bar{\rho}$. We also make the assumption that the pressure P is approximately equal to a background pressure $\bar{P}(z)$ which balances the gravitational force of the background density. This can be expressed as:

$$\begin{aligned} \rho(r,\theta,z,t) = \bar{\rho} + \rho'(r,\theta,z,t), \quad |\rho'| \ll \bar{\rho}, \\ P(r,\theta,z,t) = \bar{P}(z) + P'(r,\theta,z,t), \quad |P'| \ll \bar{P}, \\ \frac{d\bar{P}}{dz} + \bar{\rho} g = 0. \end{aligned} \tag{2.11}$$

Here ρ' and P' are small perturbations to the background state, which account for the stratification and any pressures of the basic state. Note that in making these assumptions, we have intrinsically included the centrifugal assumption (section 2.2.4) by setting up a system in which $\partial_r P \ll \partial_z P$.

Consider the term $S = [-(1/\rho)\boldsymbol{\nabla} P - \boldsymbol{g}]$ from the Navier-Stokes equation (2.3). Substituting in ρ and P from (2.11) allows us to express S as follows:

$$S = \frac{-1}{\bar{\rho} + \rho'} \left[\frac{\partial \bar{P}}{\partial z} \boldsymbol{e_z} + \boldsymbol{\nabla} P' + \bar{\rho} \boldsymbol{g} + \rho' \boldsymbol{g} \right],$$

$$\implies S \simeq \frac{-1}{\bar{\rho}} \left[\boldsymbol{\nabla} P' + \rho' \boldsymbol{g} \right].$$

To simplify this, we can choose our density-scale $\hat{\rho}_q$ such that $\bar{\rho} = 1$. This yields the Boussinesq Navier-Stokes equation as follows:

$$\frac{\partial \boldsymbol{u}}{\partial t} + \boldsymbol{u} . \boldsymbol{\nabla} \boldsymbol{u} = -\boldsymbol{\nabla} P' - \rho' \boldsymbol{g} + \frac{\eta}{(1-\eta)} \frac{1}{Re} \nabla^2 \boldsymbol{u}. \tag{2.12}$$

Since the mass conservation equation only includes gradient terms of the density, it is unaffected by the Boussinesq Approximation save for exchanging ρ for ρ':

$$\frac{\partial \rho'}{\partial t} + \boldsymbol{u} . \boldsymbol{\nabla} \rho' = 0. \tag{2.13}$$

2.2.6 The Buoyancy Frequency

Consider a vertically stratified fluid with density $\hat{\rho} = \hat{\rho}(\hat{z})$, with gravitational forces balanced by some background pressure. If a fluid parcel is initially at some $\hat{z} = \hat{z}_0$ and is vertically displaced by a small perturbation $|\hat{z}_1| \ll |\hat{z}_0|$, then we can deduce the following equation of motion:

$$\hat{\rho}(\hat{z}_0) \frac{d^2 \hat{z}_1}{d\hat{t}^2} = \hat{g} \hat{\rho} \left(\hat{z}_0 + \hat{z}_1 \right) - \hat{g} \hat{\rho} \left(\hat{z}_0 \right).$$

The force here is a result of the imbalance of pressure and gravity upon the fluid parcel. We approximate that $\hat{z}_1 (d\hat{\rho}/d\hat{z}) \simeq \hat{\rho} \left(\hat{z}_0 + \hat{z}_1 \right) - \hat{\rho} \left(\hat{z}_0 + \hat{z}_1 \right)$, which is true in the limit $\hat{z}_0 \to 0$ and is also true for any linear stratification with constant $d\hat{\rho}/d\hat{z}$. This allows us to express the equation of motion as the following differential equation:

$$\frac{d^2 \hat{z}_1}{d\hat{t}^2} = -\frac{\hat{g}}{\hat{\rho}_0} \frac{d\hat{\rho}}{d\hat{z}} \hat{z}_1.$$

We have the following oscillatory solution: $\hat{z}_1 = \hat{Z} \exp \left[\pm i \hat{N} \hat{t} \right]$. Here $\hat{Z}$ is an arbitrary amplitude, and we have defined the buoyancy frequency $\hat{N}$ with the following formula:

$$\hat{N} = \sqrt{-\frac{\hat{g}}{\hat{\rho}_0} \frac{d\hat{\rho}_0}{d\hat{z}}}. \tag{2.14}$$

The buoyancy frequency is therefore the frequency of oscillation of a vertically displaced fluid element for stable stratification. If $d\hat{\rho}/d\hat{z} > 0$, then $\hat{N}$ is imaginary and the system instead permits exponentially growing solutions and is therefore unstable. For stable stratifications $\hat{N}$ is real and can be considered to be a measure of the stratification, since the stronger the stratification, the faster the rate of oscillation.

Applying our choice of length-scale $\hat{\lambda}$, time-scale $\hat{\tau}$, and density-scale $\hat{\rho}_q$, we have:

$$N = \hat{N}\hat{\tau} = \frac{\hat{N}}{\hat{\Omega}_{\text{in}}} = \frac{1}{Fr}.$$

Here we have defined the Froude number Fr, which is a dimensionless ratio of the inner rotation rate and the buoyancy frequency. It is important to note that, in our choice of units, the Froude number Fr is the reciprocal of the dimensionless buoyancy frequency. Prior research papers on the SRI have varied over whether N or Fr is used. Throughout this thesis we will be using N, except for when comparing to the work of others.

From the Boussinesq approximation earlier (see section 2.2.5), we have restricted ourselves to density distributions for which the following applies:

$$\rho = 1 + \rho', \quad |\rho'| \ll 1.$$

(Remember that we chose $\hat{\rho}_q$ such that $\bar{\rho} = 1$.)

We therefore make the approximation that $g/\rho_0 \simeq g$, which gives us:

$$N = \sqrt{-g\frac{d\rho_0'}{dz}}. \tag{2.15}$$

This now allows us to express the dimensionless gravitational acceleration g as:

$$g = -N^2\left(\frac{d\rho_0'}{dz}\right)^{-1}. \tag{2.16}$$

For simplicity, we restrict our analysis to the cases where $d\rho_0'/dz$, N and Fr are all constant.

2.2.7 Summary and Boundary Conditions

We have the following Boussinesq system of equations (2.12), (2.13) and (2.4):

$$\frac{\partial \boldsymbol{u}}{\partial t} + \boldsymbol{u}.\boldsymbol{\nabla}\boldsymbol{u} = -\boldsymbol{\nabla}P' - \rho'\boldsymbol{g} + \frac{\eta}{(1-\eta)}\frac{1}{Re}\nabla^2\boldsymbol{u},$$

$$\frac{\partial \rho'}{\partial t} + \boldsymbol{u}\boldsymbol{.}\boldsymbol{\nabla}\rho' = 0,$$

$$\boldsymbol{\nabla}\boldsymbol{.}\boldsymbol{u} = 0.$$

We require six boundary conditions, as the combination of (2.12) with (2.4) is a sixth order system [Chandrasekhar, 1961], and this is unchanged by the inclusion of (2.13).

The boundaries of Taylor-Couette flow are at the walls of the two cylinders, $r = r_1$ and $r = r_2$. The flow cannot pass through these walls.

The flow is also viscous and therefore must obey non-slip boundary conditions; i.e. the flow directly adjacent to a boundary must have the same velocity as that boundary. These velocities are known since we have $\Omega_1 = 1$ and $\Omega_2 = \mu$.

We can therefore formulate these boundary conditions as:

$$\boldsymbol{u}\left(r_1\right) = r_1\Omega_1\boldsymbol{e_\theta} = \frac{\eta}{1-\eta}\boldsymbol{e_\theta}, \quad \boldsymbol{u}\left(r_2\right) = r_2\Omega_2\boldsymbol{e_\theta} = \frac{\mu}{1-\eta}\boldsymbol{e_\theta}. \tag{2.17}$$

Resolving this in all three dimensions provides six boundary conditions, as required.

2.3 Basic State

We desire a basic state flow that satisfies the system of equations (2.12), (2.13) and (2.4). Substituting in a flow of the form $\boldsymbol{u_0} = [0, r\Omega(r), 0]$ yields the following system:

(We have used the subscript 0 to denote basic state terms:)

$$\frac{\partial P_0'}{\partial r} = r\Omega^2, \tag{2.18}$$

$$\frac{1}{r}\frac{\partial P_0'}{\partial \theta} = \frac{\eta}{(1-\eta)}\frac{1}{Re}\left[\frac{1}{r}\frac{\partial}{\partial r}\left(r\frac{\partial}{\partial r}(r\Omega)\right) - \frac{\Omega}{r}\right], \tag{2.19}$$

$$\frac{\partial P_0'}{\partial z} = -\rho_0'. \tag{2.20}$$

If we assume, by symmetry, that $\partial_\theta P_0' = 0$, then we can solve (2.19) for $\Omega(r)$:

$$\frac{1}{r}\frac{\partial}{\partial r}\left(r\frac{\partial}{\partial r}(r\Omega)\right) - \frac{\Omega}{r} = 0,$$

$$\implies \frac{\partial}{\partial r}\left(r\Omega + r^2\frac{\partial\Omega}{\partial r}\right) - \Omega = 0,$$

$$\implies \frac{\partial^2\Omega}{\partial r^2} + \frac{3}{r}\frac{\partial\Omega}{\partial r} = 0. \tag{2.21}$$

We can solve (2.21) with the following form of $\Omega(r)$, with A and B as constants of integration:

$$\Omega(r) = A + \frac{B}{r^2}.$$

We can find A and B by applying the boundary conditions:

$$\Omega_1 = A + \frac{B}{r_1^2}, \quad \Omega_2 = A + \frac{B}{r_2^2},$$

$$\implies A = \frac{r_1^2\Omega_1 - r_2^2\Omega_2}{r_1^2 - r_2^2}, \quad B = -r_1^2 r_2^2\frac{\Omega_1 - \Omega_2}{r_1^2 - r_2^2}.$$

Applying the ratios η and μ:

$$A = \Omega_1\frac{\mu - \eta^2}{1 - \eta^2}, \quad B = r_1^2\Omega_1\frac{1 - \mu}{1 - \eta^2}.$$

Finally, applying the known quantities r_1 and Ω_1:

$$A = \frac{\mu - \eta^2}{1 - \eta^2}, \quad B = \frac{\eta^2\left(1 - \mu\right)}{\left(1 + \eta\right)\left(1 - \eta\right)^3}.$$

An example of $\Omega(r)$ is shown in figure 2.1. Notice how, due to our choice of length-scale and time-scale, the curve ranges from $\frac{\eta}{1-\eta} \le r \le \frac{1}{1-\eta}$ and between $\mu \le \Omega \le 1$. Notice also that, because $\mu < 1$, the curve decreases with radius across the radial range.

Conclusion

We have a basic state flow of the form $\boldsymbol{u_0} = [0, r\Omega(r), 0]$, with:

$$\Omega(r) = A + \frac{B}{r^2}, \tag{2.22}$$

$$A = \frac{\mu - \eta^2}{1 - \eta^2}, \quad B = \frac{\eta^2\left(1 - \mu\right)}{\left(1 + \eta\right)\left(1 - \eta\right)^3}.$$

and the following set of conditions on P_0' and ρ_0':

$$\frac{\partial P_0'}{\partial r} = r\Omega^2, \quad \frac{\partial P_0'}{\partial \theta} = 0, \quad \frac{\partial P_0'}{\partial z} = -\rho_0' g. \tag{2.23}$$

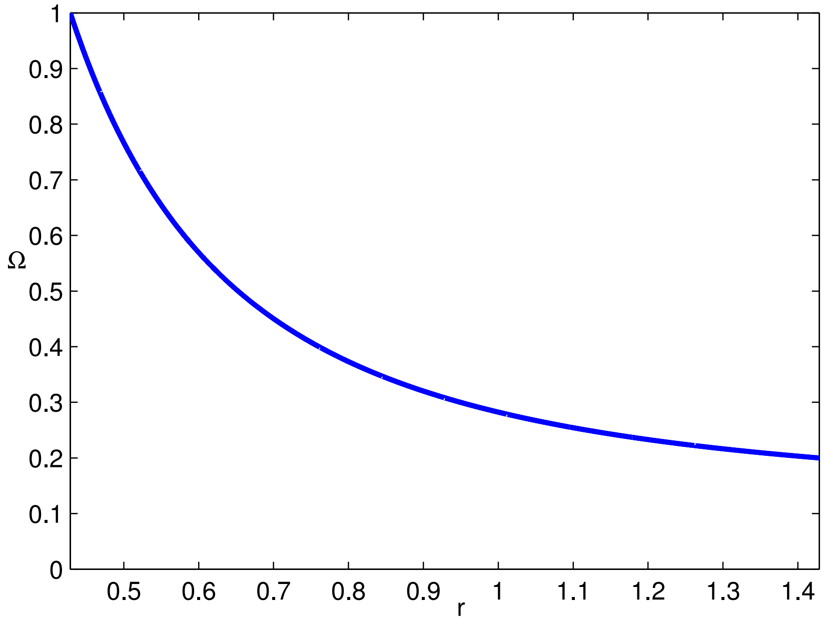

Figure 2.1: Example curve for the basic state flow $\Omega(r)$. Here we have used $\eta = 0.3$ and $\mu = 0.2$.

2.4 The SRI equations

2.4.1 Perturbation analysis

We introduce perturbations of the form $a = a_0 + a_1$, with $|a_1| \ll |a_0|$ such that the basic state variables a_0 may be considered to satisfy the system equations (2.4), (2.12) and (2.13). Perturbations are applied to the three dimensions of the flow velocity, and the Boussinesq pressure and density: $[\boldsymbol{u}, P', \rho']$. For the density perturbation we also include a factor of $1/g$, such that:

$$\rho' = \rho'_0 + \frac{\rho_1}{g}. \tag{2.24}$$

Substituting these perturbations into equations (2.4), (2.12) and (2.13) yields:

(We have used the notation $\boldsymbol{u} = [u, v, w]$.)

$$\frac{\partial \boldsymbol{u_1}}{\partial t} + \boldsymbol{u_0}.\boldsymbol{\nabla}\boldsymbol{u_1} + \boldsymbol{u_1}.\boldsymbol{\nabla}\boldsymbol{u_0} = -\boldsymbol{\nabla}P_1 - \rho_1\boldsymbol{e_z} + \frac{\eta}{(1-\eta)}\frac{1}{Re}\boldsymbol{\nabla}^2\boldsymbol{u_1} \tag{2.25}$$

$$\frac{1}{g}\frac{\partial \rho_1}{\partial t} + \frac{1}{g}\boldsymbol{u_0}.\boldsymbol{\nabla}\rho_1 + \boldsymbol{u_1}.\boldsymbol{\nabla}\rho'_0 = 0, \tag{2.26}$$

$$\boldsymbol{\nabla . u_1} = 0. \tag{2.27}$$

Note that we have retained terms only to first order in perturbations and that basic state terms have been cancelled.

We can now drop the subscripts on perturbation terms, expand the system, and apply our knowledge of the basic state from equation (2.22):

$$\frac{\partial u}{\partial t} + \Omega \frac{\partial u}{\partial \theta} - 2\Omega v = -\frac{\partial P}{\partial r} + \frac{\eta}{(1-\eta)} \frac{1}{Re} \left(\nabla^2 u - \frac{u}{r^2} - \frac{2}{r^2} \frac{\partial v}{\partial \theta} \right), \tag{2.28}$$

$$\frac{\partial v}{\partial t} + \Omega \frac{\partial v}{\partial \theta} + \zeta u = -\frac{1}{r} \frac{\partial P}{\partial \theta} + \frac{\eta}{(1-\eta)} \frac{1}{Re} \left(\nabla^2 v - \frac{v}{r^2} + \frac{2}{r^2} \frac{\partial u}{\partial \theta} \right), \tag{2.29}$$

$$\frac{\partial w}{\partial t} + \Omega \frac{\partial w}{\partial \theta} = -\frac{\partial P}{\partial z} - \rho + \frac{\eta}{(1-\eta)} \frac{1}{Re} \nabla^2 w, \tag{2.30}$$

$$\frac{\partial \rho}{\partial t} + \Omega \frac{\partial \rho}{\partial \theta} + w \frac{\partial \rho_0'}{\partial z} g = 0, \tag{2.31}$$

$$\frac{\partial u}{\partial r} + \frac{u}{r} + \frac{1}{r} \frac{\partial v}{\partial \theta} + \frac{\partial w}{\partial z} = 0. \tag{2.32}$$

Here we have defined the vorticity:

$$\zeta = r \frac{\partial \Omega}{\partial r} + 2\Omega = \frac{1}{r} \frac{\partial}{\partial r} \left(r^2 \Omega \right). \tag{2.33}$$

The vorticity ζ can be considered as a function of the gradient of the basic state angular momentum, $r^2\Omega$. It relates to the Rayleigh Criterion (Section 2.4.4), in that it is negative when the criterion for instability is satisfied, and positive when it isn't. Note that in the context of Taylor-Couette basic state flow (2.22), $\zeta = 2A$ and is constant.

We now assume that the perturbations are periodic in the azimuthal and vertical directions, with wavenumbers of m and k respectively. We also assume that the perturbations have a complex exponential growth rate σ. This gives the perturbations a harmonic ansatz of the form:

$$a(r, \theta, z, t) = \tilde{a}(r) \exp(\sigma t + i[m\theta + kz]). \tag{2.34}$$

Substituting this ansatz into the system allows us to retain only the radial gradient terms. We define the quantity $\Phi = i\sigma - m\Omega$ as the perturbation's Lagrangian frequency. We also substitute in the buoyancy frequency $N^2 = -g\partial\rho_0'/\partial z$ from section 2.2.6.

$$-i\Phi u - 2\Omega v = -\frac{dP}{dr} + \frac{\eta}{(1-\eta)} \frac{1}{Re} \left[\frac{d^2 u}{dr^2} + \frac{1}{r} \frac{du}{dr} - \left(\frac{m^2+1}{r^2} + k^2 \right) u - \frac{2imv}{r^2} \right], \tag{2.35}$$

$$-i\Phi v+\zeta u=-\frac{imP}{r}+\frac{\eta}{(1-\eta)}\frac{1}{Re}\left[\frac{d^2v}{dr^2}+\frac{1}{r}\frac{dv}{dr}-\left(\frac{m^2+1}{r^2}+k^2\right)v+\frac{2imu}{r^2}\right],\tag{2.36}$$

$$-i\Phi w=-ikP-\rho+\frac{\eta}{(1-\eta)}\frac{1}{Re}\left[\frac{d^2w}{dr^2}+\frac{1}{r}\frac{dw}{dr}-\left(\frac{m^2}{r^2}+k^2\right)w\right],\tag{2.37}$$

$$-i\Phi\rho-N^2w=0,\tag{2.38}$$

$$\frac{du}{dr}+\frac{u}{r}+\frac{imv}{r}+ikw=0.\tag{2.39}$$

These are now the full viscous equations for the stratified rotational instability.

The Complex Growth Rate σ

The term σ represents the time-dependence of the perturbation mode.

The real part of σ is the mode's physical growth rate. If this is negative, then the perturbation amplitudes are decreasing with time, and the system is stable with respect to that perturbation mode. Correspondingly, if the real part of σ is positive, then the amplitude is increasing with time, and the system is unstable. The system as a whole is only considered to be stable if all possible perturbation modes are stable.

The imaginary part of σ is the negative of the modal frequency, such that $f=-Im(\sigma)$. This convention is used to ensure that a mode travelling in the positive vertical or azimuthal directions has a positive frequency.

Therefore we can decompose σ as follows:

$$\sigma=\sigma_r+i\sigma_i=\sigma_r-if$$

where σ_r is the physical growth rate and f is the modal frequency.

The Lagrangian Frequency, Φ

$$\Phi=i\sigma-m\Omega.\tag{2.40}$$

The Lagrangian frequency is the complex frequency of the perturbation as seen by a fluid element moving with the flow. Note that this changes based on the element's radial location, since the basic state flow has a radial dependence.

From substituting in the previous decomposition of σ, we see that:

$$\Phi = i\sigma_r + f - m\Omega.$$

2.4.2 Perturbation Boundary Conditions

The boundary conditions of Taylor-Couette flow are satisfied by the basic state flow velocities. Therefore, the boundary conditions on the perturbations require that the perturbed velocities are equal to the basic state flow at the boundaries - i.e., that the velocity perturbations go to zero at r_1 and r_2:

$$\begin{aligned} r = r_1 = \frac{\eta}{1-\eta} &\implies \quad u = v = w = 0, \\ r = r_2 = \frac{1}{1-\eta} &\implies \quad u = v = w = 0. \end{aligned} \tag{2.41}$$

This gives us a total of six boundary conditions, which is equal to the total differential order of the perturbed system.

2.4.3 Common system limits

Inviscid flow

In the inviscid limit, viscosity is treated as negligible such that $\nu \to 0$. In our choice of units, this is equivalent to $(1/Re) \to 0$. This approximation does not significantly change the derivation of the perturbation equations, and without the viscous dissipation terms we attain the following system of inviscid equations:

$$-i\Phi u - 2\Omega v = -\frac{dP}{dr}, \tag{2.42}$$

$$-i\Phi v + \zeta u = -i\frac{m}{r}P, \tag{2.43}$$

$$-i\Phi w = -ikP - \rho, \tag{2.44}$$

$$-i\Phi\rho - N^2 w = 0, \tag{2.45}$$

$$\frac{du}{dr} + \frac{u}{r} + i\frac{m}{r}v + ikw = 0. \tag{2.46}$$

The inviscid system of equations can be expressed as a single second order differential equation (2.48). The system therefore requires only two boundary conditions, rather than the six non-slip boundary conditions of (2.17). To that end we consider no-normal-flow boundary conditions such that the flow cannot pass through the walls; i.e. the radial flow velocity must be zero at r_1 and r_2. This condition is carried through onto the radial perturbation velocity:

$$r = [r_1, r_2] \implies \quad u = 0. \tag{2.47}$$

Yavneh et al. [2001] were the first to show that the inviscid system can be combined into a single equation for the radial perturbation. This combined inviscid equation has various equivalent forms; we present here the form used by Park and Billant [2013]:

$$\frac{d^2u}{dr^2} + \left(\frac{1}{r} - \frac{Q'}{Q}\right)\frac{du}{dr} + \left[-\frac{k^2}{N^2 - \Phi^2}\Delta - \frac{m^2}{r^2} + \frac{mrQ}{\Phi}\left(\frac{\zeta}{r^2Q}\right)' + Q\left(\frac{1}{rQ}\right)'\right]u = 0,$$

$$Q(r) = \frac{m^2}{r^2} - \frac{k^2\Phi^2}{N^2 - \Phi^2}, \quad \Delta(r) = 2\zeta\Omega - \Phi^2. \tag{2.48}$$

The derivation of this equation is given in Appendix A.

Note that $\Phi = 0$ and $\Phi = \pm N$ are all singular points within this equation. Multiplying through by Φ we can deduce that $\Phi = 0$ removes the $d_r^2 u$ and $d_r u$ terms, yielding a linear equation for u. Furthermore, inspection of (2.45) also tells us that $\Phi = 0 \implies w = 0$. For the case $\Phi = \pm N$, examination of (2.44) and (2.45) tells us that this implies $P = 0$. This latter case, for which $\Phi^2(r_c) = N^2$ for some radial layer with $r = r_c$ is relevant to both the low-stratification inviscid domain (see section 4.3.1) and the viscous radiative instability (see section 6.3).

The distinct radial layers where $\Phi(r) = 0$, $\Phi(r) = \pm N$, and also where $\Delta(r) = 0$, are all relevant to the instability conditions derived by Park and Billant [2013]; see chapter 4 and Appendix D.

Unstratified flow

In the absence of stratification, we have $N = 0$ and we lose the mass conservation equation, leaving the following system of equations:

$$-i\Phi u - 2\Omega v = -\frac{\partial P}{\partial r} + \frac{\eta}{(1-\eta)}\frac{1}{Re}\left[\frac{d^2u}{dr^2} + \frac{1}{r}\frac{du}{dr} - \left(\frac{m^2+1}{r^2} + k^2\right)u - \frac{2im}{r^2}v\right], \tag{2.49}$$

$$-i\Phi v + \zeta u = -\frac{im}{r}P + \frac{\eta}{(1-\eta)}\frac{1}{Re}\left[\frac{d^2v}{dr^2} + \frac{1}{r}\frac{dv}{dr} - \left(\frac{m^2+1}{r^2} + k^2\right)v + \frac{2im}{r^2}u\right], \tag{2.50}$$

$$-i\Phi w = -ikP + \frac{\eta}{(1-\eta)}\frac{1}{Re}\left[\frac{d^2w}{dr^2} + \frac{1}{r}\frac{dw}{dr} - \left(\frac{m^2}{r^2} + k^2\right)w\right], \tag{2.51}$$

$$\frac{du}{dr} + \frac{u}{r} + \frac{im}{r}v + ikw = 0. \tag{2.52}$$

The viscous boundary conditions (2.41) are retained.

It has been shown (see below) that the inviscid unstratified system is only unstable up to the Rayleigh line $\mu = \eta^2$. It is therefore assumed that the viscous unstratified system has the same stability limit for sufficiently high Reynolds numbers.

Unstratified Inviscid flow

The limits of the lack of stratification and viscosity can be taken simultaneously, yielding the following system of equations:

$$-i\Phi u - 2\Omega v = -\frac{\partial P}{\partial r}, \tag{2.53}$$

$$-i\Phi v + \zeta u = -\frac{im}{r}P, \tag{2.54}$$

$$-i\Phi w = -ikP, \tag{2.55}$$

$$\frac{du}{dr} + \frac{u}{r} + \frac{im}{r}v + ikw = 0. \tag{2.56}$$

Boundary conditions are unchanged compared to the stratified inviscid system (2.47). This system is the classical inviscid Taylor-Couette system. It has been shown in Rayleigh [1917] that the system is only unstable up to the Rayleigh line $\mu = \eta^2$, and that $m = 0$ modes are always more unstable than $m \neq 0$ modes.

2.4.4 Rayleigh Criterion for Centrifugal Instability

In the absence of stratification, Rayleigh's criterion [Rayleigh, 1917] applies for inviscid fluid flows with angular velocity $\Omega(r)$. It is a statement of how the stability of the flow depends on the form of $\Omega(r)$.

Let $H(r)$ be defined as the gradient of the square of the angular momentum:

$$H(r) = \frac{d}{dr}\left(r^4\Omega^2\right). \tag{2.57}$$

If $H(r) > 0$ everywhere in the flow, then the flow is stable against axisymmetric instabilities. If $H(r) < 0$ anywhere in the flow, then the flow is unstable.

A full derivation of Rayleigh's criterion is presented in Chandrasekhar [1961]; it is extended to axisymmetric stratified flows by Ooyama [1966].

In the co-rotating unstratified domain of rotating fluid flows, it is generally assumed that axisymmetric perturbations are always more unstable than non-axisymmetric perturbations, due to the results of Andereck et al. [1986]. Therefore, one might expect the Rayleigh Criterion to also apply to non-axisymmetric perturbations, however this has not been proven to be the case. Indeed, in the presence of stratification, the SRI is a non-axisymmetric instability for which the Rayleigh Criterion does not apply (e.g. figure 3.3).

Taylor-Couette flow

In the context of the basic state Taylor-Couette flow used throughout this work, we can calculate $H(r)$ directly using the definition of Ω in (2.22):

$$H(r) = \frac{d}{dr}\left[r^4\left(A + \frac{B}{r^2}\right)^2\right] = \frac{d}{dr}\left[A^2r^4 + 2ABr^2 + B^2\right], \tag{2.58}$$

$$\implies H(r) = 4A^2r^3 + 4ABr = 4Ar\left(Ar^2 + B\right) = 4Ar^3\Omega(r). \tag{2.59}$$

If $\Omega(r)$ changes sign within the flow then $H(r)$ will be negative somewhere, since A is a constant and $r > 0$. This indicates that counter-rotating Taylor-Couette flows are always unstable - i.e. that $\mu < 0$ is sufficient for inviscid instability.

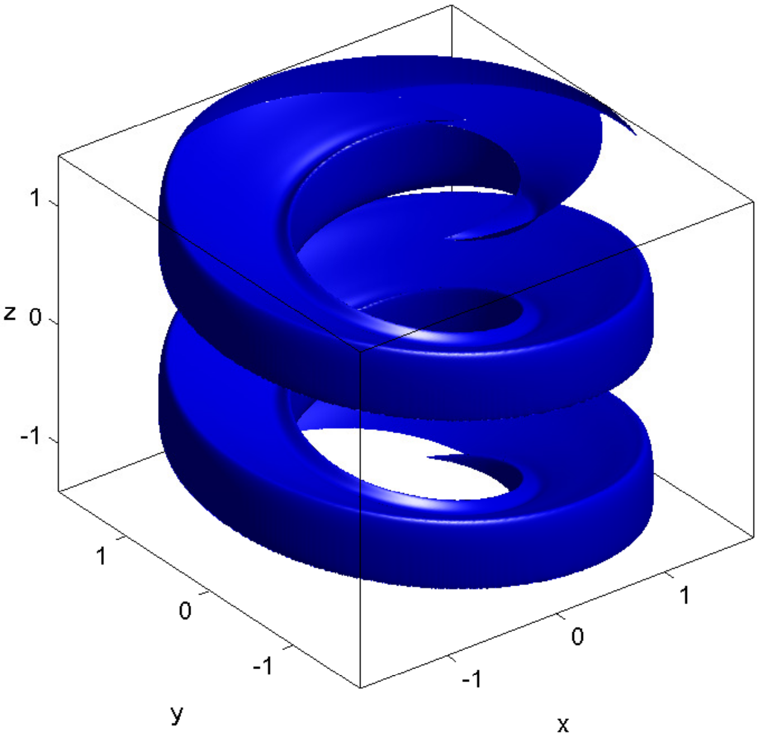

Figure 2.2: A 3D contour plot of the density perturbation for an SRI mode, demonstrating the spiral form of the instability. Here $\eta = 0.45, \mu = 0.45, m = 1, k = 4.44, Re = 304.1, N = 1.0$ and $\sigma = -0.595i$.

However, if $\mu > 0$ then $\Omega(r)$ has the same sign everywhere within the flow. In this case, $H(r)$ can only be negative if A has a different sign to $\Omega(r)$, which requires that $\mu < \eta^2$.

Since $\eta^2 > 0$, we can therefore conclude that $\mu < \eta^2$ is the necessary and sufficient condition for instability in inviscid unstratified Taylor-Couette flow.

It is important to note that, since a high Reynolds number corresponds to low viscosity, if the inviscid flow is unstable then we can generally expect the viscous flow to be unstable for a sufficiently high Reynolds number.

2.4.5 The Wavenumbers of the SRI

Figure 2.2 shows an example of the helical structure of the SRI by picturing a 3D contour of the density perturbation. Note that all instabilities which fit the ansatz (2.34) with non-zero m and k, would have a similar helical form. In the case of $[m, k] > 0$ the contour takes the form of a left-handed helix; the height of the contour increases as one moves clockwise around it.

Furthermore, Riedinger et al. [2011] identified the following symmetries in the system of perturbation equations (2.35)-(2.39):

$$[m, k, \sigma, u, v, w, \rho, P] \to [-m, k, \bar{\sigma}, \bar{u}, \bar{v}, -\bar{w}, -\bar{\rho}, \bar{P}],$$

$$[m, k, \sigma, u, v, w, \rho, P] \to [m, -k, \sigma, u, v, -w, -\rho, P].$$

$$[m, k, \sigma, u, v, w, \rho, P] \to [-m, -k, \bar{\sigma}, \bar{u}, \bar{v}, \bar{w}, \bar{\rho}, \bar{P}],$$

Here $\bar{a}$ denotes the complex conjugate of a. The first two reflections produce a right-handed helix, whereas the third double reflection retains the original left-handed helix.

These symmetries mean that, for any unstable mode with wavenumbers $[m, k]$ and Reynolds number Re at fixed $[\eta, \mu, N]$, there will be an equally unstable mode with the same Reynolds number for each variation of $[\pm m, \pm k]$. Each mode will either have the same perturbation functions $[u, v, w, \rho, P]$ or the complex conjugates of these functions. Vice versa, if for fixed $[\eta, \mu, N]$ then a specific mode with some $[m, k, Re]$ is found to be stable, it can be concluded that each variation of $[\pm m, \pm k]$ will also be stable for the same Reynolds number.

All four combinations of $[\pm m, \pm k]$ result in eigenfunctions of equal growth rates and with frequencies of equal absolute value. These symmetries therefore allow us to restrict our analysis to just the positive domain of the wavenumbers $[m, k]$.

2.4.6 Critical Reynolds number

Consider an experimental system with fixed $[\eta, \mu, N]$, and a steadily increasing Reynolds number Re. The critical Reynolds number Re_c is the Reynolds number at which this system first becomes unstable. For all possible wavenumbers $[m, k]$ and frequencies f, the critical Reynolds number is therefore the smallest unstable Reynolds number available to the system.

The critical Reynolds number will have an associated critical perturbation mode of instability, with critical wavenumbers $[m_c, k_c]$ and a critical frequency f_c. The growth rate of this mode must be $\sigma_r = 0$. This is because if the Reynolds number is slightly reduced then the system must be stable, with viscous damping providing a negative growth rate. On the other hand, if the Reynolds number is slightly increased the system will gain a positive growth rate.

Under some circumstances, we may wish to know the critical Reynolds number for some fixed value of the wavenumbers - i.e. the Reynolds number at which a specific mode becomes unstable. We label this as Re_{mk}. Similarly, if we want to know the critical Reynolds number optimising over k but with a fixed value of m, say for example $m = 0$, then we can label this as $Re_{m=0}$.

It is worth pointing out that the system we have described, of holding N fixed with increasing Re, is actually somewhat unrealistic for our choice of dimensional units. In practise, the dimensional terms $\hat{N}$ and $\hat{\nu}$ can be held reasonably constant in laboratory experiments, while $\hat{\Omega}_{\text{in}}$ can be steadily increased in order to adjust the Reynolds number Re. However, since $N = \hat{N}/\hat{\Omega}_{\text{in}}$, this would not correspond to a fixed value of N.

Our description would therefore correspond to either adjusting $\hat{N}$ alongside $\hat{\Omega}_{\text{in}}$, in order to keep their ratio constant, or adjusting $\hat{\nu}$ whilst holding $\hat{N}$ and $\hat{\Omega}_{\text{in}}$ constant. However, neither of these is particularly feasible in practise.

2.5 Eigenfunction forms

It is also useful to express the equations in terms of linear differential operators, $[L_a, R_a]$ acting on eigenfunctions $[u, v, w, \rho, P]$, with a single eigenvalue $[\sigma]$:

$$L_a(u, v, w, \rho, P) = \sigma R_a(u, v, w, \rho, P), \quad a = [1, 2, 3, 4, 5].$$

This is done for the sake of computational analysis of the system - see chapter 3.

In each case, this can be achieved by resubstituting $-i\Phi = (\sigma + im\Omega)$ into the system equations and collecting terms with a factor of σ on the right hand side of each equation.

Standard SRI

$$
\begin{gathered}
\nu\frac{d^2u}{dr^2}+\frac{\nu}{r}\frac{du}{dr}+\left(-\frac{\nu\left(m^2+1\right)}{r^2}-\nu k^2-im\Omega\right)u+\left(2\Omega-\nu\frac{2im}{r^2}\right)v-\frac{dP}{dr}=\sigma u,\\
\left(\nu\frac{2im}{r^2}-\zeta\right)u+\nu\frac{d^2v}{dr^2}+\nu\frac{1}{r}\frac{dv}{dr}+\left(-\frac{\nu\left(m^2+1\right)}{r^2}-\nu k^2-im\Omega\right)v-\frac{im}{r}P=\sigma v,\\
\nu\frac{d^2w}{dr^2}+\nu\frac{1}{r}\frac{dw}{dr}+\left(-\frac{\nu m^2}{r^2}-\nu k^2-im\Omega\right)w-\rho-ikP=\sigma w,\\
N^2w-im\Omega\rho=\sigma\rho,\\
\frac{du}{dr}+\frac{1}{r}u+\frac{im}{r}v+ikw=0,\\
r=\left[r_{\text{in}},r_{\text{out}}\right]\implies\qquad u=v=w=0.
\end{gathered}
$$

(Here $\nu=\eta/\left[Re\left(1-\eta\right)\right]$ is the kinematic viscosity $\hat{\nu}$ expressed in dimensionless units.)

Inviscid SRI

$$
\begin{gathered}
-im\Omega u+2\Omega v-\frac{dP}{dr}=\sigma u,\\
-\zeta u-im\Omega v-\frac{im}{r}P=\sigma v,\\
-im\Omega w-\rho-ikP=\sigma w,\\
N^2w-im\Omega\rho=\sigma\rho,\\
\frac{du}{dr}+\frac{1}{r}u+\frac{im}{r}v+ikw=0,\\
r=\left[r_{\text{in}},r_{\text{out}}\right]\implies\qquad u=0.
\end{gathered}
$$

Unstratified Taylor-Couette

$$
\begin{gathered}
\nu\frac{d^2u}{dr^2}+\frac{\nu}{r}\frac{du}{dr}+\left(-\frac{\nu\left(m^2+1\right)}{r^2}-\nu k^2-im\Omega\right)u+\left(2\Omega-\nu\frac{2im}{r^2}\right)v-\frac{dP}{dr}=\sigma u,\\
\left(\nu\frac{2im}{r^2}-\zeta\right)u+\nu\frac{d^2v}{dr^2}+\nu\frac{1}{r}\frac{dv}{dr}+\left(-\frac{\nu\left(m^2+1\right)}{r^2}-\nu k^2-im\Omega\right)v-\frac{im}{r}P=\sigma v,\\
\nu\frac{d^2w}{dr^2}+\nu\frac{1}{r}\frac{dw}{dr}+\left(-\frac{\nu m^2}{r^2}-\nu k^2-im\Omega\right)w-ikP=\sigma w,\\
\frac{du}{dr}+\frac{1}{r}u+\frac{im}{r}v+ikw=0,\\
r=\left[r_{\text{in}},r_{\text{out}}\right]\implies\qquad u=v=w=0.
\end{gathered}
$$

Inviscid Unstratified Taylor-Couette

$$
\begin{aligned}
-im\Omega u + 2\Omega v - \frac{dP}{dr} = \sigma u, \\
-\zeta u - im\Omega v - \frac{im}{r} P = \sigma v, \\
-im\Omega w - ikP = \sigma w, \\
\frac{du}{dr} + \frac{1}{r}u + \frac{im}{r}v + ikw = 0, \\
r = [r_{\text{in}}, r_{\text{out}}] \implies \quad u = 0.
\end{aligned}
$$

2.6 Alternative Length-scales and Time-scales

There are several alternative length-scales and time-scales that we could have chosen, instead of the gap width, $\hat{\lambda} = \hat{r}_{\text{out}} - \hat{r}_{\text{in}}$, and the reciprocal of the inner rotation rate, $\tau = \hat{\Omega}_{\text{in}}^{-1}$.

2.6.1 Viscous Time-scale

In typical lab experiments, the viscosity is unchanging whereas the inner rotation rate is varied in order to control the Reynolds Number. This makes the viscous time-scale $\hat{\lambda}^2/\hat{\nu}$ a useful choice of units for direct comparison to physical experiments.

However using the viscous time-scale is incompatible with the inviscid limit, where viscosity is discarded. This means that, if we were using the viscous time-scale, we would need to change units whenever we shifted to the inviscid system, and results from the two systems would be non-trivial to compare.

2.6.2 Stationary inner cylinder

The reciprocal of the inner rotation rate cannot be used as a time-scale when $\hat{\Omega}_{\text{in}} = 0$. This possibility is particularly relevant for the case where $\hat{\Omega}_{\text{in}} < \hat{\Omega}_{\text{out}}$, i.e. the outer cylinder is rotating faster than the inner cylinder. (The majority of Park and Billant [2013] focuses on this case.) In this circumstance, it makes sense to choose the reciprocal of the outer rotation rate as the time-scale of the system. It also becomes more useful to use the ratio $\hat{\Omega}_{\text{out}}/\hat{\Omega}_{\text{in}}$, rather than $\mu = \hat{\Omega}_{\text{in}}/\hat{\Omega}_{\text{out}}$, since $\mu \to \infty$ as $\hat{\Omega}_{\text{in}} \to 0$.

However throughout this work we will be primarily interested in the range $0 \leq \mu \leq 1$, rather than cases where $\mu > 1$.

2.6.3 Wide gap limit

Choosing the gap width as the length-scale is less useful for taking wide-gap limit $\eta \to 0$. Instead either $\hat{r}_{\text{in}}$ or $\hat{r}_{\text{out}}$ could be used, each of which would lead to similar set of dimensionless equations, albeit modified by factors of η. Choosing $\hat{r}_{\text{in}}$ as a length-scale for the wide-gap limit corresponds to a system where the outer cylinder is taken to the limit $r = \infty$, whereas choosing $\hat{r}_{\text{out}}$ corresponds to a fixed outer cylinder with a vanishingly thin inner cylinder.

However, the following work within this thesis will primarily focus on both moderate gaps and the narrow-gap limit $\eta \to 1$, for which a length-scale of $\hat{\lambda} = 1$ is appropriate.

Chapter 3

Generalised Eigenfunction Solver

Linear perturbation theory typically produces an eigenfunction problem with the complex growth rate as an eigenvalue. This chapter will explain how eigenfunction problems with a single eigenvalue can be written in matrix form, to then be solved using computational methods.

For further reading on the topic of solving linear differential equations by usage of spectral methods, see Gottlieb and Orszag [1977], Boyd [2001] and Canuto et al. [2006].

3.1 Generalised Eigenfunction problem

Consider a system of A equations of the form:

$$\mathcal{L}_a\left(f_1, f_2, ..., f_A\right) = \sigma\mathcal{R}_a(f_1, f_2, ..., f_A), \quad y_1 < y < y_2, \quad a = [1, 2, ..., A], \tag{3.1}$$

where $\mathcal{L}_a$ and $\mathcal{R}_a$ are linear differential operators, σ is a constant eigenvalue and the eigenfunctions f_α are all functions of y. (The term α ranges from $1 : A$.)

The operators $\mathcal{L}_a$ and $\mathcal{R}_a$ are given, whereas the problem is to be solved for σ and f_α.

If the total differential order of the system is B, the system has B boundary conditions of the form:

$$\mathcal{B}_b\left(f_1, f_2, ..., f_A\right) = 0, \quad y = y_i, \quad b = [1, 2, ..., B],$$

where the $\mathcal{B}_b$ are linear differential operators, and i can be equal to 1 or 2.

Note that the linearised Taylor-Couette equations in chapter 2 are an example of such a system.

3.1.1 Matrix equation

The system in section 3.1 can be expressed as a matrix equation of the form:

$$\boldsymbol{\mathcal{L}} \boldsymbol{v} = \sigma \boldsymbol{\mathcal{R}} \boldsymbol{v} \tag{3.2}$$

where $\boldsymbol{\mathcal{L}}$ and $\boldsymbol{\mathcal{R}}$ are matrices, $\boldsymbol{v}$ is an eigenvector representing the functions f_α, and σ is the same constant eigenvalue as before.

This is a generalised matrix eigenfunction problem to be solved for $\boldsymbol{v}$ and σ when supplied with the matrices $\boldsymbol{\mathcal{L}}$ and $\boldsymbol{\mathcal{R}}$.

In order to achieve the matrix formulation of the problem, we make use of spectral methods to decompose each eigenfunction into a series of coefficients. By necessity these series are truncated, since perfect accuracy can only be achieved by taking the series to infinity. However, spectral methods exhibit exponential convergence, and with sufficient terms then the truncated series is accurate to within a small approximation. We introduce the term T as an integer measure of the number of coefficients taken before truncating each series.

For the analysis of Taylor-Couette instabilities, we chose Chebyshev polynomials for the spectral decomposition. Chebyshev polynomials exhibit additional variation near the boundaries of the domain. We expect significant boundary phenomena in the form of the Taylor-Couette instabilities, making Chebyshev polynomials well suited to the system.

Spectral methods making use of Chebyshev polynomials to solve differential equations are explained further in appendix B.

3.1.2 Collocation points

To accommodate the natural range for Chebyshev functions, the system must be rescaled from operating over $[y_1 < y < y_2]$ to operating over $[-1 < x < +1]$. This can be achieved by the formula:

$$x = \frac{2y - (y_1 + y_2)}{y_2 - y_1}.$$

The collocation points are a set of values $x = x_c$ for $0 \leq c \leq T$ for which the Chebyshev functions can be easily evaluated. The matrix equation (3.2) does not evaluate the original system at every value for x, except for in the limit $T \to \infty$. Instead, the system is evaluated at each collocation point. It is assumed that, for values of x away from the collocation points, any solution to the matrix equation will only have a small divergence away from the ideal solution. This assumption is based on the exponential accuracy of spectral methods.

3.1.3 The Eigenvector

Each of the functions f_α is expressed as a truncated Chebyshev series. Typically each series is truncated at T terms, but in certain circumstances (see section 3.2.5) it may be necessary to slightly increase or reduce the size of the Chebyshev expansion for a specific eigenfunction. For example, f_3 might be evaluated to $T - 2$ terms, and f_4 taken to $T + 2$ terms.

The eigenvector of the matrix equation is then constructed by compiling each set of Chebyshev coefficients in turn. The first set of terms of the eigenvector consist of the coefficients for $f_1(x)$, the next set are the coefficients for $f_2(x)$, etc.

3.2 Formulating the Matrices

Consider the matrix equation in index notation:

$$\mathcal{L}_{ij} v_j = \sigma \mathcal{R}_{ij} v_j \tag{3.3}$$

Evaluating (3.3) at a specific value of i corresponds to approximately evaluating a specific equation from the original system at some collocation point x_c. Specific ranges of i correspond to specific equations.

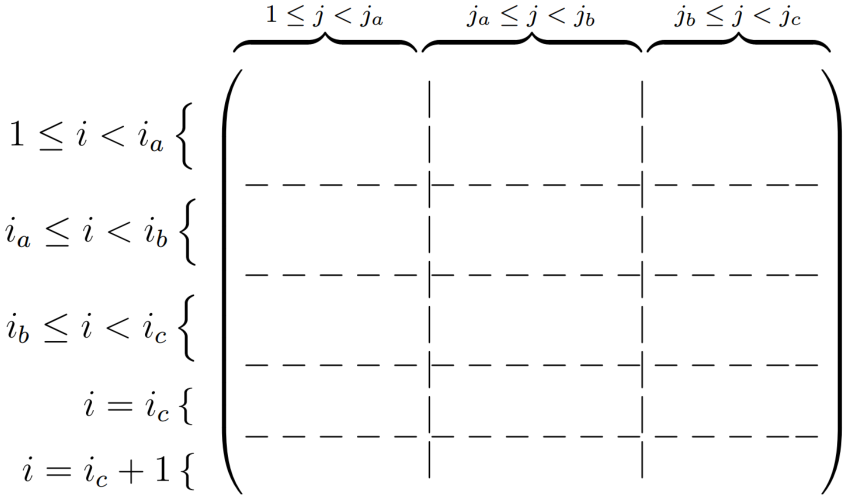

Figure 3.1: A representation of either $\mathcal{L}_{ij}$ or $\mathcal{R}_{ij}$, with $A = 3$ and $B = 2$, such that there are three equations, three eigenfunctions and two boundary conditions. Each range of columns corresponds to a specific eigenfunction, and each range of rows corresponds to a specific equation. The final two rows, $i = i_c$ and $i = i_c + 1$ correspond to the two boundary conditions.

Each column j of the two matrices corresponds to a single Chebyshev coefficient for a specific eigenfunction, such that the columns $\mathcal{L}_{i2}$ and $\mathcal{R}_{i2}$ will both correspond to the same coefficient. Specific ranges of j correspond to specific eigenfunctions. See figure 3.1 for a diagrammatical representation.

3.2.1 Function representation

Each of the functions f_α can be represented in one of three ways:

1. $f_\alpha(x)$ - Direct representation. This is the function f_α operating on some value of x.
2. $f_{\alpha,k}$ - Chebyshev Coefficients. This is the truncated series of Chebyshev coefficients for the function f_α. Here k labels a specific coefficient and ranges between $1 : K$, where K is the truncation point of the series. (Typically $K = T$.)
3. $f_\alpha(x_c)$ - Collocation point function values. This is the value of the function f_α at each collocation point. Here c labels a specific collocation point and ranges between $1 : C$, where C is the total number of points. (Typically $C = T$ also.)

$f_{\alpha,k}$ and $f_\alpha(x_c)$ are typically represented as vertical vectors, e.g.:

$$\begin{pmatrix} \\ f_{\alpha,k} \\ \\ \end{pmatrix}_K \text{ and } \begin{pmatrix} \\ f_\alpha(x_c) \\ \\ \end{pmatrix}_C$$

3.2.2 Collocation Matrix

$$\begin{pmatrix} \\ f_\alpha(x_c) \\ \\ \end{pmatrix}_C = \begin{pmatrix} \\ \quad Co \quad \\ \\ \end{pmatrix}_{[C,K]} \begin{pmatrix} \\ f_{\alpha,k} \\ \\ \end{pmatrix}_K \tag{3.4}$$

In equation (3.4), the matrix Co is the collocation matrix. It acts on a Chebyshev coefficient series $f_{\alpha,k}$ and returns $f_\alpha(x_c)$ in vector form; the values of that function on the collocation points.

The number of columns of the matrix corresponds to the number of collocation points, C, whereas the number of rows corresponds to the number of terms in the Chebyshev expansion of the function, K. Note that the matrix Co is completely defined by its number of rows and columns - it does not depend upon the function that it is being applied to.

The derivation of the terms of the collocation matrix is presented in appendix B.

3.2.3 Differentiation Matrix

$$\begin{pmatrix} \\ d_x f_{\alpha,k} \\ \\ \end{pmatrix}_K = \begin{pmatrix} \\ \quad D \quad \\ \\ \end{pmatrix}_{[K,K]} \begin{pmatrix} \\ f_{\alpha,k} \\ \\ \end{pmatrix}_K \tag{3.5}$$

In equation (3.5), the matrix D is the differentiation matrix. It acts on a Chebyshev coefficient series $f_{\alpha,k}$ and returns $d_x f_{\alpha,k}$ in vector form; the gradient of that function in Chebyshev coefficient form.

D is a square matrix; the number of rows and columns is equal to K, the number of terms in the Chebyshev expansion. Like Co, D is completely defined by the number of rows and columns, and does not depend upon the function f. As a square matrix, it can be applied multiple times, to derive the Chebyshev coefficients of higher gradients of the function.

The derivation of the terms of the differentiation matrix is presented in appendix B.

The differentiation matrix can be used in conjunction with the collocation matrix to produce the collocation values of the n^{th} gradient of a function, as follows:

$$\begin{pmatrix} d_x^n f_\alpha(x_c) \end{pmatrix}_C = \begin{pmatrix} \quad Co \quad \end{pmatrix}_{[C,K]} \begin{pmatrix} \quad D \quad \end{pmatrix}^n_{[K,K]} \begin{pmatrix} f_{\alpha,k} \end{pmatrix}_K \tag{3.6}$$

Representing a single function term

Take a single term within an equation, such as $Gd_x^n f_\alpha$. Here G is the coefficient of the function, and the function itself has been taken to the n^{th} gradient. (Note that $n \geq 0$, to include the possibility that the function has not been differentiated.)

If G is a constant, a matrix can easily be constructed that will take $f_{\alpha,k}$ and return $[Gd_x^n f_\alpha](x_c)$:

$$\begin{pmatrix} \quad M \quad \end{pmatrix}_{[C,K]} = G \begin{pmatrix} \quad Co \quad \end{pmatrix}_{[C,K]} \begin{pmatrix} \quad D \quad \end{pmatrix}^n_{[K,K]} \tag{3.7}$$

However, if $G = G(x)$, we must instead make use of the vector $G(x_c)$:

$$\begin{pmatrix} \quad M \quad \end{pmatrix}_{[C,K]} = \begin{pmatrix} G(x_c) \end{pmatrix}_C * \begin{pmatrix} \quad Co \quad \end{pmatrix}_{[C,K]} \begin{pmatrix} \quad D \quad \end{pmatrix}^n_{[K,K]} \tag{3.8}$$

Here $*$ represents a line-by-line multiplication between a vector $\boldsymbol{v}$ and a matrix $\boldsymbol{\mathcal{B}}$. In index notation then $\boldsymbol{\mathcal{A}} = \boldsymbol{v} * \boldsymbol{\mathcal{B}}$ can be represented, *without summation*, as:

$$A_{ij} = v_i B_{ij}$$

With M defined by equations (3.7) and (3.8), then we have:

$$\begin{pmatrix} \\ [Gd_x^n f_\alpha](x_c) \\ \\ \end{pmatrix}_C = \begin{pmatrix} & & \\ & M & \\ & & \end{pmatrix}_{[C,K]} \begin{pmatrix} \\ f_{\alpha,k} \\ \\ \end{pmatrix}_K \tag{3.9}$$

Furthermore, if an equation has a summation over two or more different terms involving f_α, we can create a combined matrix that will take $f_{\alpha,k}$ and act as a linear differential operator, returning the collocation values of the summed terms. We represent this combined matrix by $\boldsymbol{S}$.

For example, take $Gd_x^n f_\alpha + Hf_\alpha$:

$$\begin{aligned} \begin{pmatrix} & & \\ & S & \\ & & \end{pmatrix}_{[C,K]} &= \begin{pmatrix} \\ G(x_c) \\ \\ \end{pmatrix}_C * \begin{pmatrix} & & \\ & Co & \\ & & \end{pmatrix}_{[C,K]} \begin{pmatrix} & & \\ & D & \\ & & \end{pmatrix}^n_{[K,K]} \\ &+ \begin{pmatrix} \\ H(x_c) \\ \\ \end{pmatrix}_C * \begin{pmatrix} & & \\ & Co & \\ & & \end{pmatrix}_{[C,K]} \end{aligned} \tag{3.10}$$

In the case of boundary conditions, rather than evaluating a term at every collocation point, we instead need to evaluate it at the collocation point corresponding to either the inner or outer boundary, depending on the specific boundary condition. This can be achieved by taking either the first or last row of $\boldsymbol{S}$. This row can be treated as a horizontal vector J which acts on $f_{\alpha,k}$ to give the appropriate value at the appropriate boundary.

3.2.4 Matrix structure

For illustrative purposes, in this section we are going to assume that $A = 3$ and $B = 2$, i.e. that the original problem (3.1) had three equations and three eigenfunctions, with two boundary conditions.

Each side of the equations is treated separately, in order to derive each of $\boldsymbol{\mathcal{L}}$ and $\boldsymbol{\mathcal{R}}$. To generate $\boldsymbol{\mathcal{L}}$, take the left hand side of the equations, whereas to generate $\boldsymbol{\mathcal{R}}$ first divide through by σ and then take the right hand side of the equations.

$$\left(\begin{array}{c|c|c} S_1^1 & S_2^1 & S_3^1 \\ \hline S_1^2 & S_2^2 & S_3^2 \\ \hline S_1^3 & S_2^3 & S_3^3 \\ \hline J_1^1 & J_2^1 & J_3^1 \\ \hline J_1^2 & J_2^2 & J_3^2 \end{array}\right) \left(\begin{array}{c} f_{1,k} \\ \hline f_{2,k} \\ \hline f_{3,k} \end{array}\right)$$

Figure 3.2: The full set of half equations, assembled into a single matrix and a single eigenvector. Here the eigenvector is a list of each set of Chebyshev coefficients for each eigenfunction. This is the vector $\boldsymbol{v}$ in the matrix equation (3.2). The matrix, made up of the sub-matrices S_α^a and J_α^b, is either $\boldsymbol{\mathcal{L}}$ or $\boldsymbol{\mathcal{R}}$ depending on which side of the original equations (3.1) is being examined.

In either case, we are left with a set of three 'half-equations' and two 'half-boundary-conditions'. From here on, these are just referred to as the equations and boundary conditions respectively.

For each eigenfunction within each equation, group the appropriate terms into a linear differential operator acting on that eigenfunction. (If an eigenfunction does not appear in a specific half-equation, then the appropriate linear differential operator is just the zero operator.) As shown in the previous section, this linear differential operator can be represented by a matrix $\boldsymbol{S}$ acting on the Chebyshev coefficients of the eigenfunction, $f_{\alpha,k}$. The system, including boundary conditions, can then be represented as a single matrix operating on a single eigenvector, as shown in figure 3.2. Both $\boldsymbol{\mathcal{L}}$ and $\boldsymbol{\mathcal{R}}$ are constructed using this method.

Note that, for reasons explained in section 3.2.5, the various eigenfunctions may each have different numbers of Chebyshev coefficients in $\boldsymbol{v}$. If this is the case, the width of the appropriate sub-matrices S_α^a in $\boldsymbol{\mathcal{L}}$ or $\boldsymbol{\mathcal{R}}$ must correspond to the number of terms for the appropriate eigenfunction.

Zero rows

Depending on the form of (3.1), there may sometimes be occasions where a row in $\boldsymbol{\mathcal{L}}$ or $\boldsymbol{\mathcal{R}}$ is entirely zero. This is most often the case with boundary conditions, which in practical applications rarely involve the eigenvalue of the problem, and therefore the $\boldsymbol{\mathcal{R}}$ row corresponding to the boundary condition is entirely zero.

Such zero rows cause a problem for solving the generalised matrix eigenfunction problem, since most methods involve taking the inverses of $\boldsymbol{\mathcal{L}}$ and $\boldsymbol{\mathcal{R}}$. Therefore these zero rows must be removed, but without losing the equations that they represent.

To do this, we first rearrange the system such that all zero rows are within $\boldsymbol{\mathcal{R}}$ rather than $\boldsymbol{\mathcal{L}}$. Treating each row as an individual equation, this can always be done simply by switching which side is equal to zero. (Which side is which doesn't matter when one side is zero, since the eigenvalue can be divided out.)

Consider some quantity q as a pre-determined eigenvalue that can be ignored in the final solution, along with its associated eigenfunctions. q can be any quantity so long as it is recognisable; for our purposes, we used $q = -999$. This is because most of the work done with the program was focused on finding positive eigenvalue growth-rates corresponding to instability, and such a large negative eigenvalue would be automatically discarded.

With q chosen, we now replace the zero-row in $\boldsymbol{\mathcal{R}}$ by the finite row in $\boldsymbol{\mathcal{L}}$ multiplied by $1/q$. Labelling the left-hand-side row as the vector $\boldsymbol{\lambda}$, this results in the following equality within the overall system:

$$\boldsymbol{\lambda}.\boldsymbol{v} = \frac{\sigma}{q}\boldsymbol{\lambda}.\boldsymbol{v}. \tag{3.11}$$

Within the context of the complete system, (3.11) can be solved in only two ways. Either $\sigma = q$, in which case the resulting solution can be ignored, or $\boldsymbol{\lambda}.\boldsymbol{v} = 0$ as was implied by the equality of $\boldsymbol{\lambda}.\boldsymbol{v}$ with the original zero row. Hence the zero row has been replaced, but not discarded.

3.2.5 Chebyshev expansion adjustments

The matrices $\boldsymbol{\mathcal{L}}$ and $\boldsymbol{\mathcal{R}}$ must be square matrices for the generalised matrix eigenfunction problem to be solvable.

The height of the matrices Q is determined by $Q = AT + B$, where A is the number of equations, T is the number of collocation points and B is the number of boundary conditions. Conversely, the width of the matrices is determined by the total number of Chebyshev coefficients from each eigenfunction expansion; this quantity would typically be equal to AT if each eigenfunction was expanded to exactly T terms.

Therefore, the width of each matrix must be supplemented by the amount B. This is done by increasing the number of terms in some of the Chebyshev expansions. Typically, for an individual eigenfunction problem, each boundary condition is examined in turn and an extra term is added to the expansion of the eigenfunction most closely related to that particular boundary condition.

3.3 Computational evaluation

We now have two large matrices, $\boldsymbol{\mathcal{L}}$ and $\boldsymbol{\mathcal{R}}$, the core components of equation (3.2). For reference, (3.2) is repeated below:

$$\boldsymbol{\mathcal{L}}\boldsymbol{v} = \sigma\boldsymbol{\mathcal{R}}\boldsymbol{v}$$

With $\boldsymbol{\mathcal{L}}$ and $\boldsymbol{\mathcal{R}}$ supplied, this is a generalised matrix eigenvalue problem, which can be solved for $\boldsymbol{v}$ and σ.

Suppose that the original eigenfunction problem (3.1) has a solution, and that the eigenfunctions in this solution can be accurately described by sets of truncated Chebyshev series. (These Chebyshev series are each approximately of length T.)

By the design of matrices $\boldsymbol{\mathcal{L}}$ and $\boldsymbol{\mathcal{R}}$ constructed from the original problem, the sets of truncated Chebyshev series are themselves solutions to the matrix equation (3.2), with the same eigenvalue σ. Therefore if we can find solutions to (3.2) that match the expected form of truncated Chebyshev series describing functions $f_\alpha(x)$ then these solutions are also approximate solutions to (3.1).

Solving (3.2) will give a total of Q solutions, with Q equal to the size of the matrices $\boldsymbol{\mathcal{L}}$ and $\boldsymbol{\mathcal{R}}$. These solutions must be sorted through in order to find the results that are most relevant to the problem (3.1).

3.3.1 Spurious solutions

The truncated Chebyshev series of a function $f_\alpha(x)$ will exhibit exponential accuracy - this means that the error in the series will become exponentially smaller with each term that is added to the series. Furthermore, this means that each term in the series should be exponentially smaller than the previous terms, as there are smaller and smaller adjustments required to get closer to the 'ideal' solution. (This typically won't be true of the first few terms in the series, which are instead establishing the general structure of the eigenfunction.)

If a solution to (3.2), once broken down into individual Chebyshev series, does *not* exhibit this exponential decay, then it cannot be an accurate solution to (3.1). Since these solutions are not relevant to (3.1), they are spurious and must be filtered out.

These spurious solutions can originate from a variety of sources. They may be representations of solutions to the original problem that have insufficient terms in the Chebyshev expansion to be accurately modelled. There will also be some spurious solutions that are a result of how we handled zero rows in section 3.2.4. Alternatively, spurious solutions may arise that satisfy the matrix equation but are completely impossible in the context of the original problem, due to the subtle differences between the two.

Each individual solution to (3.2) will have A associated Chebyshev series. If even one Chebyshev series is deemed to be spurious, then the entire solution that the Chebyshev series belonged to is spurious. This is because we can only accept solutions to (3.1) for which all the eigenfunctions make sense.

Checking for spurious Chebyshev series

Consider a truncated Chebyshev series of length L. We can take the sum of the absolute magnitudes of the first $L/2$ terms of the series (rounding down) and compare it to the sum of the absolute magnitudes of the second $L/2$ terms. If the Chebyshev series exhibits the expected exponential decay in term magnitudes, then the first sum should be substantially larger.

Typically, we used a cut-off threshold of 10^{-5}; if the second half was not at least 10^{-5} times smaller than the first half, then the series was treated as spurious.

3.3.2 Relevant results

Having filtered out the spurious results, we are left with a set of approximate solutions to the original problem (3.1). Typically, we are still only interested in a select few of these results.

For example, in the case of perturbation instability analysis with a complex growth rate for an eigenvalue, we are most interested in solutions where the real growth rate is as large as possible. The set of solutions can be searched for the eigenvalue with the largest real part. If the largest growth rate is positive, the solution is considered to be a mode of instability. The associated eigenfunctions can then be converted into functions of x for analysis.

3.4 Eigenfunction solver program

All coding was done using MATLAB. An outer program *GenEig.m* was written to build the matrices $\boldsymbol{\mathcal{L}}$ and $\boldsymbol{\mathcal{R}}$ of (3.2). *GenEig.m* was written such that different sets of equations could be swapped in and out for different eigenfunction problems. These sets of equations would be supplied in the form of an *Eqns.m* file, such as *SRIEqns.m* for the viscous SRI problem. *GenEig.m* and each *Eqns.m* file were written such that the parameters of each problem could be individually varied for each evaluation.

The MATLAB routine *eig* was used to solve the matrix problem (3.2) once $\boldsymbol{\mathcal{L}}$ and $\boldsymbol{\mathcal{R}}$ had been constructed. Spurious filters were then applied, as described in section 3.3.1, yielding a list of valid eigenvalues and eigenfunctions.

3.5 Implementations

For this thesis, the methods described throughout this chapter were exclusively applied to fluid instability problems with independent variables $[r, \theta, z, t]$ or $[x, y, z, t]$. In our work, the eigenvalue σ always represents the complex growth rate of a perturbation mode, and we have instability whenever $\sigma_r > 0$.

This means that it was often useful, for a given set of parameters, to check for instability by finding the eigenvalue with the largest real component, and checking whether this was positive. It was also possible to optimise sets of parameters based around the eigenvalue, for example in order to find the largest possible σ_r, or where $\sigma_r = 0$.

Each problem typically had five eigenfunctions for any given eigenvalue σ. The coefficients for a given eigenfunction could be retrieved from the eigenvector, and converted back into an approximate form of the eigenfunction by summation of the truncated Chebyshev series. This would yield an exponentially small error in the form of the eigenfunction compared to the ideal solution. In this way, eigenfunctions of interest could be plotted for further inspection (see chapter 6).

3.5.1 Viscous SRI

For the viscous strato-rotational instability problem, the parameters are $[\eta, \mu, N, Re, m, k]$. The parameters η, μ and N are considered to be physical parameters, which can be controlled within physical experiments. Re can also be considered to be a physical parameter, as a non-dimensional measure of the ratio between inertial and viscous forces. However the Reynolds number can easily be varied in experiments by steadily increasing the rate of rotation, and we are often interested in the critical Reynolds number Re_c at which a system becomes unstable.

Unlike the other parameters, the wavenumbers m and k are unrestricted in reality; the system can 'choose' any $[m, k]$ pair that is unstable. This leads to two distinct approaches to computationally evaluating the system.

(i) If we are merely interested in finding out whether or not a given set of physical parameters $[\eta, \mu, N]$ can be made unstable, then no optimisation is required. We can set the Reynolds number Re to a significantly large value in order to activate any potential instabilities, and then scan through a reasonable range of $[m, k]$ pairs until such an instability is found or our range of $[m, k]$ pairs is exhausted. For our purposes we typically checked $Re = 1 \times 10^6$ for the ranges $0 \leq m \leq 3$ and $0 \leq k \leq 20$, although we would revise the upper limits of these ranges if nearby results in the parameter space required larger values of m or k to become unstable.

Note however that using a large value of Re requires a larger value of T to account for resolution of the eigenfunctions, which increases the computational run-time. For example, with $Re = 1 \times 10^6$, we tended to use $T = 230$, and had a computational run-time of about 40 seconds to evaluate a single set of parameters $[\eta, \mu, N, Re, m, k]$. This was considered an upper limit for T, as it made investigating large ranges of parameters take significant time.

This method relies upon the assumption that, if a mode of instability has some critical Reynolds number Re_c at which it becomes unstable, it will remain unstable for all $Re > Re_c$. However, as discussed in section 6.2.3, this is not always the case with the SRI. In the case of a closed domain loop, it is possible for an unstable mode to become stable with a Reynolds number that is too large. With this having been noted, a more thorough method could involve scanning through a set of potential Reynolds numbers for instability, but this would significantly increase the computational runtimes required. This is further complicated by the fact that the range of possible Reynolds numbers is continuous and has no upper limit.

For our own work, we found $Re = 1 \times 10^6$ to be suitable for recovering a great many unstable modes, but it is likely that this value of Re missed other modes requiring even larger Reynolds numbers.

(ii) We may instead wish to find the critical mode for a given set of physical parameters

$[\eta, \mu, N]$. This is the mode of instability which becomes unstable at the critical Reynolds number Re_c. (See section 2.4.6.)

We use a root-finding algorithm to find Re_{mk}, the critical Reynolds number at which a mode with some fixed $[m, k]$ reaches marginal stability with $\sigma_r = 0$. The root finding algorithm we used was a hybrid secant and bisection method.

We then use a minimisation algorithm to find the minimum Re_{mk} for a range of $[m, k]$-values. This algorithm worked by first scanning through a discrete range of $[m, k]$ pairs to find the minimum Re_{mk} within this range, and then improving this result by using MATLAB's fminsearch routine to optimise k further. We assume that this locally minimised Re_{mk} corresponds to the global critical Reynolds number Re_c if a sufficiently large range of m and k is scanned. The critical wavenumbers m_c and k_c correspond to the wavenumbers at which $Re_{mk} = Re_c$.

This method can alternatively be constrained to find Re_m, the critical Reynolds number for some fixed value of m but minimised over k.

Our viscous code has successfully reproduced results from Shalybkov and Rüdiger [2005] and Rüdiger and Shalybkov [2009]; see figure 3.3. A comparison to the recent experimental results of Ibanez et al. [2016] is shown later in this thesis in figure 5.2, and is discussed in section 5.3.2.

3.5.2 Inviscid SRI

For the inviscid strato-rotational instability problem, we lose the Reynolds number parameter, leaving $[\eta, \mu, N, m, k]$. Primarily for the inviscid system, we are merely interested in whether or not a given set of physical parameters $[\eta, \mu, N]$ can be made unstable for some $[m, k]$. The inviscid system typically required considerably smaller resolutions in T than the viscous system, reducing computational runtime.

However, the inviscid system introduces further complications due to computational error. In theory, due to the lack of viscous damping, many stable inviscid modes have zero growth rates, whereas only unstable modes have positive growth rates. However, computational and numerical errors allow stable modes in the inviscid domain to be measured

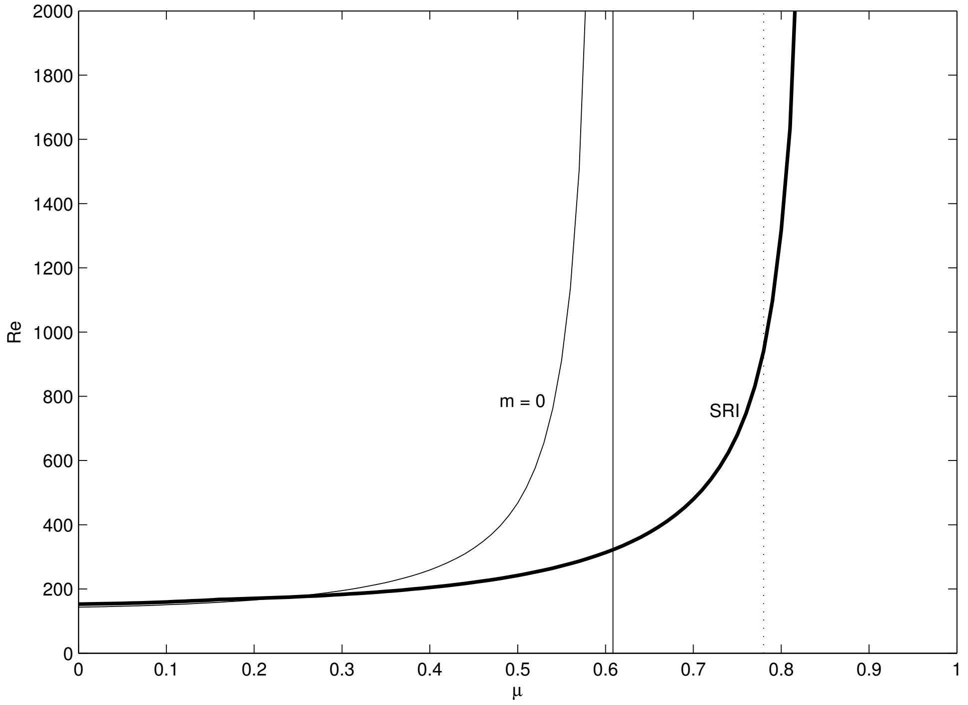

Figure 3.3: A reproduction and extension of figure 3 from Shalybkov and Rüdiger [2005], with $\eta = 0.78$ and $N = 2$. The solid vertical line represents the Rayleigh line $\mu = \eta^2$, whereas the dotted vertical line represents $\mu = \eta$, which was suggested as a stability limit of the SRI by Shalybkov and Rüdiger [2005]. Our data shows that this line is crossed by the SRI at a Reynolds number of about $Re = 1000$, which is consistent with the results of Rüdiger and Shalybkov [2009].

as having very small positive growth rates. These errors decrease with computational resolution, but they cannot be completely eliminated, and one advantage of working in the inviscid domain is to avoid the high resolutions required for a viscous computation. Thus for computationally evaluated inviscid modes, small positive growth rates measured by the program cannot be considered to be a reliable indication of instability. Nonetheless, large positive growth rates are still indicative of instability.

Therefore, inviscid results were only treated as potentially unstable if they had a real growth rate above a sufficient threshold, in order to rule out positive growth rates that were a result of computational error. A threshold of 1.0×10^{-5} was found to work well, as computational errors were typically of considerably smaller magnitude, and results above this threshold often also corresponded to unstable modes in the viscous domain. The difference between computational error and results where we are confident of inviscid instability can be seen in figure 3.4.

We typically only used $T = 40 - 70$ for inviscid system. Any potentially unstable results were then further tested by increasing up to $T = 200$. If an unstable result was present at the $T = 200$ high resolution, we would then check that the mode was well resolved. This was tested by further increasing to $T = 210$ and checking that the growth rate and frequency were not significantly changed compared to the $T = 200$. A result was only accepted as unstable if it was well resolved at this higher resolution.

Our inviscid code has successfully reproduced the results of Le Dizès and Riedinger [2010]'s figure 1; see our figure 4.1. Note that there is a difference of length-scale used, such that their $k/N = 30$ is equivalent to our $k = 600$. This plot was produced by fixing the quantities $[\eta, \mu, m, N]$ and varying k throughout the displayed range. For each value of k, the eigenfunction solver would produce multiple modes, for all of which the growth rate and frequency were plotted on the relevant graphs.

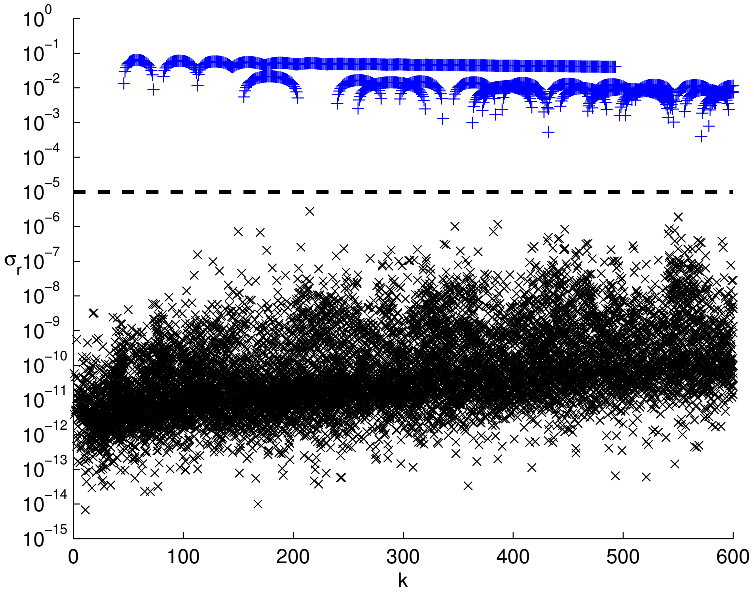

Figure 3.4: Growth rate σ_r plotted on a log scale against vertical wavenumber k. Results for which $\sigma_r > 10^{-5}$ are plotted with a blue '+', while results for smaller growth rates are plotted with a black 'x'. This figure uses the same data and parameters as figure 4.1(b). A significant difference in magnitude can be seen between the results of computation error (the 'noise' primarily focused in the range $\sigma_r \in [10^{-14}, 10^{-8}]$), and the results with which we are confident of inviscid instability (the blue '+' results for $\sigma_r > 10^{-5}$).

Chapter 4

Instability Domain

4.1 Introduction

We wish to know the domain of instability for the SRI at any given stratification N.

The line $\mu = \eta^2$ (see section 2.4.4) can be considered to be a stability limit of axisymmetric perturbations in co-rotating stratified Taylor-Couette flow. However, since the SRI is a non-axisymmetric instability, this stability limit does not apply, and can only be considered to be a sufficient condition for inviscid instability in the presence of stratification, not a necessary one.

Taking an analytic approach to near-narrow-gap co-rotating flows with high-stratification, Yavneh et al. [2001] concluded that $d(\Omega^2)/dr < 0$ was a sufficient condition for inviscid instability. This corresponds to $\mu < 1$, i.e. a stability limit of solid body rotation.

However, with numerical analyses of viscous flows with moderate gap widths and moderate stratification, Shalybkov and Rüdiger [2005] only found instabilities below the line $\mu < \eta$, and suggested this as an approximate stability limit. This work was extended for Rüdiger and Shalybkov [2009], with wide, modest and narrow gap flows ($\eta = [0.3, 0.5, 0.78]$) and a variety of stratifications. The stability limit appeared to be somewhere between $\eta < \mu < 1$ for modest and narrow gaps, whereas it appeared to be somewhere between $\eta^2 < \mu < \eta$ for wide gaps.

Later, Park and Billant [2013] found a sufficient condition for inviscid instability of strati-

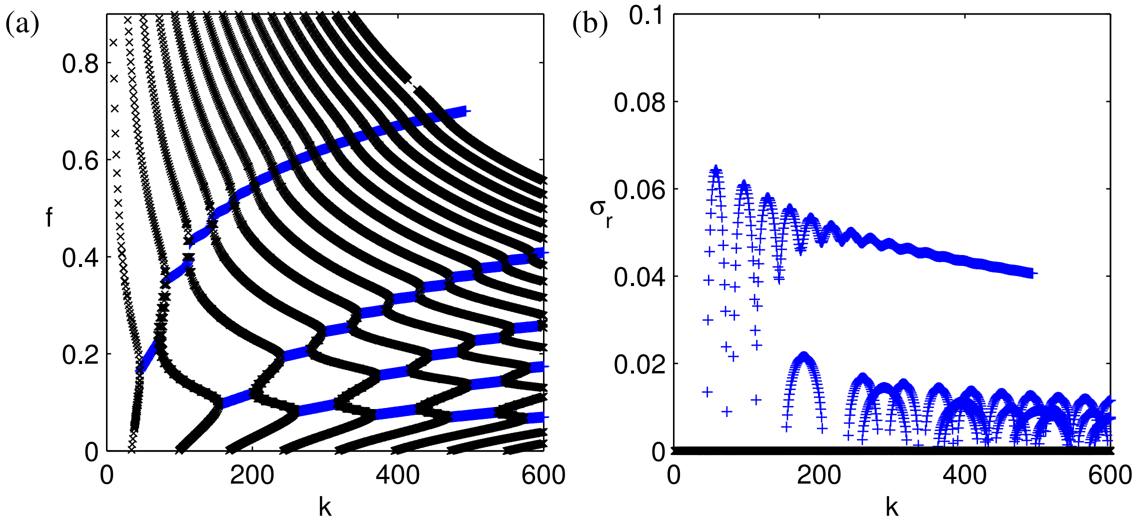

Figure 4.1: A reproduction of figure 1 from Le Dizès and Riedinger [2010]. Here $\eta = 0.2$, $\mu = 0.04$, $N = 5$ and $m = 1$. (Note that the symbol μ represents a different term in Le Dizès and Riedinger [2010].) The left-hand plot displays frequency f against the vertical wavenumber k, whereas the right-hand plot displays growth-rate σ_r against k for the same modes. Black crosses x represent stable modes, whereas blue plusses + represent unstable modes.

fied Taylor-Couette flows. This condition implied that any flow with $\mu \neq 1$ could be made unstable with sufficiently large N. Therefore Park and Billant [2013] extend the inviscid result of Yavneh et al. [2001] such that at sufficiently large N not only narrow gaps are unstable, but all gap sizes for $\mu \neq 1$.

In this chapter, we will further extend the work of Park and Billant [2013] in order to find a sufficient condition for inviscid instability on μ for any given η and N for the case $\mu < 1$. We will then give the results of a numerical search for viscous and inviscid instabilities for various stratifications, and compare these results to the theoretical predictions. Our numerical viscous results extend the work of Shalybkov and Rüdiger [2005] and Rüdiger and Shalybkov [2009] to a larger range of η and μ. We also find that there is a variation in the types of SRI, explored further in chapter 6.

4.1.1 Dual-Wave-Mode SRI

Yavneh et al. [2001] identified the presence of a non-axisymmetric Kelvin wave instability in stratified flows; this instability has come to be known as the SRI. However, in chapter 6

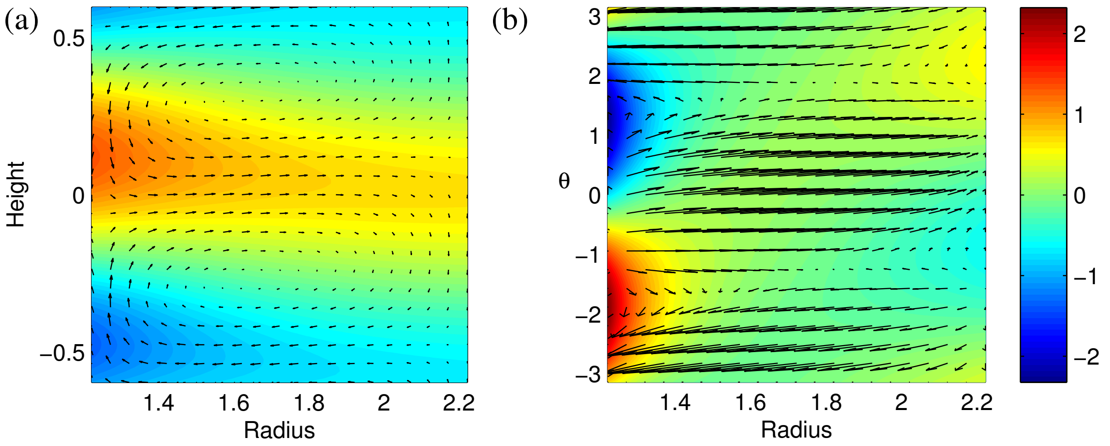

Figure 4.2: An example of the inviscid dual-wave-mode SRI for stratified Taylor-Couette flow, providing vertical (a) and horizontal (b) cross-sectional contour plots of the mode. The vertical cross-section (a) is taken at $\theta = 0$ whereas the horizontal cross-section (b) is taken at $z = 0$. For (a), radial and vertical velocities are shown as vectors, whereas the angular velocity perturbation is shown in colour contours with positive/negative represented by red/blue respectively. For (b), radial and angular velocities are shown as vectors and the vertical velocity is shown in colour contours. Colour contours are scaled against the maximum radial velocity perturbation. Here $\eta = 0.55$, $\mu = 0.31$ and $N = 1$, with optimised wavenumbers of $m = 1$ and $k = 5.27$. The frequency of the mode is $f = 0.546$, and the growth rate is $\sigma_r = 0.110$. Note that this figure correlates with figure D.1 which uses the same parameters.

we will show that there are multiple distinct forms of non-axisymmetric stratified instabilities, each of which could therefore be referred to as a strato-rotational instability. Some of these SRI forms, such as the radiative instability (discussed previously by Le Dizès and Riedinger [2010]) and the wide-gap-mode SRI, do not demonstrate the form of a Kelvin wave instability. Therefore, for the sake of distinction we will refer to the ‘classical’ SRI of Yavneh et al. [2001] as the dual-wave-mode SRI, since it relies upon the presence of two Kelvin waves each travelling adjacent to either the inner or outer radial boundary.

(For an analysis of how these waves can be referred to as Kelvin waves, see appendix C.)

It is this restriction, the presence of two interacting Kelvin waves travelling adjacent to each boundary, which leads to the distinctive growth rate ’bounces’ in figure 4.1(b) as the vertical wavenumber k is varied. Different values of k permit different inner and outer wave-modes, each with their own frequencies, and each with neutral growth rates. The rising curves in figure 4.1(a) correspond to waves travelling around the inner boundary, whereas the curves with falling frequency f compared to increasing k correspond to waves travelling around the outer boundary.

When the inner and outer waves both operate at the same value of k and approximately the same frequency, the interaction between the waves produces the dual-wave-mode SRI. This leads to bands of unstable k where the inner and outer frequencies are similar enough to interact together. When the individual frequencies are at their most similar, the instability has its strongest growth rate, hence why the unstable bands display 'bounces' in their growth rates, as the relevant frequencies converge and then diverge as k is increased.

Figure 4.2 provides an example of the inviscid structure of the dual-wave-mode SRI. The Kelvin wave structure is clearly visible in the horizontal cross-section, which shows alternating regions of strong vertical flow adjacent to each boundary. The vertical flow does appear to be stronger closer to the inner boundary for this example.

4.2 A Sufficient Condition for Instability [Park and Billant, 2013]

Park and Billant [2013] demonstrated that the inviscid system could always be made unstable to the dual-wave-mode SRI, provided that $\mu \neq 1$ and the conditions (4.1) and (4.2) are both satisfied:

$$2\sqrt{\frac{\mu-\eta^2}{1-\eta^2}} < N \quad \text{if} \quad \mu < 1; \qquad 2\sqrt{\frac{\mu\left(\mu-\eta^2\right)}{1-\eta^2}} < N \quad \text{if} \quad \mu > 1, \tag{4.1}$$

$$\frac{2}{\left|1-\sqrt{\mu}\right|}\sqrt{\frac{\mu-\eta^2}{1-\eta^2}} < m < \frac{2N}{\left|1-\mu\right|}. \tag{4.2}$$

Note that these conditions indicate that any combination of $[\eta, \mu]$ with $\mu \neq 1$ can potentially be made unstable, provided that the stratification N is large enough. The derivation of these equations is presented in appendix D.

Also note that these are only sufficient conditions for instability; we will show in section 4.3 that it can be possible to destabilise the flow when (4.1) and (4.2) are not mutually satisfied.

Equations (4.1) and (4.2) enable the dual-wave-mode SRI, which depends upon the existence of two wave-modes in the flow. Each of these wave-modes is adjacent to one of the cylinder walls, and they have Lagrangian frequencies of opposite sign.

The derivation does rely upon the validity of a WKBJ approximation for large k, and the approximation that the flow-region between the two wave-modes is not significantly smaller than the size of the wave-like regions.

The value of m in (4.2) must be a positive integer. It is possible that $\frac{2N}{|1-\mu|}$ could be larger than $\frac{2}{|1-\sqrt{\mu}|}\sqrt{\frac{\mu-\eta^2}{1-\eta^2}}$, but that no positive integer exists in the gap between them, in which case (4.2) could not be satisfied. However, if the gap between the two terms is greater than 1, there must be a positive integer that exists within this gap. Therefore, if the following modified condition (4.3) is satisfied, then we know that there must exist an integer m such that (4.2) is satisfied:

$$\frac{2}{|1-\sqrt{\mu}|}\sqrt{\frac{\mu-\eta^2}{1-\eta^2}}+1<\frac{2N}{|1-\mu|}. \tag{4.3}$$

4.2.1 Inviscid flow is Unconditionally Unstable if $\mu < 1$ and $N \geq 2$

As an extension of the work of Park and Billant [2013], we will now show that for $N \geq 2$, then (4.1) and (4.3) are satisfied for all μ in the range $\eta^2 \leq \mu < 1$. Since we know that inviscid axisymmetric modes are unstable for $\mu < \eta^2$, this will demonstrate the remarkable result that for $N \geq 2$ there is inviscid instability throughout the range $0 < \eta < 1$ and $0 \leq \mu < 1$.

Equation (4.1) is clearly satisfied for $N \geq 2$, since $\sqrt{(\mu-\eta^2)\,/\,(1-\eta^2)} < 1$ for $\eta^2 \leq \mu < 1$.

To show that (4.3) is also satisfied, we start from the following inequality:

$$\frac{\left(1-\sqrt{\mu}\right)^2}{2\left(1+\sqrt{\mu}\right)}>0. \tag{4.4}$$

This inequality is always satisfied since a square of a real number must be positive. We can expand (4.4) as:

$$\frac{4-2\left(1+\sqrt{\mu}\right)-(1-\mu)}{2\left(1+\sqrt{\mu}\right)}>0.$$

Multiplying through by $2/(1-\sqrt{\mu})$ allows us to conclude that:

$$\frac{4}{(1-\mu)} > \frac{2}{\left(1-\sqrt{\mu}\right)} + 1.$$

However if $N \geq 2$, then $2N/(1-\mu) \geq 4/(1-\mu)$. We also know from above that $\sqrt{(\mu-\eta^2)\,/\,(1-\eta^2)} < 1$. Therefore, for $N \geq 2$, we can conclude the following:

$$\frac{2N}{(1-\mu)} \geq \frac{4}{(1-\mu)} > \frac{2}{\left(1-\sqrt{\mu}\right)} + 1 > \frac{2}{\left(1-\sqrt{\mu}\right)}\sqrt{\frac{\mu-\eta^2}{1-\eta^2}} + 1.$$

This yields (4.3). We can therefore conclude that (4.3) is always satisfied for $N \geq 2$.

Therefore $N \geq 2$ is sufficient to establish that both (4.1) and (4.3) hold, and hence that (4.2) also holds, and therefore there is inviscid instability everywhere for the range $0 < \eta < 1$ and $0 \leq \mu < 1$.

4.2.2 Conditions for Instability if $\mu < 1$ and $N < 2$

In appendix E we derive a set of conditions for instability upon η and μ for any given N. This serves as a further extension of the work of Park and Billant [2013]. The resulting conditions on η and μ are summarised in figure 4.3 as a flowchart. The following quantities are defined:

$$\begin{aligned}
\mu_0 &= \eta^2 + \left(\frac{1-\eta^2}{4}\right) N^2, \\
\sqrt{\mu}_1 &= 1 - \sqrt{2\,(2-N)}, \\
\sqrt{\mu}_2 &= \frac{1}{3}\left(-1 + \sqrt{2\,(2-3N)}\right), \\
\sqrt{\mu}_3 &= -1 + \sqrt{2N}, \\
f_1 &= -\left[4N^2 - 4N\,(1-\mu) - 4\,(1+\sqrt{\mu})^2 + (1-\mu)^2\right], \\
f_2 &= 3\mu^2 + 8\mu\sqrt{\mu} - 2\,(2N-3)\,\mu - (2N-1)^2.
\end{aligned}$$

It should be noted that, since we evaluated (4.3) rather than (4.2), there may be some rare cases where dual-wave-mode SRI can become active even when the derived set of conditions would predict otherwise. However, such cases will always be very close to the predicted domain of instability from these conditions.

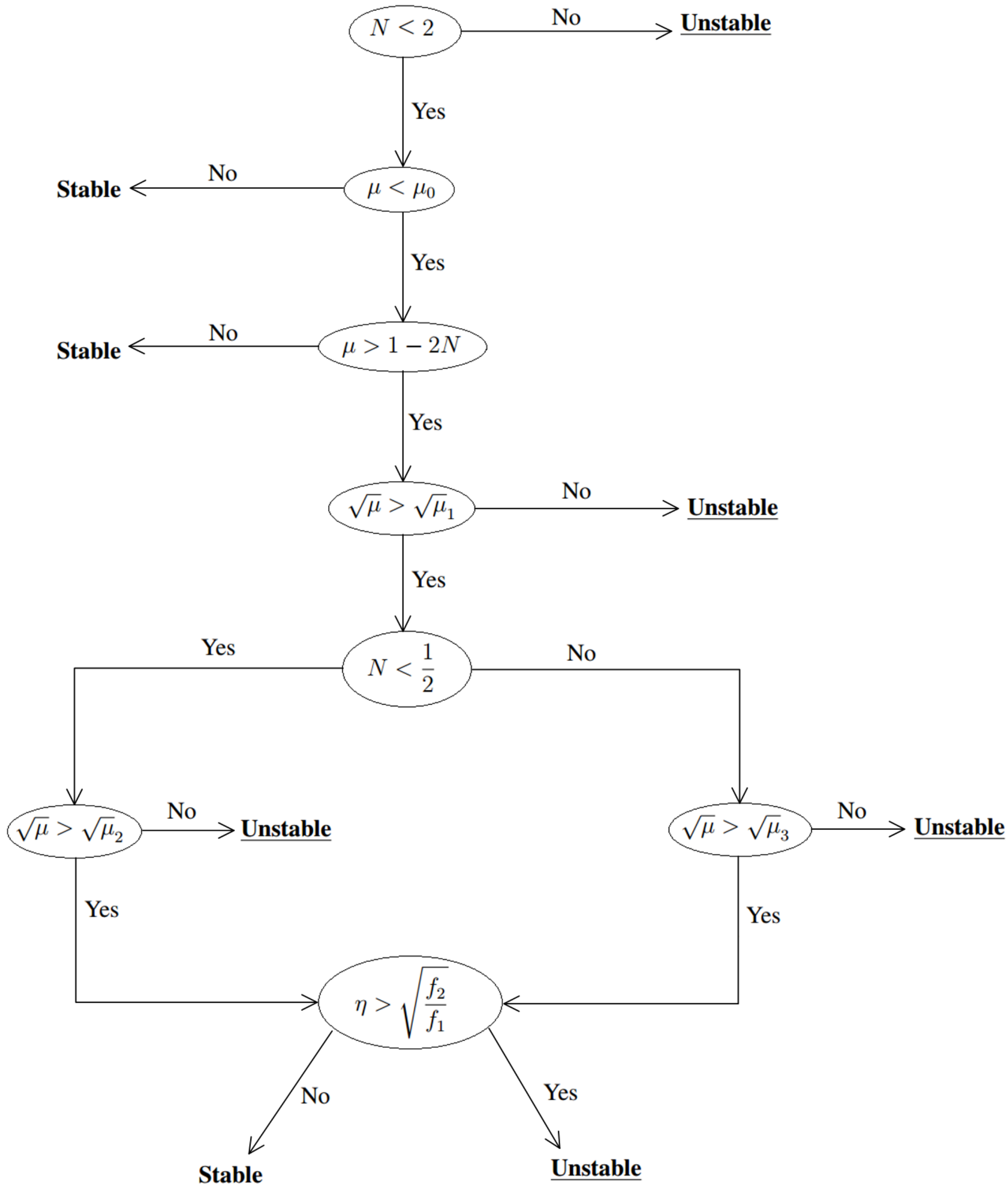

Figure 4.3: The tree of conditions for an inviscid flow with a given stratification N to be destabilised by dual-wave-mode SRI. Note that if the result is 'Stable' it simply means that the flow is stable with regard to the dual-wave-mode SRI, and not necessarily stable in general. Furthermore, this chart is only applicable for $0 < \eta < 1$, $\eta^2 < \mu < 1$ and $0 < N$.

4.3 Numerical search for Instability

To test the previously suggested stability limits with various values of the buoyancy frequency N, we took a brute force approach, performing a direct numerical search for unstable modes throughout the parameter space of $0 < \eta < 1$ and $0 < \mu < 1$. This numerical search was performed upon a grid across the $[\eta, \mu]$-parameter space with the grid points being spaced by a difference of 0.05 in either parameter. We used the computational methods described in section 3.5 to find both inviscid and viscous modes of instability. The viscous domain was typically scanned at $Re = 1.0 \times 10^6$, although in some case instabilities were only found for smaller Reynolds numbers.

Each numerical search began from the grid-location $\eta = 0.95$, $\mu = 0.05$, which was a consistently unstable point in the parameter space. The search for unstable modes would then proceed throughout the grid. At each grid-point, the parameters of adjacent unstable modes were used as initial guesses to seek an unstable mode at the current point. The inviscid computations were done first, and these results were used as a guide for the viscous computations.

4.3.1 Results

As can be seen from Figure 4.4, we have not confirmed the unconditional instability expected for flows with $N \geq 2$. The possible reasons for this discrepancy between the analytic and computational results are discussed later in this section.

Figure 4.4 does provide counter-examples to the earlier suggested SRI stability limit of $\mu < \eta$ [Shalybkov and Rüdiger, 2005], in addition to those provided by Rüdiger and Shalybkov [2009] and Ibanez et al. [2016]. We therefore conclude that, while the $\mu < \eta$ stability limit is a good first order guess for the stability limit of viscous stratified flows, it does not stand up to careful analysis. Interestingly, our wide gap results also do not match up with those of Rüdiger and Shalybkov [2009], who with $N = 2.0$ and $\eta = 0.3$ saw no instabilities beyond $\mu = 0.24$. However, in figure 4.4(c) we instead see instabilities up to $\mu = 0.35$. This would appear to be because we are allowing considerably larger Reynolds

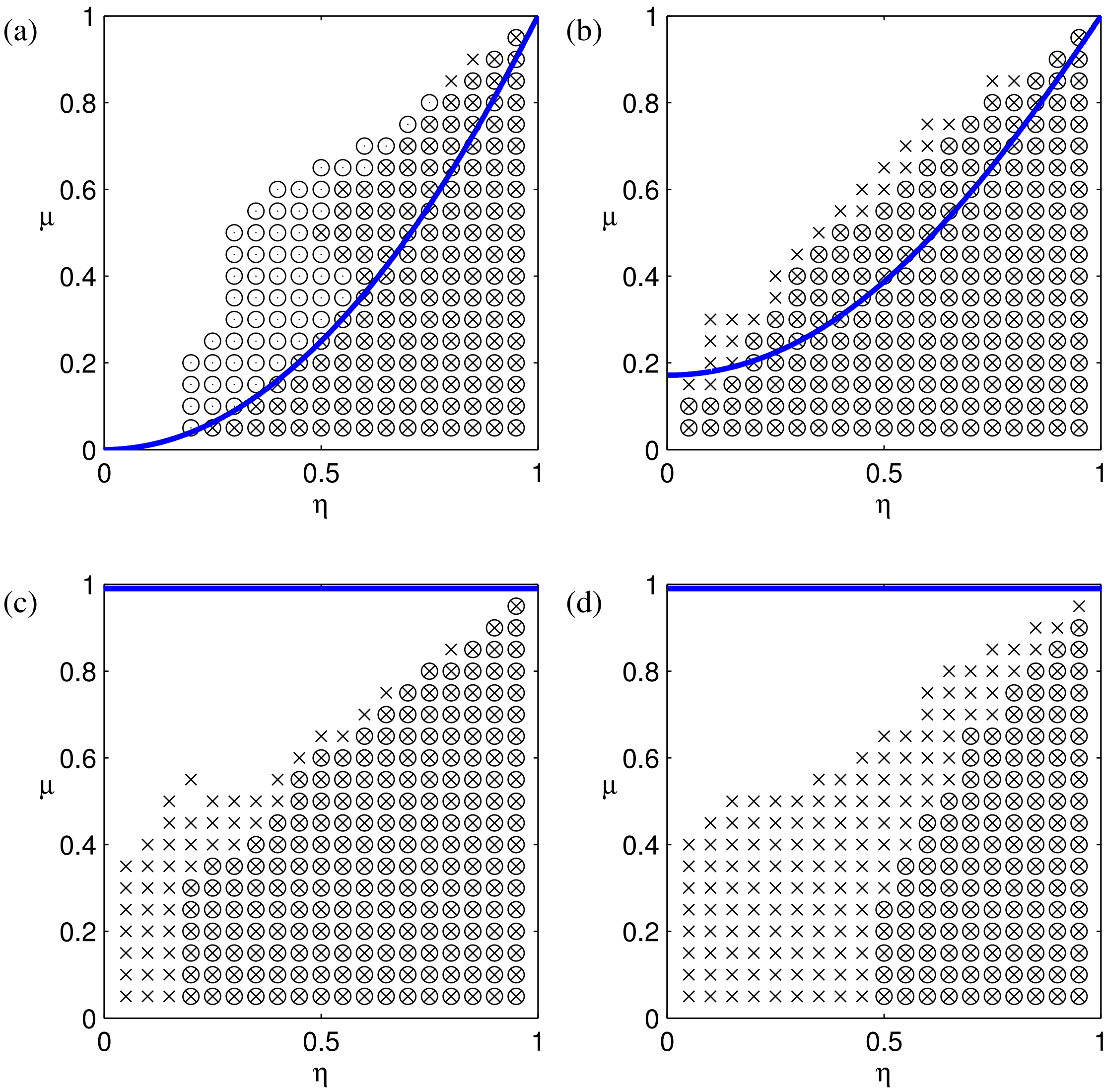

Figure 4.4: (a)$N = 0.3$, (b)$N = 1.0$, (c)$N = 2.0$, (d)$N = 5.0$; arranged in order of increasing stratification. These plots display the inviscid and viscous unstable modes found for $0 < \eta < 1$ and $0 < \mu < 1$ for various stratifications. Here $'\times'$ represents locations where we have found inviscid instabilities; 'o' represents locations that are viscously unstable for a Reynolds number of $Re = 1.0 \times 10^6$. The blue line on all four plots shows the extent of the inviscid instability as predicted by figure 4.3; below this line is predicted to be unstable to the dual-wave-mode SRI. Note that in plots (c) and (d) the entire domain of $\mu < 1$ is predicted to be inviscidly unstable.

numbers than were examined by Rüdiger and Shalybkov [2009], who only looked at $Re < 1500$ for $\eta = 0.3$.

In most cases (figure 4.4 (b),(c),(d)) we see a strong correlation between the viscous and inviscid results, although there are locations in the $[\eta, \mu]$-parameter space where the inviscid system is unstable but the viscous system appears stable. Since we are only checking viscous instabilities up to $Re = 1.0 \times 10^6$, these locations may just correspond to regions that require an even larger Reynolds number for instability.

Weak Stratification

In figure 4.4 (a) with a weak stratification of $N = 0.3$, we see regions of the parameter space where the system is viscously unstable but inviscidly stable. The boundary of the inviscidly unstable region also exhibits an 'overhang' appearance.

This overhang does appear to be genuine, at least to the limit of our computational abilities. To check, we increased the computational resolution up to $T = 200$ for the entire brute force inviscid instability search at $N = 0.3$. (We still confirmed each unstable result was well resolved, see section 3.5.2 for details.) The higher resolution only slightly increased the range of results compared to the standard $T = 70$ search, and it is the $T = 200$ results that are displayed in the figure. The overhang also was not influenced by increasing the range of available $[m, k]$-wavenumbers, and its existence appears to be related to the critical radial layer mentioned below.

Closer examination of the inviscid system suggests that the lack of inviscid instability in the viscously unstable region is due to a critical radial layer entering the radial range. While investigating the aforementioned overhang in the inviscid results, we examined the boundary of the inviscidly unstable domain, where the system transitions to purely viscous instabilities. For inviscid flows at this boundary, a radial layer for which $\Phi^2 - N^2 = 0$ moves inside the radial range of the fluid.

The reciprocal of this $\Phi^2 - N^2$ term appears in the combined inviscid equation (2.48). If equations (2.44) and (2.45) are combined, eliminating ρ, it can be seen that a radial layer for which $\Phi^2 - N^2 = 0$ will produce a singularity in w if $P \neq 0$ (see (A.6)). The flow is therefore increasingly difficult to computationally resolve as Φ^2 approaches N^2, and impossible to resolve when they are equal. It is unclear why the system is unable to select a mode with $P = 0$ at this radial layer.

It would appear that the critical layer does not arise in the viscous system. With small diffusion, the singularity is smoothed out, such that the flow can be made viscously unstable. However for inviscid flows, this singularity prevents a solution from forming.

We have only ever found this radial layer for small stratifications. However, since it results in significant differences between the viscous and inviscid systems, we may conclude that inviscid analysis can be unreliable for weak stratification.

This radial layer is discussed by Riedinger et al. [2010] and Le Dizès and Riedinger [2010], who refer to it as a stabilising singularity seen for sufficiently large Froude numbers. It is also seen by Leclercq et al. [2016] for their radiative instability result, also at a weak stratification, and similarly arises in figure 6.12 of this thesis for the radiative instability.

Comparison to Predictions

In figures 4.4 (a) and (b) we see a good correlation between the theoretical predictions of inviscid instability from figure 4.3 and the numerical results; inviscid instability is always present within the domain that is predicted to be inviscidly unstable. In both cases, inviscid instabilities do extend beyond the theoretical predictions; this indicates that there are other strato-rotational instabilities that do not rely on the system of instability explored by Park and Billant [2013]. In the next chapter we shall see further evidence of different types of strato-rotational instability.

In figures 4.4 (c) and (d), the entire $[0 < \eta < 1,\ 0 < \mu < 1]$ domain is predicted to be inviscidly unstable, according to the inequalities derived earlier in this chapter. However, our numerical results do not correspond to this. The domain of numerical inviscid instability does appear to expand slightly as N is increased, but in neither case does it fill the domain, leaving the top left corner $[\eta \approx 0; \mu \approx 1]$ empty.

The discrepancy between predictions and numerical results for figures 4.4 (c) and (d) appears to be the result of the limited nature of the numerical analysis. It is noted in appendix D that dual-wave-mode SRI depends upon the existence of two wave-like regions, each adjacent to one of the boundary walls. This can only be achieved for a finite range of frequencies, and the conditions (4.1) and (4.2) guarantee the existence of this range. As one moves into the domain space of wide-gaps and near-solid-body rotation (i.e. $[\eta \approx 0; \mu \approx 1]$), then at viable frequencies for both regions to exist, the inner wave-like region becomes increasingly small in the radial domain. An example is shown in Figure 4.5.

The inner-wavelike region does always exist so long as $\eta > 0$ and $\mu < 1$ and the conditions for instability are satisfied, although the range of unstable m wavenumbers grows to higher and higher values. The reduced radial size of the wave-like region requires increasingly large computational resolutions to resolve as $\eta \to 0$ and $\mu \to 1$. This makes the computational detection of instability increasingly difficult as one moves into the wide-gap and near-solid-body region, and would explain why the inviscid results of figures 4.4 (c) and (d) do not match up to our derived inviscid prediction that the entire $\mu < 1$ domain is unstable for $N \geq 2$. In this region, it would appear that the problem of detecting instability is ill-suited to a brute force computational approach.

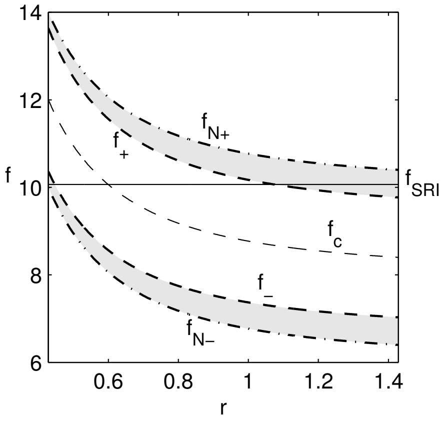

Figure 4.5: Similar to figure D.1. The lines $f_{N\pm}$ (dot-dashed) and $f_{\pm}$ (dashed) are plotted (see Appendix D), for $\eta = 0.3$, $\mu = 0.7$, $m = 12$, and $N = 2.0$. Also plotted is the line f_c (thin dashed line) at which the real part of Φ changes sign. Shaded regions denote where the flow has wave-like properties. The constant line $f = f_{SRI}$ gives an example frequency for which both wave-like regions exist. Note that for these parameters, then at $f = f_{SRI}$ the inner wave-like region is very small compared to the central evanescent region and the outer wave-like region.

Chapter 5

Experimental Review

A handful of experimental investigations into rotating stratified flows have been performed. In this chapter we review their results, and in one case compare our viscous numerical results to the experimental results of the appropriate paper.

5.1 Le Bars and Le Gal [2007]

Le Bars and Le Gal [2007] performed an experimental follow-up to the numerical SRI work of Shalybkov and Rüdiger [2005], and in so doing provided the first experimental confirmation of the SRI's existence.

Their system had a radius ratio of $\eta = 0.8$, with $\hat{r}_{\text{in}} = 55\text{mm}$ and $\hat{r}_{\text{out}} = 69\text{mm}$, yielding a gap width of $\hat{\lambda} = 14\text{mm}$. The vertical height of the system was $\hat{h} = 168\text{mm}$. Stratification was achieved by way of a salt solution using the double bucket method described by Oster [1965]. The cylinders could be individually spun, allowing complete control over the Reynolds number and allowing rotation ratios throughout the range $0 \leq \mu \leq 1$.

The radius ratio was chosen for the sake of comparison to the radius ratio $\eta = 0.78$ results of figure 3 from Shalybkov and Rüdiger [2005].

The Froude number was fixed at $Fr = 0.5$, by way of controlling $\hat{\Omega}_{\text{in}}$ and $\hat{N}$. Ten different values of the Reynolds number Re are used, ranging from $Re = 339$ up to $Re = 1210$. Their results provided excellent correlation with the numerical results of Shalybkov and

Rüdiger [2005] (see their figure 2 for the comparison). Throughout their experiments they saw values of m ranging from 1 to 5, mostly at $m = 1$ (see their figure 4). The largest value of μ for which instability was seen was $\mu \simeq 0.76$.

5.2 Riedinger et al. [2011]

Riedinger et al. [2011] performed an experimental follow-up to the numerical Radiative Instability (RI) work of Le Dizès and Riedinger [2010] (see section 1.2.1), providing experimental verification of the RI's existence. We discuss the RI further in section 6.3.

The experiment was performed in a wide rectangular tank with horizontal dimensions 240cm × 74cm and a height of 48cm, with a central rotating cylinder. The tank was filled up to a depth of 45cm. Three different cylinder sizes were used, with radii of $\hat{r}_{\text{in}} = 12.5$mm, 15mm, and 20mm. Stratification was again achieved using a salt solution and the double bucket method. A shadowgraph with a screen of tracing paper was used to capture detailed images of the flow.

The RI was observed for Reynolds numbers ranging from $Re = 295$ to 800 and Froude numbers ranging between $Fr = 0.5$ to 2.5. Their figure 9 compares the experimental (a) and numerical (b) modal forms of the instability, showing strong agreement. Furthermore, their figure 10 compares their numerical line of critical stability to their experimental results, showing a decent level of agreement.

The experimental system had nonlinear properties each time that the cylinder was accelerated up to a given rotational rate. These were present due to the lack of an external boundary, since the flow could not be kept in stable solid body rotation whilst being accelerated. These non-linear effects were not be accounted for in their numerical theory, however Riedinger et al. [2011] still saw a strong correlation between their numerical and experimental results.

5.3 Ibanez et al. [2016]

Using sodium polytungstate salt, Ibanez et al. [2016] were able to achieve stronger density concentrations, and therefore large values of $\hat{N}$ while maintaining a large aspect ratio.

Their system had a radius ratio of $\eta = 0.877$, with $\hat{r}_{\text{in}} = 4.218\text{cm}$ and $\hat{r}_{\text{out}} = 4.811\text{cm}$, yielding a gap width of $\hat{\lambda} = 0.593\text{cm}$. The vertical height of the system was $\hat{h} = 25.6\text{cm}$. Two syringe pumps were used to stimulate the stratification, one containing fresh water and the other a sodium polytungstate solution. The rotation rates of the two cylinders could again be individually controlled.

A range of stratifications $\hat{N} = 1.57\text{s}^{-1}, 3.14\text{s}^{-1}$ and 4.71s^{-1} were tested. The system would be taken up to a given Reynolds number whilst maintaining solid body rotation ($\mu = 1$), at which point the outer cylinder would be slowed so as to reduce μ. The value of μ for which onset of instability occurred was noted for various values of Re for each stratification (see their figure 2).

Notably they discovered that comparatively large Reynolds numbers can actually stabilise the SRI for a given value of μ. We see similar results in chapter 6, and discuss the phenomenon in section 6.2.3. Ibanez et al. [2016] also discovered a non-periodic mixing instability at high Reynolds numbers, close to the line $\mu = \eta^2$. Their results are shown in figure 5.1, which is a direct reproduction of figure 2 from Ibanez et al. [2016].

5.3.1 Violating the Centrifugal approximation

At large Reynolds numbers the experiment of Ibanez et al. [2016] did not satisfy the centrifugal approximation $\hat{r}_{\text{in}}\hat{\Omega}_{\text{in}}^2/\hat{g} \ll 1$ noted by Shalybkov and Rüdiger [2005]; however Ibanez et al. [2016] do not comment on this detail. Their results include a domain where the centrifugal force would have been larger than the gravitational force, such that a purely vertical stratification would not have been possible. Interestingly they still found the SRI to be present, suggesting that, while the centrifugal approximation is useful from a mathematical perspective, from an experimental perspective the approximation is not necessary in order to find the SRI.

To demonstrate this inequality, consider that Reynolds numbers in the range $100 \leq Re \leq 14000$ were used, with a sodium polytungstate solution in water. This solution had approximately the kinematic viscosity of distilled water, $\hat{\nu} = 1.0 \times 10^{-6}\mathrm{m}^2\mathrm{s}^{-1}$. In combination with the dimensions of their experiment, this allows us to calculate the range of rotation rates used, since $\hat{\Omega}_{\text{in}} = \hat{\nu} Re/\hat{r}_{\text{in}}\hat{\lambda}$, and $\hat{\nu}/\hat{r}_{\text{in}}\hat{\lambda} \simeq 0.0040\mathrm{s}^{-1}$. The calculations proceed as follows:

$$100 \leq Re \leq 14000,$$

$$0.40\mathrm{s}^{-1} \leq \hat{\Omega}_{\text{in}} \leq 56.0\mathrm{s}^{-1},$$

$$0.0007 \leq \frac{\hat{r}_{\text{in}}\hat{\Omega}_{\text{in}}^2}{\hat{g}} \leq 13.5.$$

As can be seen, at larger Reynolds numbers the centrifugal force is considerably larger than the gravitational force. The centrifugal approximation would require it to be negligibly small compared to gravity. A rotation rate of $\hat{\Omega}_{\text{in}} = 15.3\mathrm{s}^{-1}$ would yield a centrifugal acceleration $\hat{r}_{\text{in}}\hat{\Omega}_{\text{in}}^2$ approximately equal to that of the gravitational acceleration $\hat{g} = 9.81\mathrm{ms}^{-2}$; this means that the two forces are approximately equal for Reynolds numbers of around $Re \simeq 3800$, with the centrifugal force stronger for larger Reynolds numbers.

We note that larger values of $\hat{r}_{\text{in}}$ and $\hat{d}$ would reduce the necessary $\hat{\Omega}_{\text{in}}$ required to achieve any given value of Re, which may allow the experiment to be made consistent with the analytical approach. However, this would likely require reducing the aspect ratio of the experiment, as there are physical constraints due to the maximum possible solution density of sodium polytungstate.

5.3.2 Numerical comparison

Using the eigenfunction code described in chapter 3 of this thesis, we performed a numerical reproduction of Ibanez et al. [2016]'s results. This involved a grid-based search for instability throughout the $[\mu, Re]$-parameter space presented in figure 5.1, with a fixed value of η, the appropriate three values of N, and varying the wavenumbers $[m, k]$ throughout a reasonable range. A tighter grid was used in regions of the parameter space where the instability would switch on or off, ultimately yielding errors of $\delta\mu = 0.001$ and $\delta Re = 100$.

It was also necessary to convert from the SI units of the experiment to the dimensionless terms used throughout this thesis, which required that we recalculate the value of $\hat{\Omega}_{\text{in}}$ at each new value of Re.

Notably, the physical experiments had a fixed vertical height whereas our numerical analysis assumes that the system is unbounded in the vertical direction. Our unbounded results are shown in figure 5.2 with the symbol $'\text{o}'$; we get a good correlation to the results of Ibanez et al. [2016] for Reynolds numbers of $Re \leq 1000$. Our unbounded results appear to permit a slightly larger domain of instability for higher Reynolds numbers.

We repeated the numerical computation while restricting the range of available k. It was decided that k could not go smaller than the value $k_{min} = 0.2895$, which allows for a maximum vertical wavelength which would fit twice into the vertical height of the experiment. These results are shown with the symbol $'\times'$ on figure 5.2. These restricted-k results provide a stronger correlation to the experimental results of Ibanez et al. [2016], but are still not perfect at higher values of Re. This discrepancy is likely down to the experimental violation of the centrifugal assumption, as noted in the previous subsection.

5.4 Rüdiger et al. [2017]

Rüdiger et al. [2017] performed both numerical and experimental analyses of the SRI. Rather than using a salt stratification, their experiment instead made use of a temperature gradient to stimulate stratification in the system.

Their system had a radius ratio of $\eta = 0.52$, with $\hat{r}_{\text{in}} = 7.5$cm and $\hat{r}_{\text{out}} = 14.5$cm, yielding a gap width of $\hat{\lambda} = 5.0$cm. The vertical height of the system was $\hat{h} = 70.0$cm. Hot and cold endplates were used to provide the temperature gradient, with the hot endplate at the top of the experiment. The rotation rates of the two cylinders could again be individually controlled. Their numerical simulations also worked exclusively with $\eta = 0.52$. To measure the stratification against the viscosity, they introduced a stratification Reynolds number $Rn = \hat{N}\hat{r}_{\text{in}}\hat{\lambda}/\hat{\nu}$. Their numerical code avoided circumstances where endplate shear layers could become unstable.

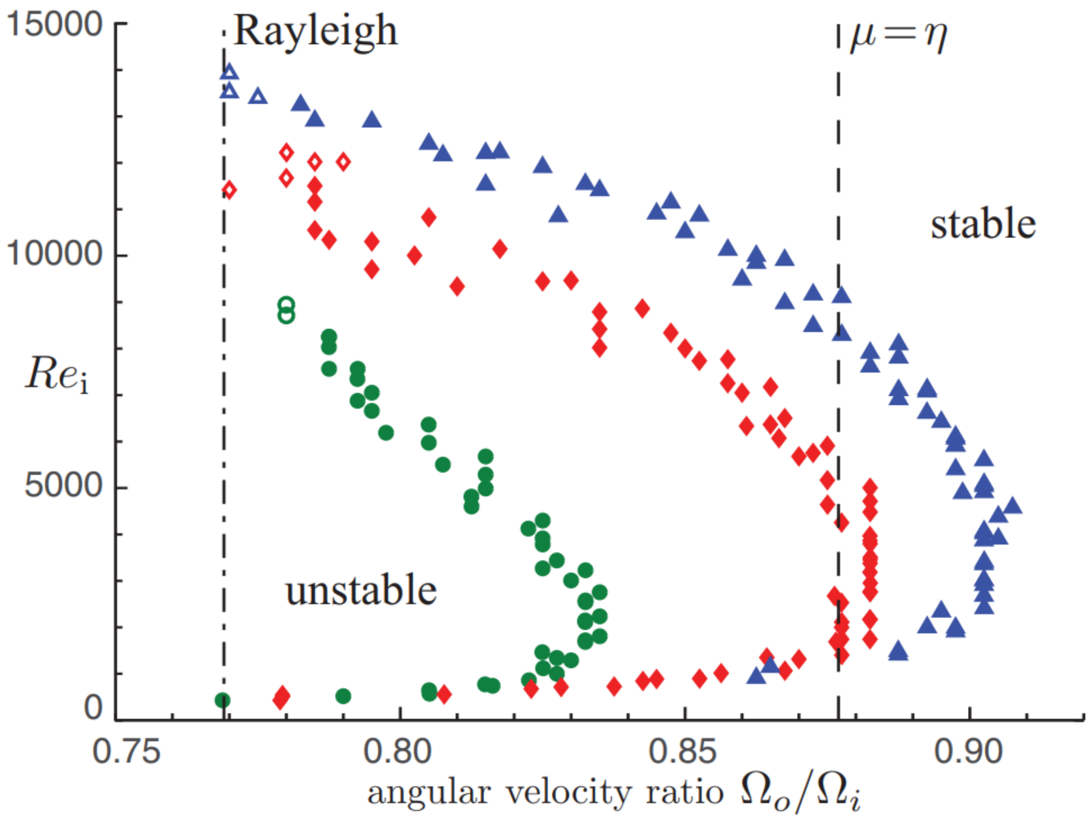

Figure 5.1: A direct reproduction of figure 2 from Ibanez et al. [2016], used with permission, and included here for the sake of comparison to figure 5.2. The experiment is described in detail in the main text. These are experimental results for the onset of the SRI with $\eta = 0.877$, as μ is reduced away from solid body rotation ($\mu = 1$) and the inner Reynolds number Re_i is held fixed. (The inner Reynolds number Re_i of Ibanez et al. [2016] is equivalent to the Reynolds number Re used throughout this thesis.) A wide range of Reynolds numbers were tested, with three distinct stratifications: green circles, $N = 1.57\mathrm{s}^{-1}$; red diamonds, $N = 3.14\mathrm{s}^{-1}$; blue triangles, $N = 4.71\mathrm{s}^{-1}$. Unfilled symbols represent a non-periodic instability found near to the Rayleigh line. The dashed line represents the suggested stability limit $\mu = \eta$ of Shalybkov and Rüdiger [2005], whereas the dot-dashed line represents the Rayleigh line $\mu = \eta^2$.

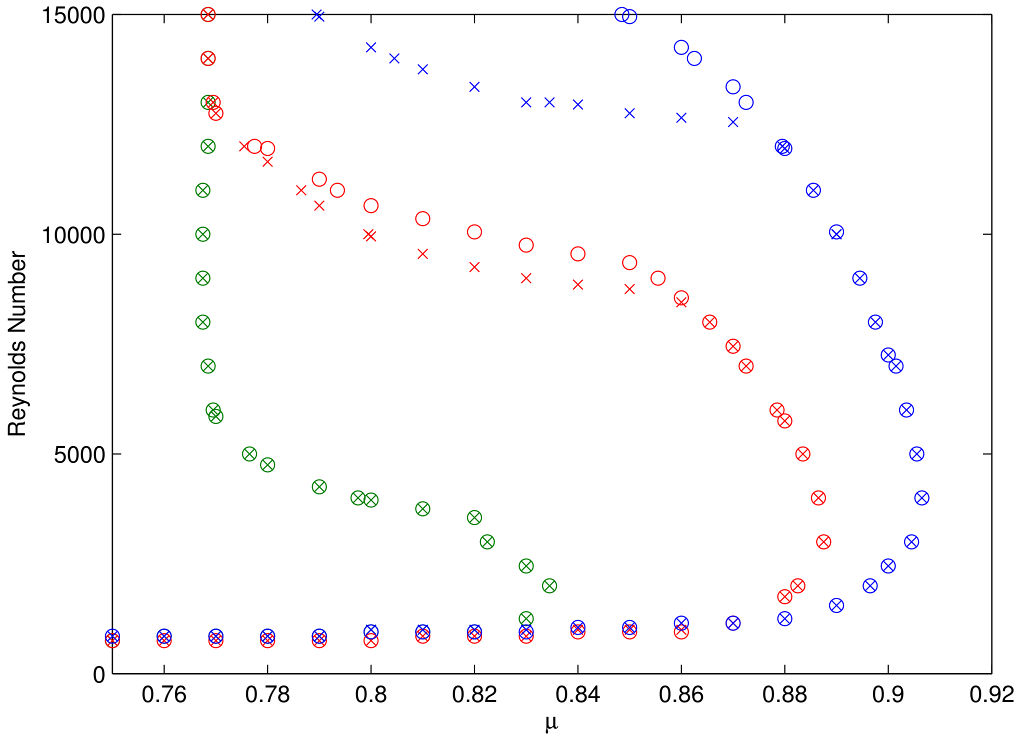

Figure 5.2: A reproduction, using our numerical code, of the experimental data shown in figure 5.1 from Ibanez et al. [2016], with radius ratio $\eta = 0.877$ and viscosity $\nu \simeq \nu_{water}$. Three values of the stratification are displayed; the green symbols represents $\hat{N} = 1.57\text{s}^{-1}$, red 3.14s^{-1} and blue 4.71s^{-1}. The figure displays where the flow becomes unstable as μ is reduced away from solid body rotation. Results shown with the symbol 'o' are unbounded on k, whereas results shown with the symbol $'\times'$ represent cases where we restricted the range of available vertical wavenumbers k such that vertical wavelengths would always fit at least twice into the experimental scale-height. Note that, since $N = \hat{N}/\hat{\Omega}_{\text{in}}$, the values of the dimensionless buoyancy frequency in this plot are typically considerably smaller than those used elsewhere in this thesis.

Similar to Ibanez et al. [2016], they found that higher Reynolds numbers could sometimes stabilise the flow. These results are compiled in their figures 7 and 8, for which they see a decent agreement between their numerical and experimental results. In the $[Re, Rn]$-parameter space, they numerically demonstrated the existence of a closed domain loop of instability as μ was increased - this was an instability region which ultimately shrank and vanished at around $\mu \simeq 0.571$ for $N = 1$ (see their figure 6). However, this closed domain loop does not appear to have been checked experimentally. Closed domain loops are further discussed in section 6.2.3 of this thesis.

Interestingly, their numerical results indicated that the SRI was restricted to only exist for the approximate range $0.3 < Fr < 5.5$. This numerical result was found for $\eta = 0.52$, $\mu = 0.27$ and $m = 1, 2, 3$, within the ranges $0 \leq Re \leq 1000$ and $0 \leq Rn \leq 2000$.

Chapter 6

Eigenfunction appearance

In this chapter, we explore the eigenfunction appearance of the critical viscous mode (defined in section 2.4.6) throughout the $[\eta, \mu]$-parameter space for $N = 1.0$. Using the algorithms described in section 3.5.1, we found the critical mode of instability for each unstable viscous point identified in figure 4.4(b) (for which $N = 1.0$). We then directly looked at the eigenmode structure for each critical mode. (The method used to recover the form of individual eigenfunctions is described in section 3.5.)

We also explored the $[m, k, Re]$-parameter space near to each viscous critical mode, seeking the line of critical stability where modes transition from stable to unstable. These viscous $[m, k, Re]$ results were then compared to unstable modes found in the corresponding inviscid $[m, k]$-parameter space, in order to examine the connections and differences between the viscous and inviscid systems.

6.1 Critical mode analysis

Figure 6.1 shows the distinct critical mode regions throughout the $[\eta, \mu]$-parameter space for $N = 1.0$. It can be seen that the critical mode changes in appearance as one moves throughout the $[\eta, \mu]$-parameter space, for which we have labelled the different critical mode regions as (α)-(ϵ). Examples of the critical modes found within these regions are shown in figures 6.2 to 6.8.

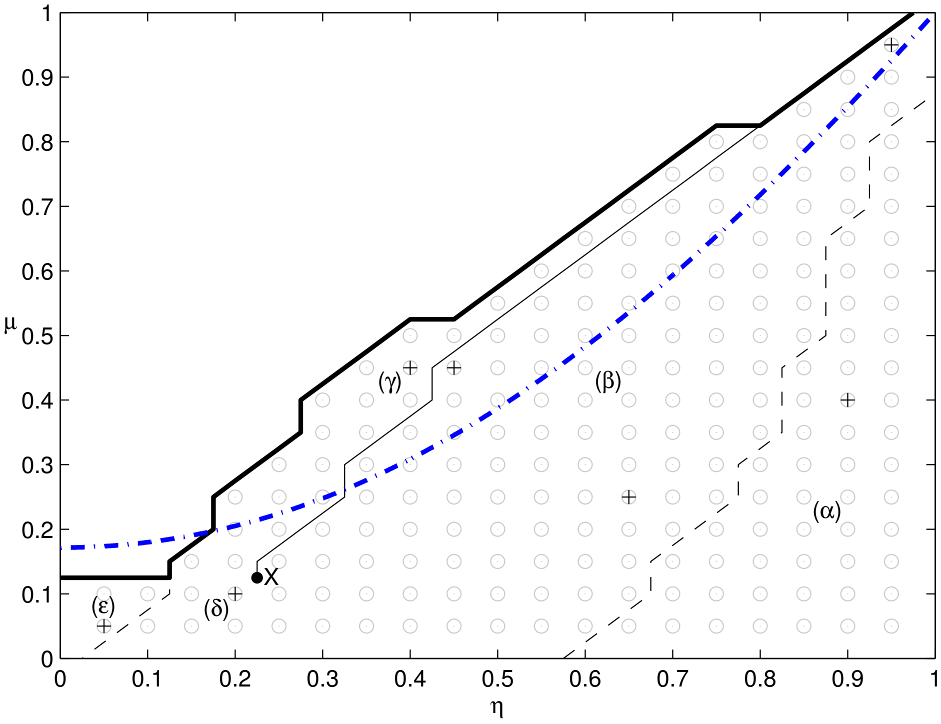

Figure 6.1: A copy of the viscous modes from Figure 4.4(b), the instability domain plot for $N = 1.0$. Here we have shown the different regions of the parameter-space dependent upon the form of the critical mode at each point. Solid lines denote discontinuous changes in the critical Reynolds number Re_c of the instability mode; dashed lines denote changes where the critical mode of instability does change, but Re_c is continuous. The thick black line denotes the apparent stability limit for modes with a Reynolds number below $Re = 1.0 \times 10^6$. Regions (α)-(ϵ) are labelled and are discussed in the main text, as is the point of continuity X. The black lines are only accurate to within 0.05 in η or μ, due to the grid-based approach to critical mode evaluation. The blue dot-dashed line denotes the stability limit for the inviscid dual-wave-mode SRI, as calculated in chapter 4. Each $+$ sign denotes the location of an example mode from the later figures within this chapter.

Region (α) has critical modes that are classical Taylor-Couette modes with $m = 0$, such as figure 6.2; region (β) corresponds to critical modes of the dual-wave-mode SRI, such as figures 6.3, 6.4 and 6.5; region (γ) corresponds to the wall-mode SRI, such as figure 6.6; region (δ) corresponds to the pseudo-radiative-mode SRI, such as figure 6.7; region (ϵ) corresponds to the wide-gap-mode SRI, such as figure 6.8.

In particular, a discontinuous change in structural appearance was found; this is the thin solid black line shown in the figure 6.1. Across this line, as one moved from region (β) to region (γ), the critical mode would discontinuously shift in terms of appearance, Reynolds number Re and $[m, k]$-wavenumbers. The point X denotes where this discontinuous change becomes continuous. This occurs because the critical modes of dual-wave-mode SRI and wall-mode SRI begin to overlap within the $[m, k, Re]$-parameter space, taking the form of the pseudo-radiative-mode. We refer to X as the point of continuity; it is discussed further in section 6.2.4.

6.1.1 Example figures

Figures 6.2 to 6.8 show examples of the appearance of critical modes from each region alongside wavenumber analyses. Later in this chapter, figure 6.12 shows an example for $N = 0.3$. Although we have not examined the $[\eta, \mu]$-parameter space for $N = 0.3$ in as much detail, figure 6.12 displays an example of the radiative instability (RI) as the critical mode. The radiative instability is discussed further in section 6.3.

Each figure examines specific values of η, μ, and N. The critical $[m, k]$-wavenumbers and critical Reynolds numbers Re_c are quoted in each figure. Each figure also declares whether the Lagrangian frequency goes to zero, i.e. $\Phi = 0$, anywhere within the flow, and if so declares the critical radial layer r_c where this happens. Also noted are radial locations where $\Phi(r) = \pm\sqrt{2\zeta\Omega}$, if they occur. The Lagrangian frequency is relevant to the dual-wave-mode mechanism described by Park and Billant [2013]; see appendix D.

Each figure features four subplots labelled (a)-(d):

Vertical (a) and horizontal (b) cross-sectional contour plots of the critical mode of instability are shown. For the vertical cross-section (a), radial and vertical velocities are shown as vectors, whereas the angular velocity perturbation is shown in colour contours with positive/negative represented by red/blue respectively. For the horizontal cross-section (b), radial and angular velocities are shown as vectors and the vertical velocity is shown in colour contours. Colour contours are scaled against the maximum radial velocity perturbation, and basic state flow is always in the positive θ-direction. Vertical cross-sections are taken at $\theta = 0$ whereas horizontal cross-sections are taken at $z = 0$. Each cross-section is taken over a sufficient range to demonstrate the full wavelength of each mode.

Lines of critical stability for various values of m are shown in plot (c), with stable flows towards the low-Reynolds-number region of the figure. The critical viscous mode is marked on these plots with x. Each line colour corresponds to the same values of m as in the inviscid plot (d). It should be noted that, although ranges of Re are explored, this is not non-linear analysis, and is simply examining whether or not specific combinations of parameters can be made linearly unstable.

Plot (d) depicts which combinations of $[m, k]$ were found to produce inviscid instabilities. We generally see a strong correlation between the bands of unstable inviscid wavenumbers compared to the sets of viscous wavenumbers that can be made unstable, however this is not always the case.

As noted in section 2.4.5, for any unstable mode with wavenumbers $[m, k]$, there are equally unstable counterpart modes for all combinations of $[\pm m, \pm k]$ for the same values of $[\eta, \mu, N, Re]$. We therefore only show the positive $[m, k]$ modes in figures 6.2 to 6.8, however we can expect the counterpart modes to activate at the same critical Reynolds number. This will produce a superposition of the relevant modes.

In most cases, only the range $m = [0, 1, 2, 3]$ is displayed. However, for figure 6.3 the relevant critical mode has $m = 7$, hence for that case we investigated the range $m = [0, 1, ..., 9]$.

Critical mode structure

It is worth considering how we would expect the eigenfunction of a perturbation mode to appear. Based upon the perturbation ansatz of equation (2.34) we expect a repeating cell-like structure in the θ- and z-directions. Due to the presence of the divergence free equation 2.39 in the system, we do not expect to see sinks or sources in the flow.

Figure 6.3(a)(b) displays an example SRI eigenfunction. (Note that figure 6.3 is a good demonstration of the fact that stratification can destabilise centrifugally stable flows, since in this case $\mu > \eta^2$.) All of the features we expected to see in the structure of a perturbation mode can be seen, providing a useful confirmation that our eigenfunction-solver code is well-behaved.

6.2 Discussion

We will first examine the cross-sections (a) and (b) of each example figure in following section 6.2.1. Plots (c) and (d) are then discussed in section 6.2.2, which compares the inviscid and viscous systems for all example figures.

6.2.1 Modal cross-section structure

Region (α) contains axisymmetric critical modes corresponding to the classical centrifugal instability of Taylor-Couette flow. An example mode is shown in figure 6.2. The vertical cross-section (a) exhibits strong azimuthal flow across the gap width, which correlates with a rotating cell-structure in the vertical plane. Centrifugal instabilities are slightly stabilised by the presence of stratification, increasing the critical Reynolds number compared to unstratified flow.

As previously described in section 4.1.1, we refer to the critical mode of region (β) as the dual-wave-mode SRI, since it corresponds to modes that have previously been investigated by Yavneh et al. [2001], Shalybkov and Rüdiger [2005] and Park and Billant [2013]. Examples of the mode are shown in figures 6.3, 6.4 and 6.5. Similar to the inviscid dual-wave-mode SRI seen in figure 4.2 from section 4.1.1, the viscous dual-wave-mode SRI has Kelvin waves propagating along each boundary wall. As before this is most visible in the horizontal cross-sections, which exhibit alternating regions of strong vertical flow

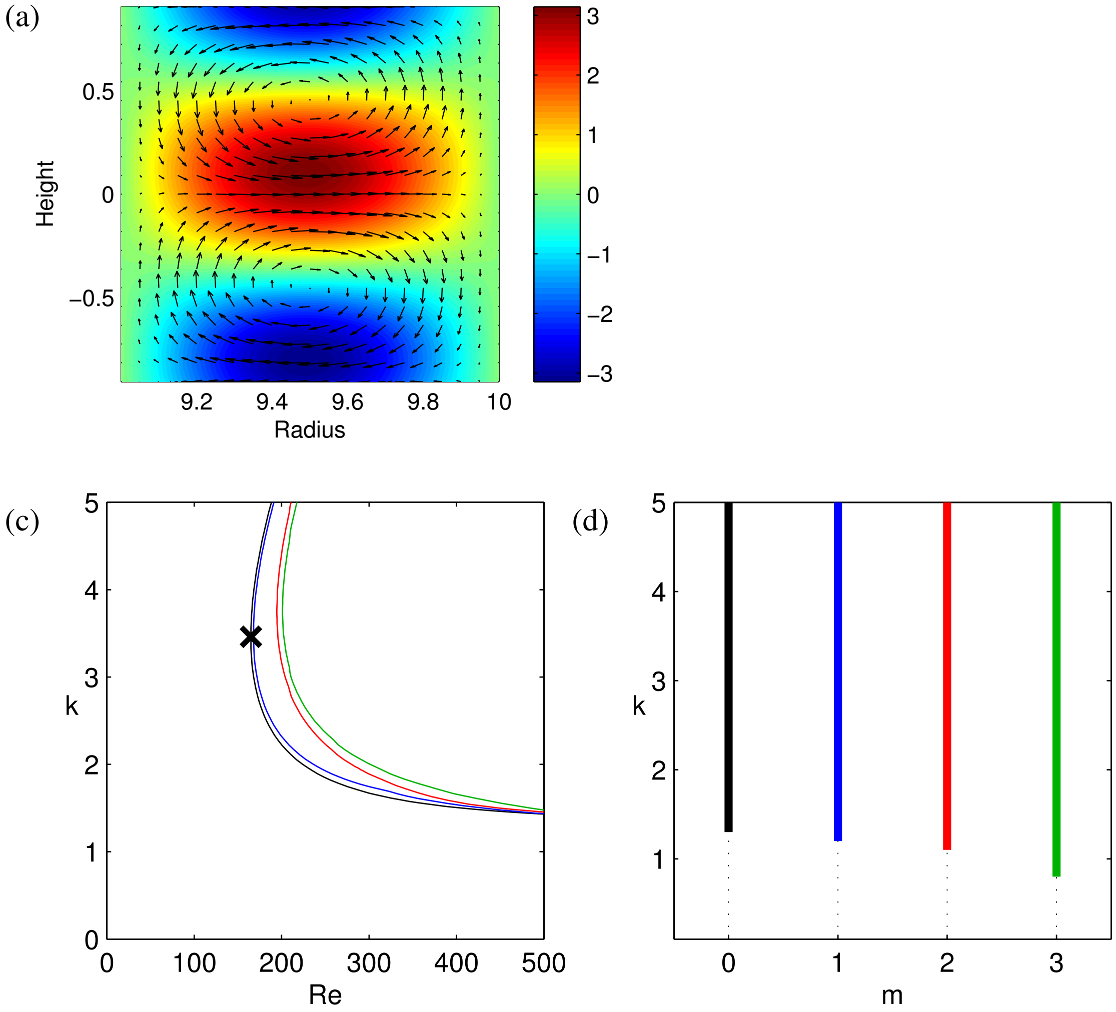

Figure 6.2: An example of classical axisymmetric Taylor-Couette instability, found as the critical mode within region (α) of figure 6.1. Here $\eta = 0.90$, $\mu = 0.40$, and $N = 1.0$. The critical mode of instability has $Re_c = 165$ with $m = 0, k = 3.46$, and $f = -0.421$. $\Phi(r_c) = 0$ does not occur for this range of r and this frequency, nor does $\Phi = \pm\sqrt{2\zeta\Omega}$. A horizontal cross-section is not shown in this context since the mode is axisymmetric, and hence there is no variation in the θ direction. The viscous and inviscid plots are labelled as (c) and (d) to preserve the convention of the other figures within this chapter.

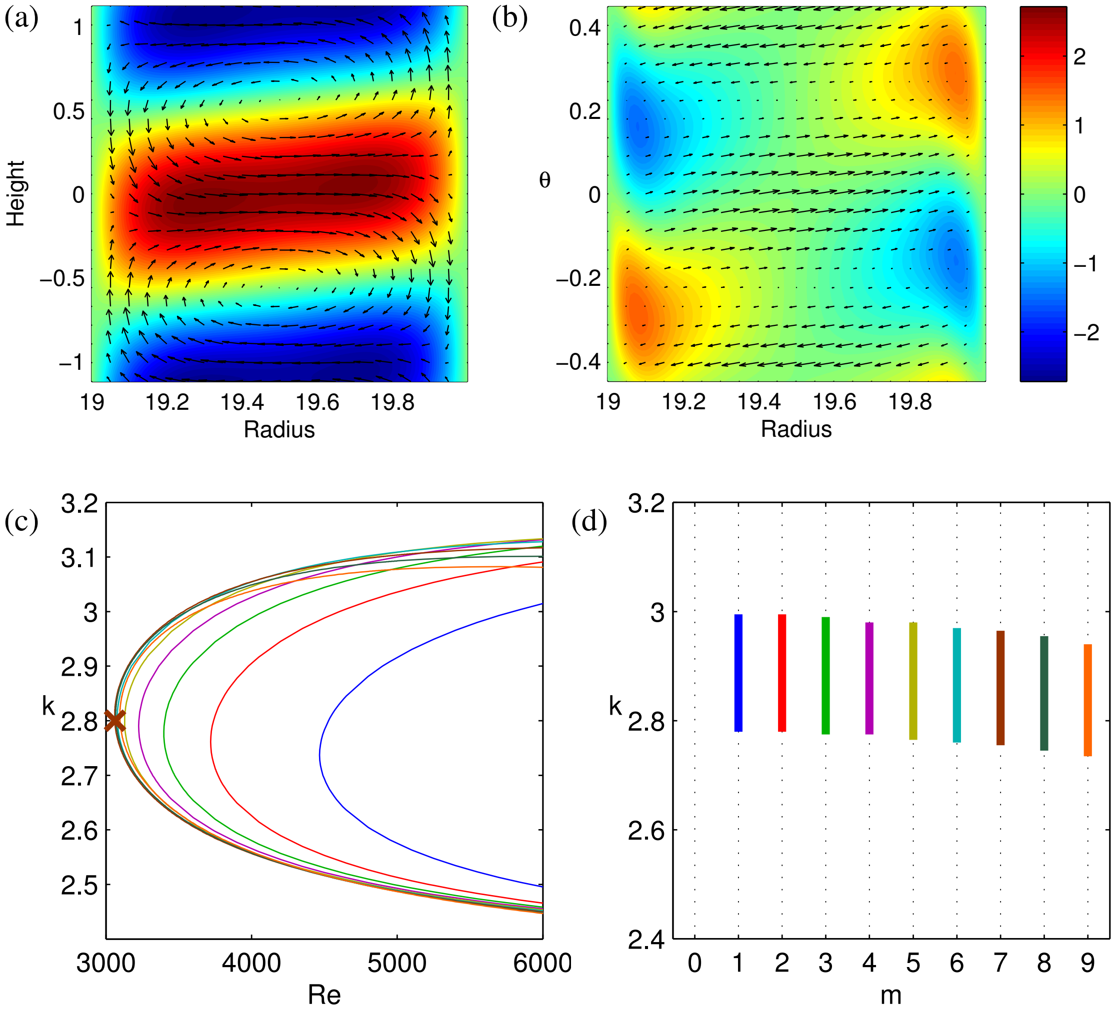

Figure 6.3: An example of dual-wave-mode SRI close to the Narrow Gap limit, found as the critical mode within region (β) of figure 6.1. Here $\eta = 0.95$, $\mu = 0.95$, and $N = 1.0$. The critical mode of instability has $Re_c = 3062$ with $m = 7, k = 2.80$, and $f = 6.82$. For this frequency, $\Phi(r_c) = 0$ occurs at $r_c = 19.5$, although $\Phi = \pm\sqrt{2\zeta\Omega}$ does not occur within the radial range.

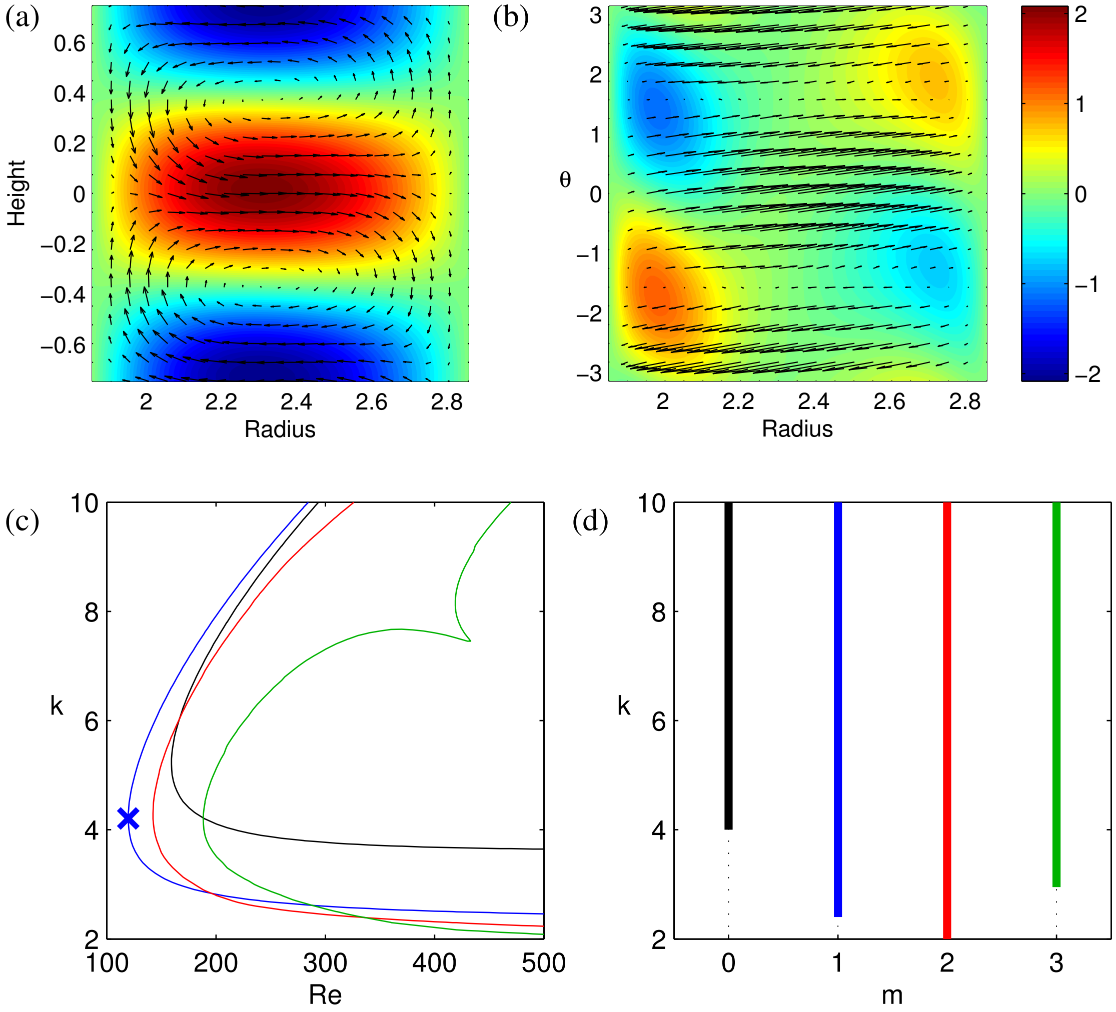

Figure 6.4: Another example of dual-wave-mode SRI, here for $\eta = 0.65$, $\mu = 0.25$ and $N = 1.0$, occupying region (β) of figure 6.1. The critical mode of instability has $Re_c = 120$ with $m = 1, k = 4.21$, and $f = 0.525$. For this frequency, $\Phi(r_c) = 0$ occurs at $r_c = 2.33$, although $\Phi = \pm\sqrt{2\zeta\Omega}$ does not occur since for this $[\eta, \mu]$ we have $2\zeta\Omega < 0$ throughout the radial range.

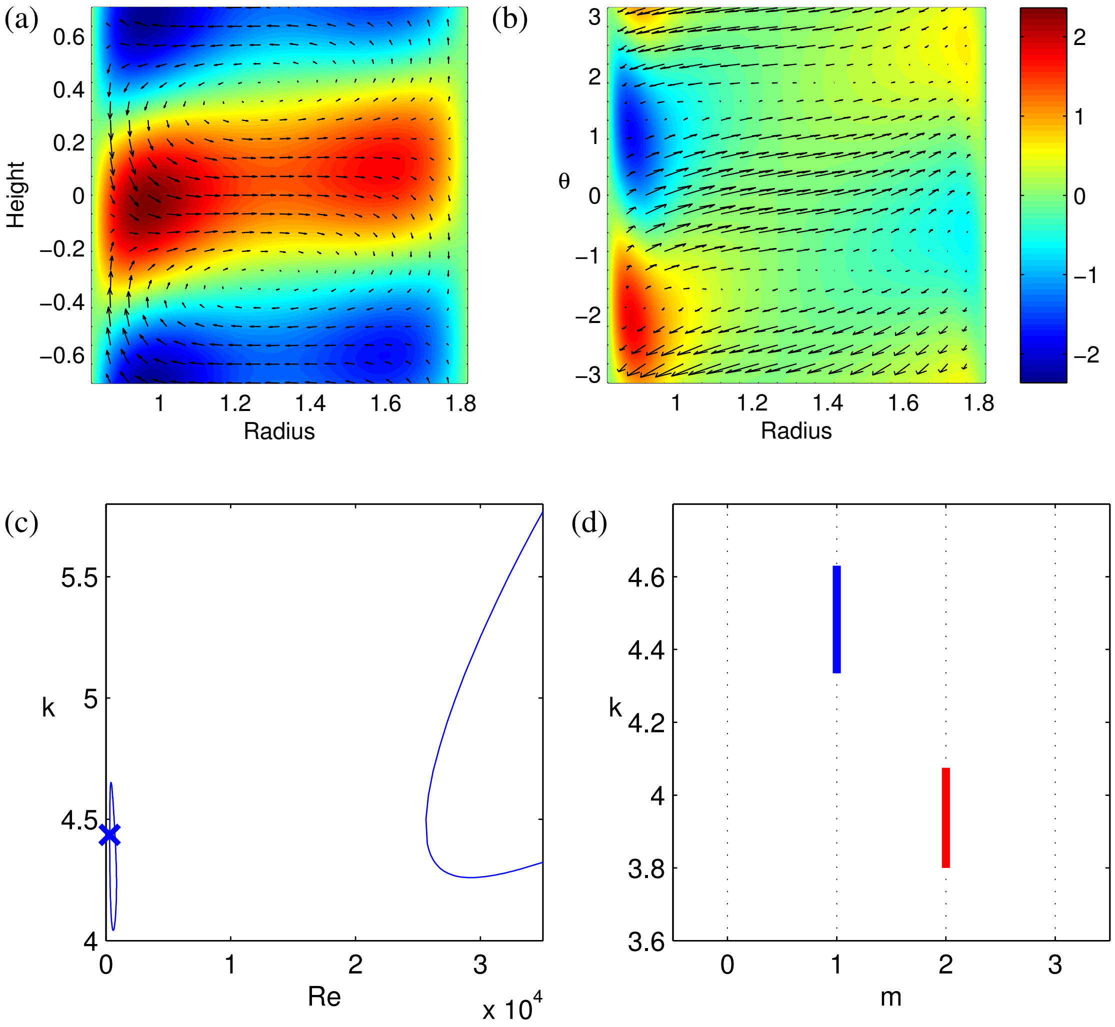

Figure 6.5: Another example of dual-wave-mode SRI, here for $\eta = 0.45$, $\mu = 0.45$ and $N = 1.0$, occupying region (β) of figure 6.1, close to the dividing line with region (γ). The critical mode of instability has $Re_c = 304.1$ with $m = 1, k = 4.436$, and $f = 0.595$. For this frequency, $\Phi(r_c) = 0$ occurs at $r_c = 1.27$, although $\Phi = \pm\sqrt{2\zeta\Omega}$ does not occur within the radial range. There is a closed domain loop in the bottom left corner of (c), which is shown in more detail in figure 6.9(c). This closed loop contains the critical mode of instability, but there is also a separate domain of instability visible for higher Reynolds numbers, which appears to be unbounded.

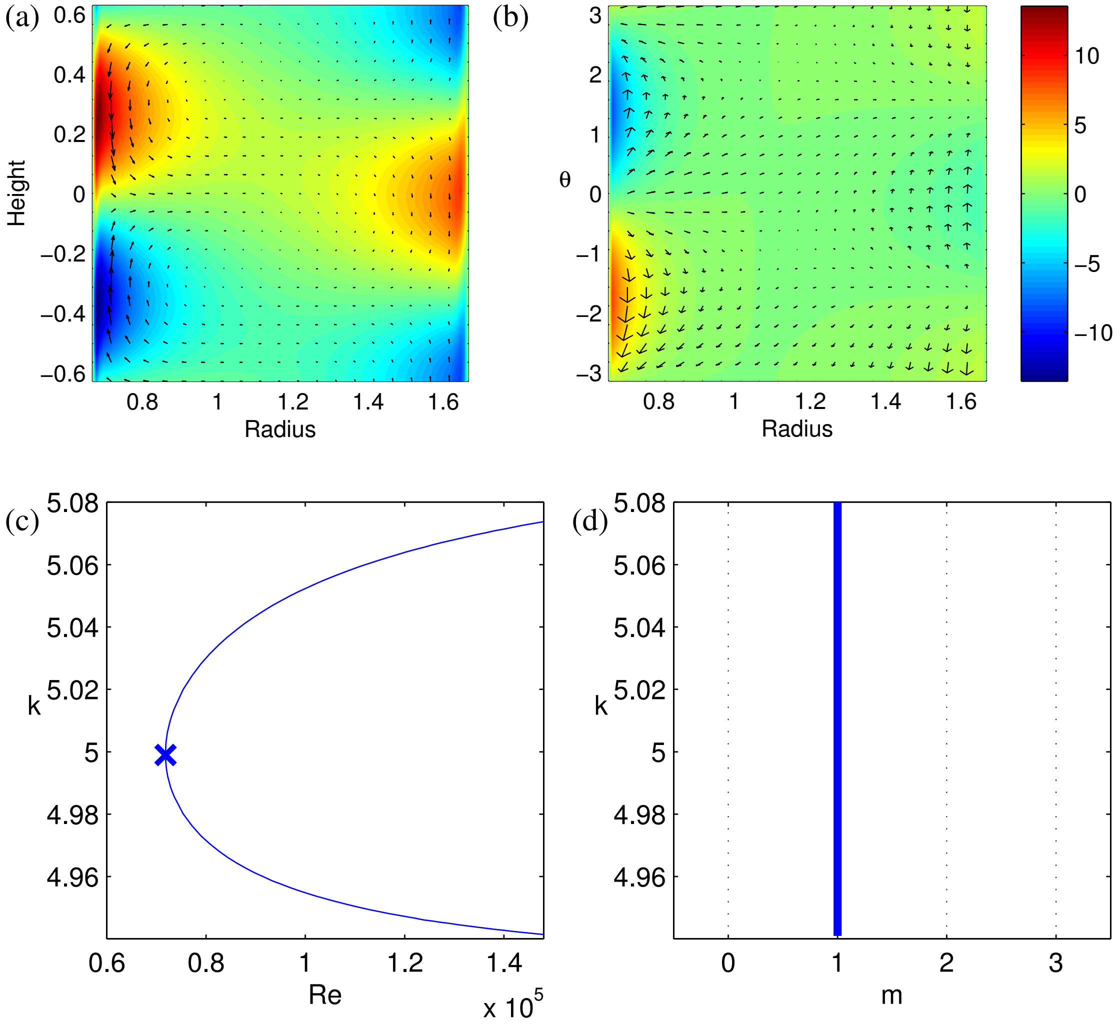

Figure 6.6: An example of wall-mode SRI, found as the critical mode within region (γ) of figure 6.1. Here $\eta = 0.40, \mu = 0.45$ and $N = 1.0$. The critical mode of instability has $Re_c = 71840$ with $m = 1, k = 5.00$, and $f = 0.598$. For this frequency, $\Phi(r_c) = 0$ occurs at $r_c = 1.07$, although $\Phi = \pm\sqrt{2\zeta\Omega}$ does not occur within the radial range.

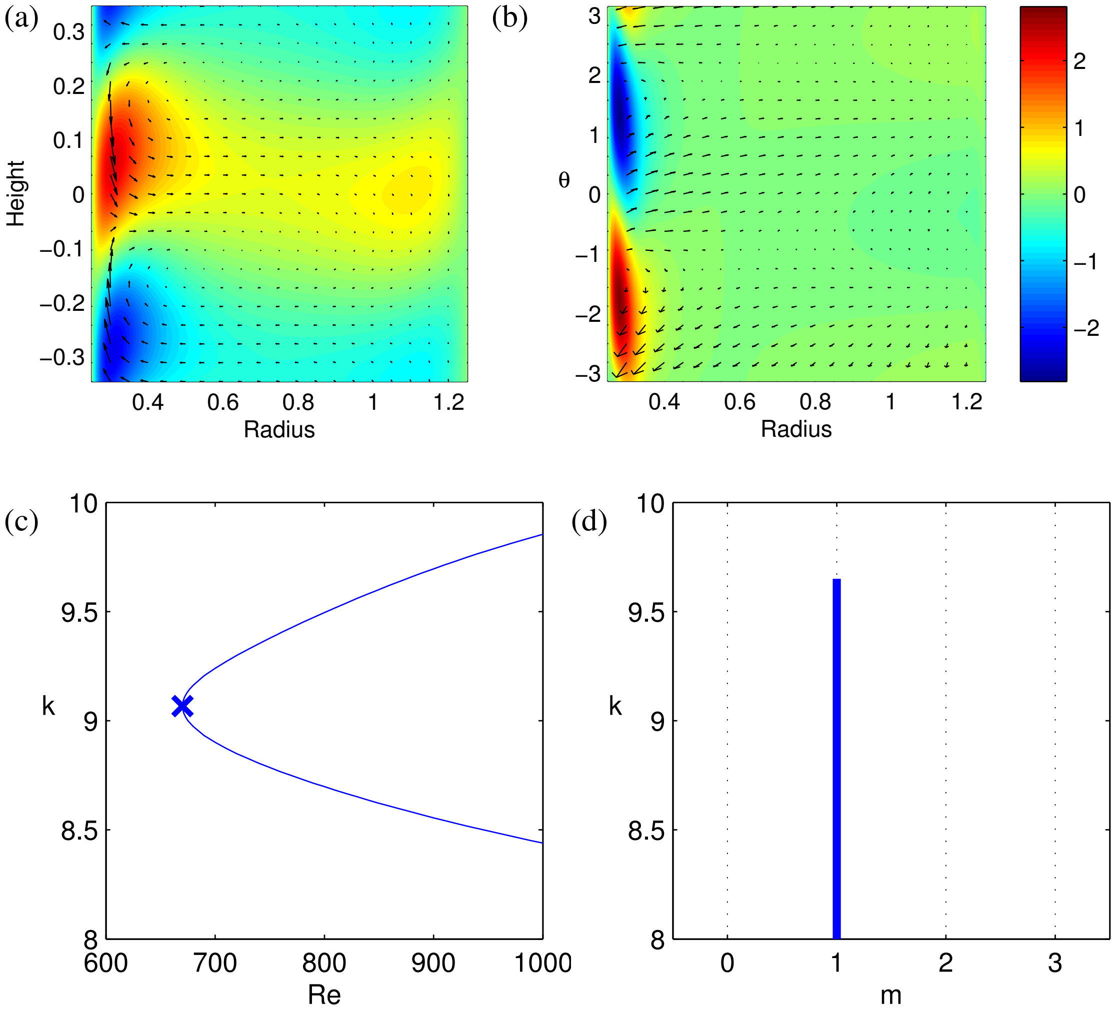

Figure 6.7: An example of the pseudo-radiative-mode SRI, found as the critical mode within region (δ) of figure 6.1. Here $\eta = 0.20, \mu = 0.10$ and $N = 1.0$. The critical mode of instability has $Re_c = 671$ with $m = 1, k = 9.07$, and $f = 0.238$. For this frequency, $\Phi(r_c) = 0$ occurs at $r_c = 0.577$ and $\Phi(r_-) = -\sqrt{2\zeta\Omega}$ occurs at $r_- = 0.319$. $\Phi = +\sqrt{2\zeta\Omega}$ does not occur within the radial range.

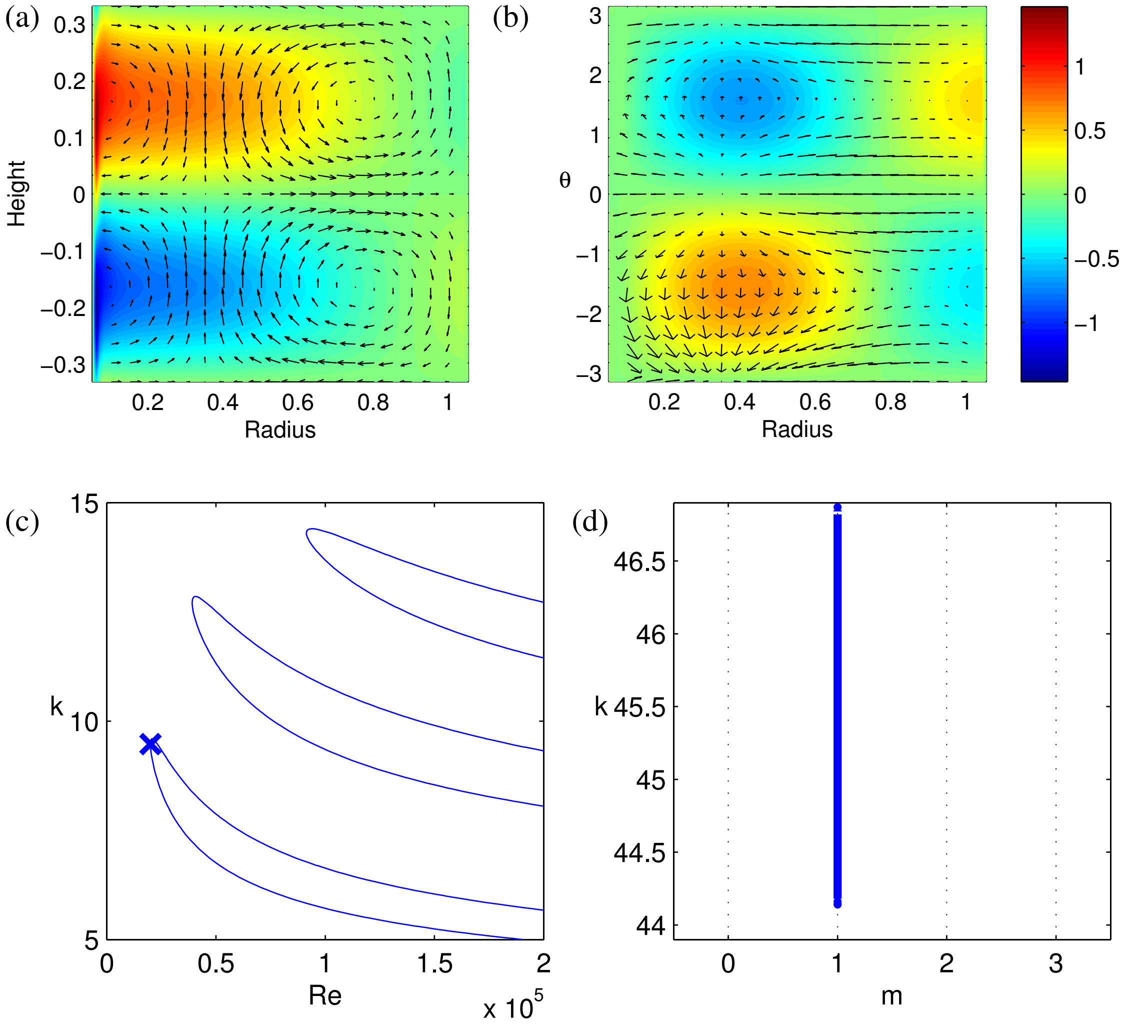

Figure 6.8: An example of the wide-gap-mode SRI, found as the critical mode within region (ϵ) of figure 6.1. Here $\eta = 0.05, \mu = 0.05$ and $N = 1.0$. The critical mode of instability has $Re_c = 20007$ with $m = 1, k = 9.477$, and $f = 0.538$. For this frequency, $\Phi(r_c) = 0$ occurs at $r_c = 0.0734$, $\Phi(r_-) = -\sqrt{2\zeta\Omega}$ occurs at $r_- = 0.0536$, and $\Phi(r_+) = +\sqrt{2\zeta\Omega}$ occurs at $r_+ = 0.102$. Note that the range of inviscidly unstable wavenumbers appears to be entirely distinct from the range of viscously unstable wavenumbers.

adjacent to each boundary. However, unlike the inviscid dual-wave-mode SRI, the viscous dual-wave-mode SRI displays a strong azimuthal flow across the gap width, similar to the classical viscous Taylor-Couette instability. For $N = 1.0$ the dual-wave-mode SRI typically has a critical Reynolds number in the range $100 < Re_c < 400$, although this increases near the narrow-gap limit.

In the case of figure 6.3, we can see that the lines of critical stability corresponding to the various values of m are all very close together - this is a phenomenon that occurs close to the narrow gap limit, with the critical horizontal wavenumber m_c climbing to higher and higher values.

Figure 6.5 shows an example of dual-wave-mode SRI close to the line of discontinuity between regions (β) and (γ); it can be seen that the azimuthal flow has reduced in strength at the centre of the gap width, and gathered slightly towards the inner radius. It can also be seen in the horizontal cross-section that the outer boundary Kelvin Wave has become significantly weaker in amplitude compared to the wave at the inner boundary.

We refer to the critical mode of region (γ) as the wall-mode SRI, since the velocity perturbations are strongest close to the boundary walls, and there is little activity in the middle of the gap width. A typical wall-mode SRI eigenfunction is shown in figure 6.6. It can also be seen that the vertical velocity perturbation is significantly stronger at the inner boundary compared to the outer boundary. For $N = 1.0$ the wall-mode SRI typically has a critical Reynolds number of $Re_c > 10,000$, considerably larger than the Re_c for a typical dual-wave-mode SRI.

We refer to the critical mode of region (δ) as the pseudo-radiative-mode SRI, since it exhibits a strong similarity to the Radiative Instability first discussed by Le Dizès and Riedinger [2010]; this is discussed further in section 6.3.2. Interestingly, region (δ) is continuously connected to regions (β) and (γ), despite the two other regions being discontinuously separated from each other. The viscous $[m, k, Re]$-parameter space of region (δ) appears to correspond to an overlap of the corresponding $[m, k, Re]$-parameter spaces from (β) and (γ); see section 6.2.4. For $N = 1.0$ the pseudo-radiative-mode SRI typically has a critical Reynolds number in the range $300 < Re_c < 2000$, although it climbs to significantly higher values as regions (γ) and (ϵ) are approached.

When approaching region (ϵ) from region (δ), there is another discontinuous change in the form and vertical wavenumber of the critical mode, although Re_c remains continuous. This is represented by the dashed line separating the two regions in figure 6.1. Region (ϵ) exhibits a high-Reynolds number stratified-rotational instability as the critical mode, and we refer to this mode as the wide-gap-mode SRI. The wide-gap-mode is shown in figure 6.8; particularly striking are the strong vertical flows occupying most of the gap. For $N = 1.0$ the wide-gap-mode SRI typically has a critical Reynolds number of $Re_c > 10,000$, which is considerably larger than the Re_c of a typical dual-wave-mode SRI.

Although both require high Reynolds numbers, it is not clear if the wide-gap-mode SRI of region (ϵ) is related to the wall-mode SRI of region (γ).

6.2.2 The Viscous and Inviscid systems

By examining the wavenumber analyses (c) and (d) of figures 6.2 through to 6.8, we can compare and contrast which wavenumbers are unstable in the viscous and inviscid domains.

We expect to see strong correlation between the inviscid and viscous systems, as the inviscid system can be considered to be the high-Re limit of the viscous system, albeit without the presence of non-slip boundary conditions. Working with the assumption that increasing Re promotes instability, any unstable point in the viscous domain can be expected to remain unstable as Re increases up to the inviscid limit. This expectation holds up for figure 6.2, with the classical axisymmetric Taylor-Couette instability in region (α). We can see in (c) that the various m-modes are very close together in the $[m, k, Re]$-parameter space, which will not typically be the case for later SRI modes. In (d) we can see an exceptionally strong correlation between the unstable $[m, k]$-wavenumbers of inviscid flow when compared to the viscous $[m, k]$-wavenumbers that could be made unstable.

However, this expectation of a strong correlation between the inviscid and viscous systems is challenged by figure 6.3, for a narrow gap dual-wave-mode of the SRI in region (δ). While we do see a correlation between the range of unstable k for the viscous (c) and inviscid (d) systems at all values of m, the viscous system has a consistently wider range of k that can be made unstable than the inviscid system. The discrepancy is notable but is also relatively minor. However, in later examples we will see that there is even stronger disagreement between the bands of unstable viscous and inviscid instability.

We do see stronger correlations between the viscous and inviscid systems in figure 6.4, a dual-wave-mode SRI result from region (β); figure 6.6, a wall-mode SRI result from region (γ); and figure 6.7, a pseudo-radiative-mode SRI result from region (δ).

However, figure 6.5, a dual-wave-mode SRI result of region (β), again shows only a weak correlation between the viscous and inviscid wavenumbers. Figure 6.5(c) also demonstrates the existence of a closed domain loop. Closed domain loops are discussed further in section 6.2.3, although their existence conclusively proves that increasing the Reynolds number does not always promote instability for the SRI, compared to the expectation we stated above. Figure 6.5 also has an inviscidly unstable range of k for $m = 2$, but no visible line of critical stability for the viscous system. This may indicate that for the viscous system to become unstable at those wavenumbers it requires higher values of Re. Alternatively it may indicate instabilities that are only possible in the inviscid system and are not compatible with either viscosity or viscous boundary conditions.

Finally figure 6.8, a wide-gap-mode SRI result from region (ϵ), demonstrates a complete lack of correlation between the unstable wavenumbers of the viscous and inviscid systems. This mode also exhibits distinct bands of viscous instability within the $[m, k, Re]$-parameter space.

Dual-Wave-mode SRI

We can see from figure 6.1 that the viscous dual-wave-mode of region (β) extends beyond the stability line of the inviscid dual-wave-mode SRI derived in chapter 4. This may be a result of viscosity aiding the mode, allowing it to persist further into the $[\eta, \mu]$-parameter space. The influence of viscosity on the dual-wave-mode SRI would match with the observation that modes in region (β) are found within closed domain loops as one approaches the discontinuity line separating regions (β) and (γ), as closed domain loops are examples where some viscosity is necessary for the instability.

At the very wide gap, $\eta < 0.35$, the limit of the viscous dual-wave-mode is seemingly stricter than the inviscid dual-wave-mode stability limit. It would appear that viscosity has in this case stabilised the dual-wave-mode SRI.

The Lagrangian Frequency

In all plots demonstrating the non-axisymmetric SRI modes, then $\Phi(r)$ changes sign as one moves across the radial range, transitioning at a point where $\Phi(r_c) = 0$. This point has been noted in the caption of each figure. This transition between positive and negative Φ is predicted for the dual-wave-mode SRI by Park and Billant [2013]; see appendix D. The different signs of the Lagrangian frequency represent how the wave-like regions travel in opposite directions relative to the basic state flow, despite travelling together in the lab frame.

Park and Billant [2013] also predicted that there would be radial layers where the Lagrangian frequency $\Phi(r_{\pm}) = \pm\sqrt{2\zeta\Omega}$. However, these layers are not seen in any of the viscous dual-wave-modes that we have examined, although r_{-} occurs in figure 6.7, and both radial layers are seen in figure 6.8.

In the inviscid system, the radial layers $r_{\pm}$ represent the edges of the wave-like regions of the dual-wave-mode SRI. Given that the layers are absent for the viscous dual-wave-mode SRI, but the wave-like regions are still present, it would appear that viscosity has altered the necessary conditions for these wave-like regions. This may explain why the domain of dual-wave-mode SRI is extended somewhat in the presence of viscosity for the same value of N.

6.2.3 Closed Domain Loops

Figure 6.9 shows examples of several closed domain loops. These are closed unstable regions of the $[m, k, Re]$-parameter space for fixed values of $[\eta, \mu, N]$; here the flow can be made linearly unstable for only a finite range of Re. In these regions, it appears that viscosity is somehow necessary for the instability to occur, as reducing the influence of

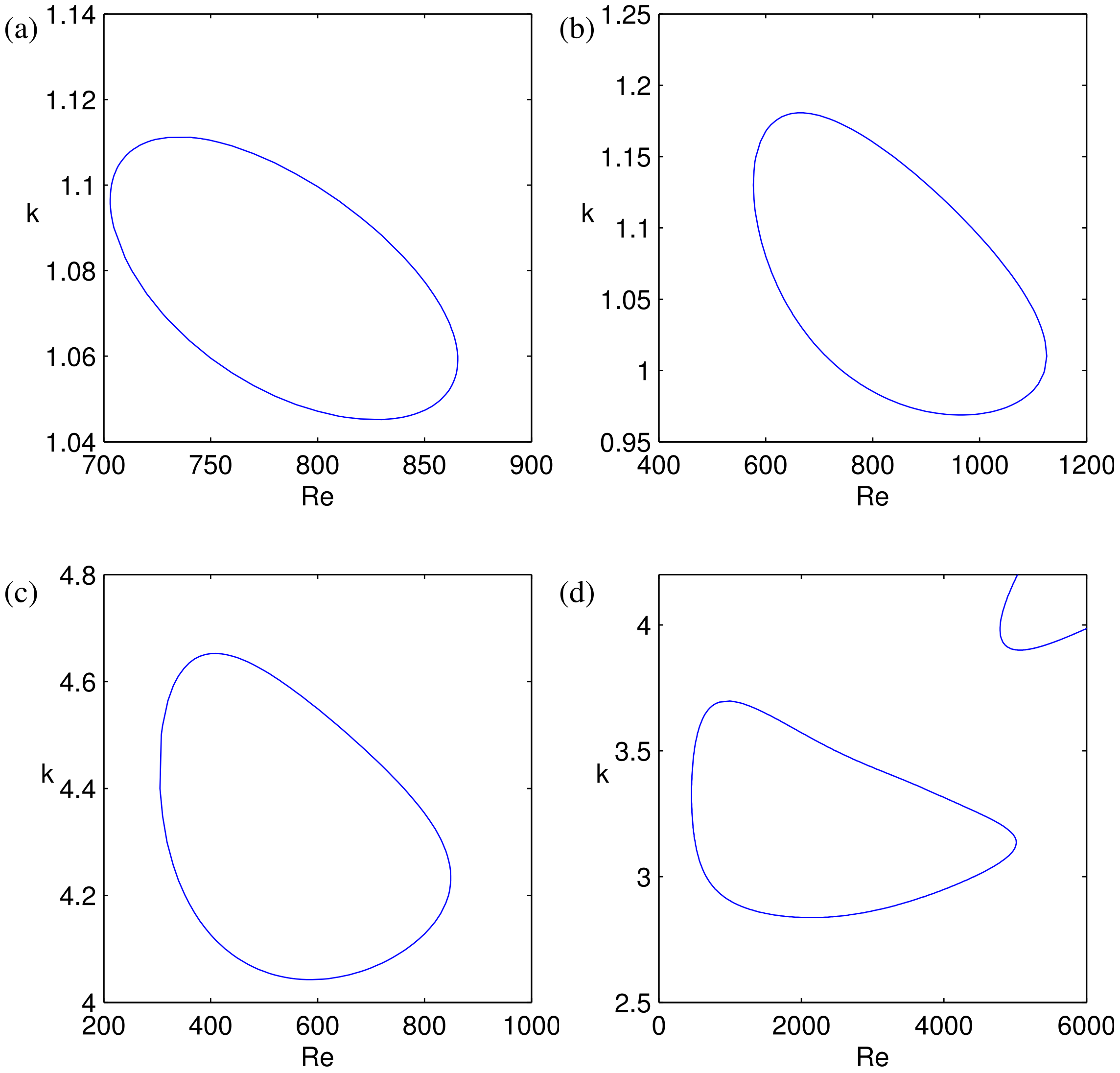

Figure 6.9: Examples of closed domain loops. For flow parameters within these loops, the flow is linearly unstable, whereas it is stable outside. These therefore provide examples where increasing the Reynolds number can stabilise the flow. (a) $\eta = 0.56, \mu = 0.50$ and $N = 0.3$. (b) $\eta = 0.57, \mu = 0.50$ and $N = 0.3$. (c) $\eta = 0.45, \mu = 0.45$ and $N = 1.0$. (d) $\eta = 0.70, \mu = 0.70$ and $N = 1.0$. In all examples we have $m = 1$.

viscosity (by increasing Re) can entirely remove the linear instability for all wavenumbers. This suggestion is supported by the fact that these closed domain loops typically do not appear to have any correspondence to instabilities in the inviscid domain.

There is a precedent for viscosity being required for shear flow instabilities. For example, Plane Poiseuille flow can be stable in the inviscid domain, but unstable when the viscosity is non-zero [Drazin and Reid, 1981]. Recently Ibanez et al. [2016] performed experiments which showed a similar phenomenon where higher Reynolds numbers could stabilise the flow compared to an unstable result with a lower Reynolds number with all other parameters kept the same; see section 5.3.

For $N = 1.0$, closed domain loops were only ever found close to the discontinuity line between regions (β) and (γ) on figure 6.1. However it should also be noted that closed domain loops present something of a challenge for numerical methods, as they are easily missed without a rigorous and time-consuming scan of the entire $[m, k, Re]$-parameter space. In general in this chapter we have only found closed domain loops by utilising guesses from nearby regions of the $[\eta, \mu, N]$-parameter space.

In each case where we have observed closed domain loops, the instability does appear to ultimately switch on again as Re is further increased. Figure 6.5(c) provides a good example of this; a separate domain of instability can be seen at higher Reynolds numbers. The structure of unstable eigenmodes found within the high-Re domain of instability are very similar to the critical eigenmode shown in figure 6.6. This suggests that the unbounded domains of figures 6.5(c) and 6.6(c) are connected, and that the closed domain loop vanishes as η is reduced from 0.45 to 0.40 (with $\mu = 0.45$ and $N = 1.0$).

We have evidence that closed domain loops can quickly shrink within the $[m, k, Re]$-parameter as η and μ are changed. Consider figures 6.9(a) and (b), which show roughly the same closed domain loop for slightly different values of η, with $\mu = 0.5$ and $N = 0.3$. As can be seen, the loop at $\eta = 0.56$ is significantly smaller, with a Reynolds number range of $700 < Re < 875$ rather than the range $600 < Re < 1175$ of $\eta = 0.57$. Upon further reducing η, the closed domain loop appears to shrink and ultimately vanish entirely.

Since the critical mode in figure 6.5 is contained within a closed domain loop, which vanishes as η is decreased or μ is increased, the critical mode must change sharply once the closed domain loop ceases to exist. This would explain the discontinuity line between regions (β) and (γ), with the related change in critical mode appearance and significant increase in critical Reynolds number. The shift is particularly apparent when considering the fact that figures 6.5 and 6.6 differ in $[\eta, \mu]$-parameter space by only $\eta = 0.45$ compared to $\eta = 0.4$. It would therefore appear that closed domain loops are the mechanism behind the discontinuity line on figure 6.1.

A related phenomenon to these closed domain loops is seen in figure 6 of Rüdiger et al. [2017]. This figure, derived using a computational solver similar to our own, sees a closed-domain loop in the $[Re, Rn]$-parameter space for $\eta = 0.52$ and $m = 1$. Here $Rn = \hat{N}\hat{r}_{\text{in}}\hat{\lambda}/\hat{\nu}$ is a stratification Reynolds number. This closed domain loop vanishes at around $\mu \simeq 0.571$, which is similar to our result of seeing the corresponding $[m, k, Re]$-parameter space closed domain loop vanishing at $\mu \approx 0.55$ for $\eta = 0.52$, $N = 1.0$ and $m = 1$.

6.2.4 The Point of Continuity

The thin black line on figure 6.1 denotes the discontinuous jump in Re_c between regions (β) and (γ) as the critical mode changes from the dual-wave-mode SRI to the wall-mode SRI. In the previous section, we have explained how this jump is related to the vanishing of closed domain loops.

As region (δ) is approached along this line of discontinuity, the discontinuous jump becomes steadily smaller, until the change in Re_c becomes continuous at the point X. This point of continuity appears to be at approximately $[\eta = 0.2, \mu = 0.1]$ for $N = 1.0$. In figure 6.10, we can see how the discontinuity between the dual-wave-mode SRI and the wall-mode SRI becomes continuous.

The point of continuity appears to be a result of an overlap of the relevant domains in the viscous $[m, k, Re]$-parameter space between the dual-wave-mode SRI and the wall-mode SRI. The unbounded domain of instability for higher Reynolds numbers, corresponding to the wall-mode SRI, moves down to lower Reynolds numbers as one approaches point

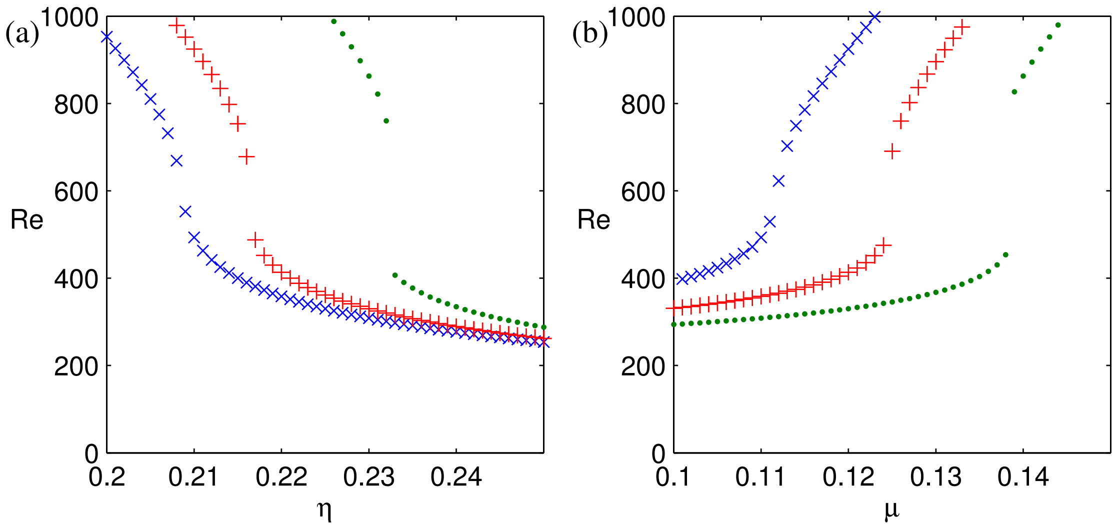

Figure 6.10: Tracking the discontinuity in Re_c near to the co-dimension 2-point. Each plot shows the critical Reynolds number Re_c for instability for a range of η and μ values. In both plots we have $N = 1.0$. We can see that the system transitions from continuous to discontinuous as η and μ are increased. In (a), we have $0.2 < \eta < 0.25$. Blue crosses give the results for $\mu = 0.11$, red pluses give the results for $\mu = 0.12$, and green dots give the results for $\mu = 0.14$. In (b), we have $0.1 < \mu < 0.15$. Blue crosses give the results for $\eta = 0.21$, red pluses give the results for $\eta = 0.22$, and green dots give the results for $\eta = 0.23$.

X from higher values of η or μ. This ultimately means that the closed domain loop, corresponding to dual-wave-mode SRI, is engulfed by the unbounded domain before it can vanish. A snapshot of this process is shown in figure 6.11(a).

6.2.5 Wide-gap transition

The transition between regions (δ) and (ϵ) does not rely upon closed domain loops, although the transition is also visible in the $[m, k, Re]$-parameter space. Instead, as the transition is approached, the pseudo-radiative-mode SRI of region (δ) requires increasingly high critical Reynolds numbers. At the same time, the $[m, k, Re]$-domain of the wide-gap-mode SRI becomes more unstable, requiring smaller Reynolds numbers. The two instabilities operate at different bands of vertical wavenumbers, and as the transition between the two regions is crossed, the wide-gap-mode SRI becomes more unstable than the overlap-mode SRI. The transition between regions (δ) and (ϵ) can therefore be considered a line of codimension-2.

This transition can be seen in figure 6.11(b), which shows an example where the two

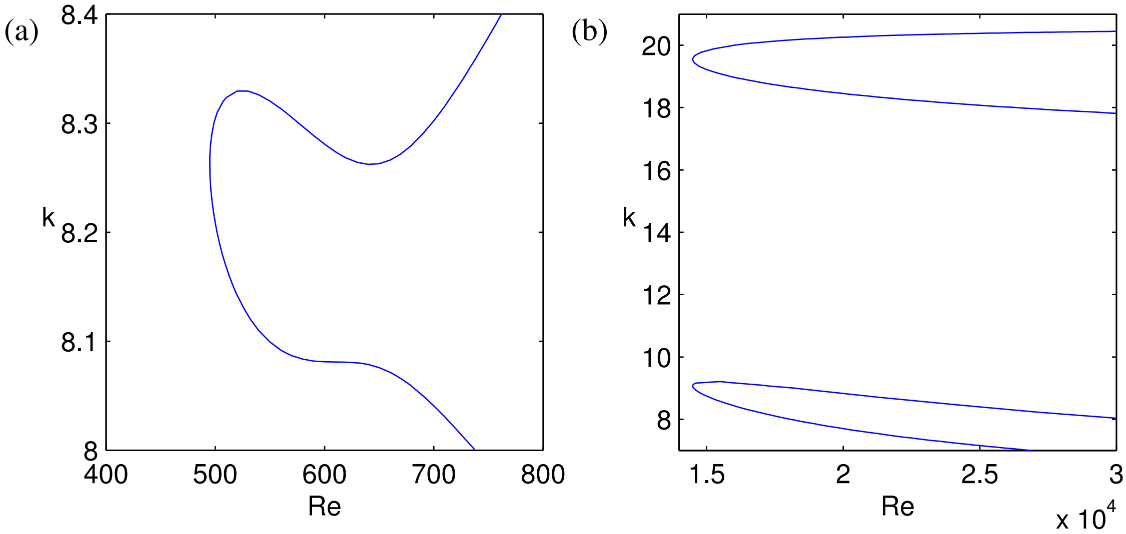

Figure 6.11: (a) A plot of the $[m, k, Re]$-parameter space for $\eta = 0.22, \mu = 0.1245$, and $N = 1.0$, near the point of continuity X. It can be seen that the closed domain loop of region (β) has merged with the unbounded high-Re domain of region (γ). (b) A plot of the $[m, k, Re]$-parameter space for $\eta = 0.0786, \mu = 0.05$, and $N = 1.0$, at the transition between region (δ) and region (ϵ).

instabilities require approximately equal Reynolds numbers to become unstable. In this figure, the wide-gap-mode SRI corresponds to the unstable region around $k = 9$, whereas the pseudo-radiative-mode SRI corresponds to the unstable region around $k = 20$.

6.3 Radiative Instability

The Radiative Instability (RI) is a form of stratified non-axisymmetric instability first identified by Le Dizès and Riedinger [2010] in the inviscid domain for the wide-gap limit of stratified Taylor-Couette flows. It is characterised by the presence of perturbation wave travelling around the inner cylinder of the flow, with amplitudes rapidly shrinking as the radius is increased. In Le Dizès and Riedinger [2010] the RI was only found when the outer cylinder had been moved to infinity, replacing the outer boundary condition with a condition of outward radiation.

Experimental confirmation of the RI was provided by Riedinger et al. [2011], see section 5.2 for further details. By physical constraints, this experiment had a wide but non-infinite gap. However, from the edge of the inner cylinder to the edge of the tank, the smallest gap width of the experiment would still have been 17.5 times the radius of the largest cylinder

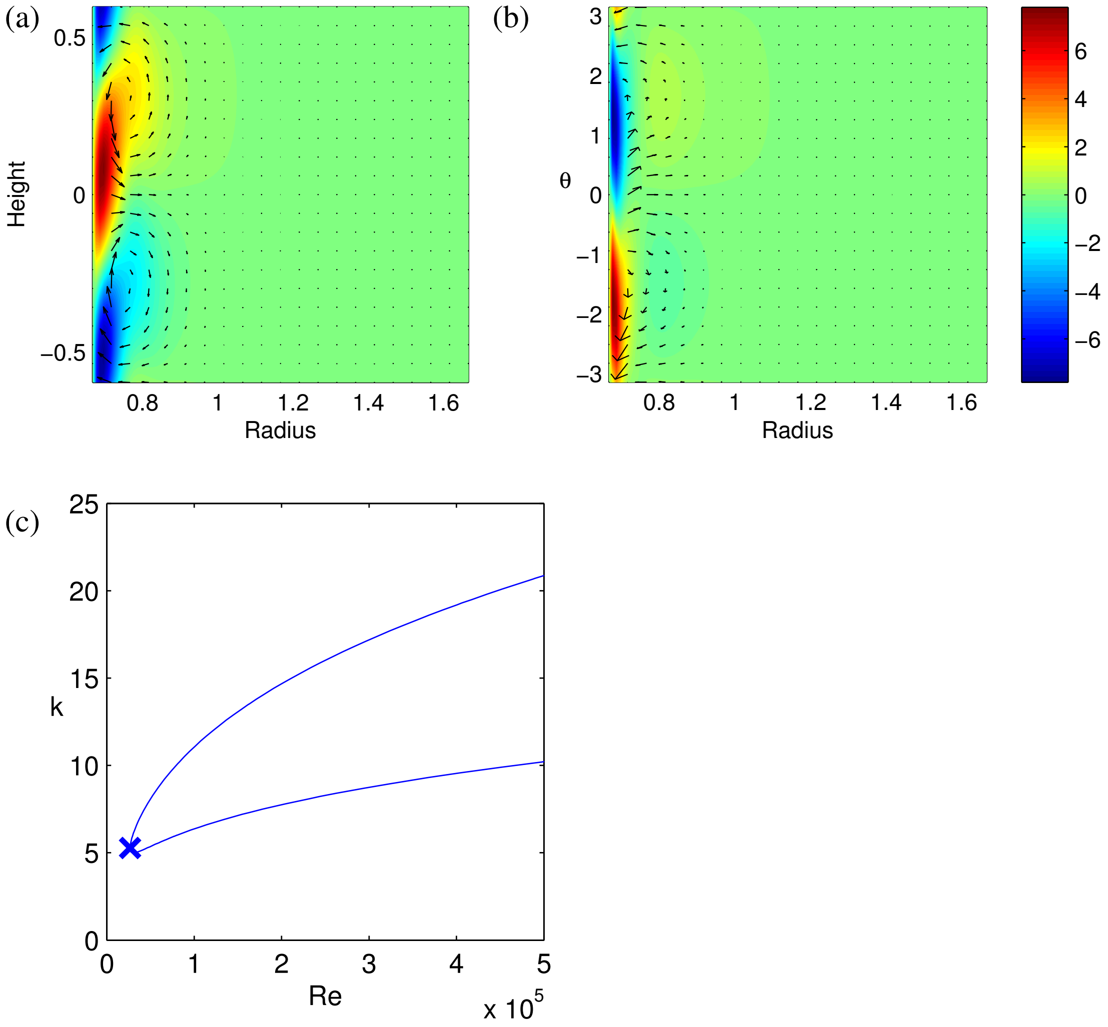

Figure 6.12: An example of the radiative instability as the critical mode of instability for stratified Taylor-Couette flow. Here $\eta = 0.40, \mu = 0.40$ and $N = 0.3$. The critical mode of instability has $Re_c = 26603$ with $m = 1, k = 5.270$, and $f = 0.850$. Since this is a result for $N = 0.3$, this mode is not marked upon figure 6.1. For this frequency, $\Phi(r_c) = 0$ occurs at $r_c = 0.750$, although $\Phi = \pm\sqrt{2\zeta\Omega}$ does not occur within the radial range. We do have $\Phi^2(r_N) = N^2$ within the radial range at $r_N = 1.10$. No inviscid modes were found for this combination of η, μ and N.

used. This would correspond to a maximum radius ratio of $\eta = 0.057$; note that the tank was rectangular and the gap width will generally have been even larger.

The RI was detected in numerical viscous simulations by Leclercq et al. [2016] for non-wide-gap flows with $\eta = 0.417$. It was found for linear perturbations in the super-critical domain, i.e. beyond the onset of instability. This confirmed that the RI could exist away from the wide-gap limit, although it remained unclear whether the RI could exist as a critical mode of instability for viscous flows.

6.3.1 Appearance

As stated above, the RI is characterised by a single unstable mode travelling around the inner boundary, with perturbations decaying in amplitude as the radius is increased. If an outer boundary is present, the perturbation flow adjacent to the outer boundary should be negligible.

Leclercq et al. [2016] also identified a critical radial layer in the flow where $\Phi^2(r) = N^2$, and suggested that the presence of this layer might be what enabled the RI to exist away from the wide-gap limit.

6.3.2 The Radiative Instability in the present work

The modes of instability in region (δ), such as figure 6.7, resemble the RI. They have a strong perturbation wave adjacent to the inner cylinder, and the flow is significantly weaker at all larger radii. However, there is still some azimuthal flow at larger radii, as evidenced by the colour contours on figure 6.7(a). The $\Phi^2 = N^2$ radial layer is also absent in the flow at the frequency for the pseudo-radiative-mode SRI. Given that region (δ) is close to the wide gap limit, it is plausible that the pseudo-radiative-mode continuously shifts to become the RI as η is further reduced. This would match well with inviscid arguments made by Le Dizès and Riedinger [2010].

In figure 6.12, we show the critical mode of instability for a flow with stratification $N = 0.3$, found in the region of figure 4.4(a) which had no inviscid instabilities. This critical mode shows all the features of the RI. The perturbation flow is focused on the inner boundary, with negligible perturbations as the radius is increased. Furthermore, the $\Phi(r) = -N$ radial layer is present in the flow, as marked on the figure. We take this mode as a demonstration that the radiative instability can sometimes be the critical mode of instability for stratified viscous Taylor-Couette flows.

This example of the RI was observed within the region of the parameter space where no inviscid modes of instability have been found, previously seen in figure 4.4(a). It is interesting to note that the $\Phi^2 = N^2$ radial layer appears to have prevented the presence of inviscid instabilities in this region, and yet simultaneously allowed the viscous RI to exist away from the wide-gap limit. This again suggests that the presence of viscosity is capable of extending the effective range of stratified instabilities compared to inviscid flows.

6.3.3 Astrophysical context for the RI

The radiative instability is particularly interesting in the context of astrophysical disc flows, since it depends on only the inner boundary, with the outer boundary going to infinity. Astrophysical discs are expected to have an inner boundary condition, related to either an inner hole, or related to flow onto a central object. The radiative instability may therefore be a stratified non-axisymmetric instability which is relevant to astrophysical discs in a way that dual-wave-mode SRI, which depends on two boundary conditions, is not. We therefore suggest for future work that the RI be examined in more detail.

Chapter 7

The Narrow Gap Limit of the SRI

7.1 Threshold of Non-Axisymmetric Critical modes

We have defined the critical mode of instability in section 2.4.6. Depending on the specific values of $[\eta, \mu, N]$, the critical mode can be either axisymmetric with $m = 0$ or non-axisymmetric with $m \neq 0$. In this chapter, we are interested in the threshold between these two cases.

For the sake of distinction, we label the axisymmetric critical Reynolds number as $Re_{m=0}$ and the non-axisymmetric critical Reynolds number as $Re_{m\neq0}$. $Re_{m=0}$ and $Re_{m\neq0}$ can both be found using the methods discussed in section 3.5.1. We further define the quantity $\Delta_{Re} = Re_{m\neq0} - Re_{m=0}$. Whether Δ_{Re} is positive or negative will respectively denote whether axisymmetric or non-axisymmetric modes are dominant at marginal stability. Δ_{Re} can be considered to be a function of $[\eta, \mu, N]$.

The threshold between axisymmetric and non-axisymmetric critical modes corresponds to the region where $\Delta_{Re} = 0$.

To this end, we seek the value of μ for which $\Delta_{Re} = 0$ with fixed $[\eta, N]$, making use of the same root-finding algorithm mentioned in section 3.5.1. We do this for a range of η values and buoyancy frequencies.

7.1.1 Difficulties

As described in section 2.4.6, to find the critical mode for given $[\eta, \mu, N]$ we are optimising the basic SRI-mode program over Re, then optimising those results over k, and then further optimising over m when looking at non-axisymmetric modes. To then find the threshold between axisymmetric and non-axisymmetric critical modes, we are then optimising over μ for given $[\eta, N]$ values.

This requires four nested routines, and demands considerable computational runtime. This is further complicated because computational error at any stage can influence the final result. Computational errors can be reduced by higher resolutions at each stage, but they cannot be eliminated entirely and higher resolutions at any stage will increase the computational runtime.

Furthermore, as stated in section 2.4.6, our critical mode searching program is not perfect, as it only examines finite ranges of wavenumbers and is not well suited to the closed-domain-loop phenomena (Section 6.2.3).

It was also found that, as $\eta \to 1$, the critical SRI mode shifts to higher and higher values of m. This phenomenon only becomes important at around $\eta = 0.95$. For example, $[\eta = 0.95, \mu = 0.95, N = 1.0]$ has a critical mode with $m_c = 7, k_z = 2.8$ and $Re_c = 3062$; whereas $[\eta = 0.99, \mu = 0.9714, N = 1.0]$ has a critical mode with $m_c = 24, k_z = 3.26$ and $Re_c = 3208$. We are therefore forced to significantly increase the range of m that is examined as $\eta \to 1$. For this reason we only examine the threshold up to the value of $\eta = 0.95$.

7.1.2 Prior work

In figure 3 of Shalybkov and Rüdiger [2005], this threshold can be seen to exist at around $\mu = 0.25$ for $\eta = 0.78$ and $Fr = 0.5$, at which point $Re_{m=0} \simeq Re_{m\neq 0}$. The threshold is absent in figure 4 of the same paper, which has $\eta = 0.4$ and $Fr = 0.5$, implying that the threshold does not exist between $0 \leq \mu \leq 1$ for those parameters.

Figure 6.1 for $N = 1.0$ indicates that the threshold is a line in the $[\eta, \mu]$-parameter space

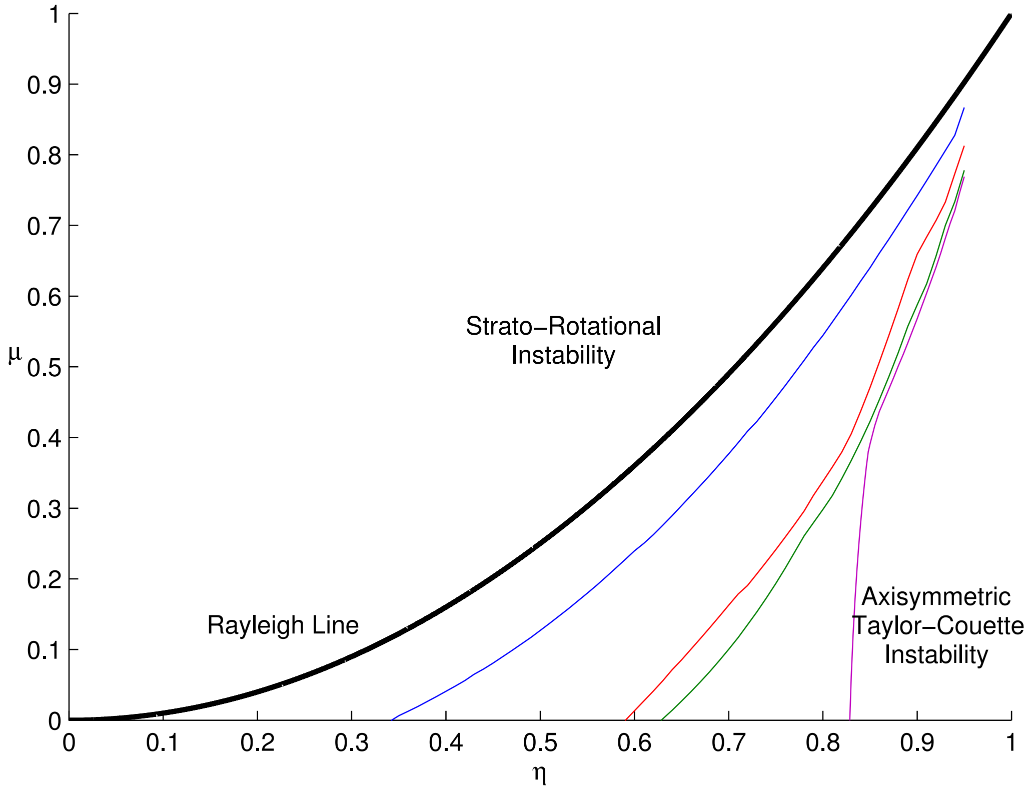

Figure 7.1: The $\mu(\eta)$ bifurcation curve between axisymmetry and the SRI for various values of the buoyancy frequency N: $N = 0.5$ (blue), $N = 1.0$ (red), $N = 1.5$ (green) and $N = 2.5$ (purple). Also shown is the Rayleigh line $\mu = \eta^2$ (thick black). Axisymmetric instabilities dominate as $\eta \to 1$ or $\mu \to 0$, whereas the SRI dominates for smaller values of η and larger values of μ.

with a single value of μ for each value of η. Since $Re_{m=0}$ goes to infinity as the Rayleigh line is approached and axisymmetric instabilities do not exist beyond it (see section 2.4.4), we can also assume that the threshold will always be below the Rayleigh line.

7.1.3 Results

Figure 7.1 depicts the threshold within the $[\eta, \mu]$-parameter space for a variety of buoyancy frequencies.

At weak stratifications, the threshold tends towards the Rayleigh line $\mu = \eta^2$. This makes sense, since the Rayleigh line is the axisymmetric stability limit, and in the limit of zero stratification, all critical modes are axisymmetric.

Interestingly, we here disagree with the results of Leclercq et al. [2016]. In figure 2(e) of that paper, they predict that the non-axisymmetric $m = 1$ mode is the critical mode for all μ up to the limit of stability, for $\eta = 0.417$ and with a Richardson number of $Ri = 0.25$. This Richardson number is equivalent to the square of our dimensionless buoyancy frequency N, hence $Ri = 0.25 \implies N = 0.5$. However, for $N = 0.5$ and $\eta = 0.417$ on 7.1, we predict that the critical mode is the axisymmetric $m = 0$ mode for $\mu < 0.53$. This discrepancy is presumably a result of the density diffusion term $\nabla^2 \rho/(ReSc)$ in their density equation, which is absent in our system. (Sc is the Schmidt number, $Sc = \hat{\nu}/\hat{\kappa}$ where $\hat{\kappa}$ is the diffusivity of mass. Leclercq et al. [2016] typically used $Sc = 700$.)

At stronger stratifications, non-axisymmetric SRI modes increasingly dominate more of the parameter space, and the threshold line appears to move towards the line $\eta = 1$. It appears to be the case that the limit $\eta \to 1$ is always kept within the axisymmetric domain. This would suggest that the classical narrow gap limit explored by Chandrasekhar [1961] ($\eta \to 1$ for some constant $\mu < 1$) always has an axisymmetric critical mode even in the presence of stratification.

However for all stratifications the threshold line between axisymmetric and non-axisymmetric critical mode instabilities appears to pass through $[\eta \to 1, \mu \to 1]$, with the range $[\eta \to 1,\ 0 \leq \mu < 1]$ corresponding to axisymmetric instabilities. This suggests that the SRI could persist as a critical mode into a near-solid-body-rotation narrow-gap limit with $[\eta \to 1,\ \mu \to 1]$, dependent upon the relationship between η and μ as the limit is approached.

This near-solid-body-rotation narrow-gap limit was previously explored by Yavneh et al. [2001] in the inviscid domain. Although working in different terminology, they took $\eta \to 1$ while holding the relative strain rate $S(r) = -B/(Ar^2 + B)$ at $O(1)$, which necessitates that $\mu \to 1$ also. They showed that in this limit the combined inviscid equation for the SRI (2.48) becomes the equivalent equation for an inviscid rotating shear flow.

7.2 The Near-Solid-Body-Rotation Narrow-Gap Limit

The non-dimensionalised viscous SRI equations (see chapter 2) are:

$$-i\Phi u - 2\Omega v = -\frac{dP}{dr} + \frac{\eta}{(1-\eta)}\frac{1}{Re}\left[\frac{d^2u}{dr^2} + \frac{1}{r}\frac{du}{dr} - \left(\frac{m^2+1}{r^2} + k^2\right)u - \frac{2im}{r^2}v\right], \quad (7.1)$$

$$-i\Phi v + \zeta u = -i\frac{m}{r}P + \frac{\eta}{(1-\eta)}\frac{1}{Re}\left[\frac{d^2v}{dr^2} + \frac{1}{r}\frac{dv}{dr} - \left(\frac{m^2+1}{r^2} + k^2\right)v + \frac{2im}{r^2}u\right], \quad (7.2)$$

$$-i\Phi w = -ikP - \rho + \frac{\eta}{(1-\eta)}\frac{1}{Re}\left[\frac{d^2w}{dr^2} + \frac{1}{r}\frac{dw}{dr} - \left(\frac{m^2}{r^2} + k^2\right)w\right], \quad (7.3)$$

$$-i\Phi\rho - N^2 w = 0, \quad (7.4)$$

$$\frac{du}{dr} + \frac{u}{r} + i\frac{m}{r}v + ikw = 0. \quad (7.5)$$

with boundary conditions:

$$r = [r_1, r_2] \implies u = v = w = 0. \quad (7.6)$$

and the following defined quantities:

$$\Phi = i\sigma_r + f - m\Omega, \quad \Omega(r) = A + \frac{B}{r^2}, \quad \zeta = \frac{1}{r}\frac{d}{dr}\left(r^2\Omega\right) = 2A,$$

$$A = \frac{\mu - \eta^2}{1-\eta^2}, \quad B = \frac{\eta^2(1-\mu)}{(1+\eta)(1-\eta)^3}. \quad (7.7)$$

To take the double limit of $[\eta \to 1,\ \mu \to 1]$, we first need to establish a fixed relationship between η and μ such that, if either variable is taken to the limit, the other variable is forced to follow. To this end we define a constant ratio β between $1-\mu$ and $1-\eta$:

$$\beta = \frac{1-\mu}{1-\eta} = O(1). \quad (7.8)$$

Note that $\beta = 0$ corresponds to solid body rotation $\mu = 1$, and that $\beta = 1$ corresponds to the line $\mu = \eta$. The meaning of β is explored further in section 7.2.1.

We are now free to choose our small parameter. We use $\epsilon = 1 - \eta$ and take the limit $\epsilon \to 0$, allowing us to write:

$$\eta = 1 - \epsilon, \quad \mu = 1 - \epsilon\beta. \quad (7.9)$$

Since all radial values within $r_1 \leq r \leq r_2$ will go to infinity as $\eta \rightarrow 1$, we require a different independent variable to the radius. We define:

$$r = r_1 + x, \quad \frac{d}{dr} = \frac{d}{dx}. \tag{7.10}$$

such that $x = 0$ at $r = r_1$ and $x = 1$ at $r = r_2$.

This allows us to calculate r in terms of ϵ and x:

$$r = \frac{1-\epsilon}{\epsilon} + x,$$

$$\implies r = \frac{1}{\epsilon} + (x-1). \tag{7.11}$$

We need the limiting behaviour of Ω. Substituting η and μ for β and ϵ into A and B we have:

$$A = \frac{(1-\epsilon\beta) - (1-\epsilon)^2}{1-(1-\epsilon)^2}, \quad B = \frac{(1-\epsilon)^2 \beta\epsilon}{(1+(1-\epsilon))\,\epsilon^3};$$

Solving for A:

$$A = \frac{2-\beta-\epsilon}{2-\epsilon};$$

$$A = 1 - \frac{\beta}{2} - \frac{\epsilon\beta}{4} + O(\epsilon^2). \tag{7.12}$$

Solving for B/r^2:

$$\frac{B}{r^2} = \frac{(1-\epsilon)^2 \beta\epsilon}{(1+(1-\epsilon))\,\epsilon^3}\left(\frac{\epsilon}{1+\epsilon\,(x-1)}\right)^2;$$

$$\frac{B}{r^2} = \frac{(1-2\epsilon+\epsilon^2)\,\beta}{(2-\epsilon)\,(1+\epsilon\,(x-1))^2};$$

$$\frac{B}{r^2} = \frac{\beta}{2}\left(1-2\epsilon+\epsilon^2\right)\left(1-\epsilon\left(2x-\frac{5}{2}\right)+O(\epsilon^2)\right);$$

$$\frac{B}{r^2} = \frac{\beta}{2} + \frac{\epsilon\beta}{4} - \epsilon\beta x + O(\epsilon^2). \tag{7.13}$$

Therefore, substituting for $\Omega = A + B/r^2$ and working to $O(\epsilon)$:

$$\Omega(x) = 1 - \epsilon\beta x; \tag{7.14}$$

and:

$$\zeta = 2A = 2 - \beta - \frac{\epsilon\beta}{2}. \tag{7.15}$$

In the narrow gap limit, we make the approximation that (m/r) tends towards a constant horizontal wavenumber, i.e.:

$$\frac{m}{r} \to k_y, \quad m \to \frac{k_y}{\epsilon}.$$

To distinguish between terms, we also relabel the vertical wavenumber k as k_z.

With the limiting behaviour of Ω and the horizontal wavenumber, we can derive the near-solid-body narrow-gap form of Φ:

$$\Phi = i\sigma_r + f - \frac{k_y}{\epsilon}\left(1 - \epsilon\beta x\right),$$

$$\implies \Phi = i\sigma_r + f - \frac{k_y}{\epsilon} + k_y\beta x.$$

We can now define the adapted frequency $f^* = f - k_y/\epsilon$. This expression is equivalent to $f^* = f - m$, and allows us to write:

$$\Phi = i\sigma_r + f^* + k_y\beta x. \tag{7.16}$$

(Note that f^* does *not* denote the complex conjugate of f.)

Substituting (7.8)-(7.16) into the SRI equations (7.1)-(7.5) leads to:

$$-i\Phi u - 2\left(1 - \epsilon\beta x\right)v = -\frac{dP}{dx} + \frac{1}{\epsilon Re}\left[\frac{d^2u}{dx^2} + \epsilon\frac{du}{dx} - \left(k_y^2 + k_z^2 + \epsilon^2\right)u - 2i\epsilon k_y v\right],$$

$$-i\Phi v + \left(2 - \beta\right)u = -ik_yP + \frac{1}{\epsilon Re}\left[\frac{d^2v}{dx^2} + \epsilon\frac{dv}{dx} - \left(k_y^2 + k_z^2 + \epsilon^2\right)v + 2i\epsilon k_y u\right],$$

$$-i\Phi w = -ik_zP - \rho + \frac{1}{\epsilon Re}\left[\frac{d^2w}{dx^2} + \epsilon\frac{dw}{dx} - \left(k_y^2 + k_z^2\right)w\right],$$

$$-i\Phi\rho - N^2 w = 0,$$

$$\frac{du}{dx} + \epsilon u + ik_y v + ik_z w = 0.$$

The form of these equations suggests a rescaling of the Reynolds number such that $\epsilon Re = Re^*$. This leads to, in dimensional units:

$$Re^* = \frac{1}{\nu} = \frac{\hat{\lambda}^2\hat{\Omega}_{\text{in}}}{\hat{\nu}}, \tag{7.17}$$

Substituting in (7.17) and dropping terms that are directly smaller than adjacent terms, we have:

$$-i\Phi u - 2v = -\frac{dP}{dx} + \frac{1}{Re^*}\left[\frac{d^2u}{dx^2} - \left(k_y^2 + k_z^2\right)u\right], \tag{7.18}$$

$$-i\Phi v + (2-\beta)\, u = -ik_y P + \frac{1}{Re^*}\left[\frac{d^2v}{dx^2} - \left(k_y^2 + k_z^2\right) v\right], \tag{7.19}$$

$$-i\Phi w = -ik_z P - \rho + \frac{1}{Re^*}\left[\frac{d^2w}{dx^2} - \left(k_y^2 + k_z^2\right) w\right], \tag{7.20}$$

$$-i\Phi\rho - N^2 w = 0, \tag{7.21}$$

$$\frac{du}{dx} + ik_y v + ik_z w = 0. \tag{7.22}$$

The remaining terms can be assumed to all balance with each other. These are the SRI Near-Solid-Body-Rotation Narrow-Gap equations.

7.2.1 β as a measure of the Flow Shear

From (7.14), we have $\Omega = 1 - \epsilon\beta x$. Differentiating by x allows us to conclude that:

$$\beta = -\frac{1}{\epsilon}\frac{d\Omega}{dx}.$$

β can therefore be considered to be a scaled non-dimensional measure of the flow shear. Note also that, from our original definition, $\beta > 0$ corresponds to $\mu < 1$ and vice versa, with $\beta = 0$ corresponding to solid body rotation.

7.3 Rotating Stratified Shear flow

In the near-solid-body-rotation narrow-gap limit, the inviscid SRI system is equivalent to the inviscid stratified rotating shear flow system, as shown by Yavneh et al. [2001]. Kushner et al. [1998] demonstrated that a similar rotating shear flow system, with shallow water instead of stratification, was susceptible to a Kelvin wave instability; hence Yavneh et al. [2001] concluded that the SRI was itself a Kelvin wave instability.

In this section we will derive the equations of the viscous rotating shear flow system, in order to demonstrate the connection between that system and the near-solid-body narrow-gap limit of the viscous stratified Taylor-Couette system. This serves to extend the work done by Yavneh et al. [2001] to the viscous domain.

Rotating Stratified Shear Flow (RSSF), as described by Yavneh et al. [2001], is the stratified shear flow between two parallel infinite vertical walls in a rotating $[\hat{x}, \hat{y}, \hat{z}]$ frame.

7.3.1 Flow equations

We place our vertical walls at $\hat{x} = 0$ and $\hat{x} = \hat{L}$. The viscous flow is stimulated by equal and opposite sliding of the walls in the $\hat{y}$-direction. The walls have velocity $\pm\hat{V}_0$. The $\hat{z}$-direction is the vertical direction of gravity, stratification and rotation. The rotation vector of the frame is $\hat{\boldsymbol{\Omega}}_{\mathbf{0}} = \hat{\Omega}_0 \boldsymbol{e_z}$.

Non-Dimensionalisation of the RSSF system

We define our Reynolds number for the rotating shear flow system as:

$$\tilde{Re} = \frac{\hat{L}^2\hat{\Omega}_0}{\hat{\nu}}.$$

We are examining a new system, so we need a new length-scale and a new time-scale. Similar to the Taylor-Couette system, we use as our length-scale the gap width between the walls such that $\hat{\lambda} = \hat{L}$, and as our time-scale we use the reciprocal of the constant background rotation such that $\hat{\tau} = \hat{\Omega}_0^{-1}$. We again measure the density in terms of a constant reference density $\hat{\rho}_q$, which gives us a pressure-scale $\hat{P}_q = \hat{\rho}_q\hat{\lambda}^2\hat{\tau}^{-2}$.

We now make the transition to non-dimensional co-ordinates by rescaling our terms such that $[\hat{x}, \hat{y}, \hat{z}] = \hat{\lambda}[x, y, z]$ and $\hat{V}_0 = V_0\hat{\lambda}\hat{\tau}^{-1}$. In these units the walls are at $x = 0$ and $x = 1$, and we have:

$$\hat{\boldsymbol{\Omega}}_{\mathbf{0}} = \boldsymbol{\Omega}_{\mathbf{0}}\tau^{-1}, \qquad \Longrightarrow \qquad \boldsymbol{\Omega}_{\mathbf{0}} = \boldsymbol{e_z}.$$

System equations

We start with the system equations for stratified fluid flow (see section 2.2) in a rotating frame:

$$\frac{\partial \boldsymbol{u}}{\partial t} + \boldsymbol{u}.\boldsymbol{\nabla}\boldsymbol{u} = -\boldsymbol{\nabla}P' - 2\boldsymbol{\Omega}\times\boldsymbol{u} - \boldsymbol{\nabla}\phi_c - \rho'\boldsymbol{g} + \frac{1}{\tilde{Re}}\boldsymbol{\nabla}^2\boldsymbol{u}, \tag{7.23}$$

$$\boldsymbol{\nabla}.\boldsymbol{u} = 0. \tag{7.24}$$

$$\frac{\partial \rho'}{\partial t} + \boldsymbol{u}.\boldsymbol{\nabla}\rho' = 0. \tag{7.25}$$

Here $-2\boldsymbol{\Omega} \times \boldsymbol{u}$ is the Coriolis force and $-\boldsymbol{\nabla}\phi_c$ is the centrifugal force, expressed as a potential gradient. We have already taken the Boussinesq approximation (section 2.2.5), again setting $\hat{\rho}_q$ such that the background density $\bar{\rho} = 1$. The buoyancy frequency is the same as in section 2.2.6, yielding the following formula for the dimensionless gravity g in terms of the basic state density distribution ρ_0' (2.16):

$$g = -N^2 \left(\frac{d\rho_0'}{dz}\right)^{-1}.$$

The centrifugal force and the pressure term can be compared and combined, to produce a new adapted pressure $\tilde{P} = P' + \phi_c$. This allows us to absorb the centrifugal term into the pressure term. Dropping the ˜ from this adapted pressure term, we now have:

$$\frac{\partial \boldsymbol{u}}{\partial t} + \boldsymbol{u}.\boldsymbol{\nabla}\boldsymbol{u} + 2\boldsymbol{\Omega} \times \boldsymbol{u} = -\boldsymbol{\nabla}P - \rho'\boldsymbol{g} + \frac{1}{\tilde{Re}}\boldsymbol{\nabla}^2\boldsymbol{u},$$

$$\boldsymbol{\nabla}.\boldsymbol{u} = 0,$$

$$\frac{\partial \rho'}{\partial t} + \boldsymbol{u}.\boldsymbol{\nabla}\rho' = 0.$$

We have previously defined that $\boldsymbol{\Omega} = \boldsymbol{e_z}$ and therefore we know that $2\boldsymbol{\Omega}\times\boldsymbol{u} = (-2v, 2u, 0)$. Expanding out we then have:

$$\frac{\partial \boldsymbol{u}}{\partial t} + \boldsymbol{u}.\boldsymbol{\nabla}\boldsymbol{u} - 2u_y\boldsymbol{e_x} + 2u_x\boldsymbol{e_y} = -\boldsymbol{\nabla}P - \rho'\boldsymbol{g} + \frac{1}{\tilde{Re}}\boldsymbol{\nabla}^2\boldsymbol{u},$$

$$\boldsymbol{\nabla}.\boldsymbol{u} = 0,$$

$$\frac{\partial \rho'}{\partial t} + \boldsymbol{u}.\boldsymbol{\nabla}\rho' = 0.$$

We have two moving boundary walls at $x = 0$ and $x = 1$, both moving with speed V_0 in opposite directions. The flow is unbounded in the y and z directions. We set the non-slip boundary conditions (with $V_0 =$ const.):

$$\boldsymbol{u}(x=0) = V_0\boldsymbol{e_y}, \quad \boldsymbol{u}(x=1) = -V_0\boldsymbol{e_y}.$$

We now try the following basic state velocity: $\boldsymbol{u_0} = V(x)\boldsymbol{e_y} = V_0\left(1-2x\right)\boldsymbol{e_y}$. (Note that $\boldsymbol{\nabla . u} = \boldsymbol{0}$ is satisfied by design.)

$$\implies -2V_0\left(1-2x\right)\boldsymbol{e_x} = -\boldsymbol{\nabla} P_0 - \rho_0'\boldsymbol{g}.$$

Separating this equation into components yields the following set of conditions on P_0 and ρ_0':

$$\frac{\partial P_0}{\partial x} = 2V_0\left(1-2x\right), \quad \frac{\partial P_0}{\partial y} = 0, \quad \frac{\partial P_0}{\partial z} = -\rho_0' g. \tag{7.26}$$

We assume that a basic state pressure distribution P_0 exists which satisfies these conditions.

Perturbations

We now introduce small perturbations to the system such that $a = a_0 + a_1$ with $a_1 \ll a_0$. We do this for $a = [u_x, u_y, u_z, P, \rho]$, and assume that the a_0 terms satisfy the basic state system. As before, for the density perturbation we include a factor of $1/g$ such that $\rho' = \rho_0' + \rho_1/g$. Applying this to the system, cancelling basic state terms and retaining only terms to first order in perturbations, we get:

$$\frac{\partial \boldsymbol{u_1}}{\partial t} + \boldsymbol{u_1 . \nabla u_0} + \boldsymbol{u_0 . \nabla u_1} - 2u_{1y}\boldsymbol{e_x} + 2u_{1x}\boldsymbol{e_y} = -\boldsymbol{\nabla} P_1 + \rho_1 \boldsymbol{e_z} + \frac{1}{\tilde{Re}}\boldsymbol{\nabla}^2 \boldsymbol{u_1},$$

$$\frac{\partial \rho_1}{\partial t} + g\boldsymbol{u_1 . \nabla}\rho_0 + \boldsymbol{u_0 . \nabla}\rho_1 = 0,$$

$$\boldsymbol{\nabla . u_1} = 0.$$

We assume that all perturbation variables have the form $a_1(x,y,z,t) = \tilde{a}(x)\exp(\sigma t + i[k_y y + k_z z])$. We then have:

$$\boldsymbol{u_0 . \nabla} a_1 = V\frac{\partial a_1}{\partial y} = ik_y V a_1.$$

Therefore:

$$\sigma \boldsymbol{u_1} + ik_y V \boldsymbol{u_1} + \boldsymbol{u_1 . \nabla u_0} - 2u_{1y}\boldsymbol{e_x} + 2u_{1x}\boldsymbol{e_y} = -\boldsymbol{\nabla} P_1 + \rho_1 \boldsymbol{e_z} + \frac{1}{\tilde{Re}}\boldsymbol{\nabla}^2 \boldsymbol{u_1},$$

$$\sigma\rho_1 + ik_y V\rho_1 + g\boldsymbol{u_1 . \nabla}\rho_0 = 0,$$

$$\boldsymbol{\nabla . u_1} = 0.$$

Dropping the 1 subscript and continuing:

$$\sigma \boldsymbol{u} + ik_y V \boldsymbol{u} + u_x \frac{\partial \boldsymbol{u_0}}{\partial x} - 2u_y \boldsymbol{e_x} + 2u_x \boldsymbol{e_y} = -\boldsymbol{\nabla} P + \rho \boldsymbol{e_z} + \frac{1}{\tilde{Re}} \boldsymbol{\nabla}^2 \boldsymbol{u},$$

$$\sigma \rho + ik_y V \rho + g u_z \frac{\partial \rho_0}{\partial z} = 0,$$

$$\frac{\partial u_x}{\partial x} + ik_y u_y + ik_z u_z = 0.$$

If we split the system into multiple equations, introduce $N^2 = -g\partial\rho_0/\partial z$ and $\Phi = i\sigma - k_y V$, and expand out $\boldsymbol{\nabla}^2$, we attain:

$$-i\Phi u_x - 2u_y = -\frac{\partial P}{\partial x} + \frac{1}{\tilde{Re}} \left[\frac{\partial^2 u_x}{\partial x^2} - \left(k_y^2 + k_z^2\right) u_x \right], \tag{7.27}$$

$$-i\Phi u_y + \left(2 - 2V_0\right) u_x = -ik_y P + \frac{1}{\tilde{Re}} \left[\frac{\partial^2 u_y}{\partial x^2} - \left(k_y^2 + k_z^2\right) u_y \right], \tag{7.28}$$

$$-i\Phi u_z = -ik_z P - \rho + \frac{1}{\tilde{Re}} \left[\frac{\partial^2 u_z}{\partial x^2} - \left(k_y^2 + k_z^2\right) u_z \right], \tag{7.29}$$

$$-i\Phi \rho - N^2 u_z = 0, \tag{7.30}$$

$$\frac{\partial u_x}{\partial x} + ik_y u_y + ik_z u_z = 0. \tag{7.31}$$

Comparing equations (7.18-7.22) with (7.27-7.31), we can see that the near-solid-body narrow gap SRI system and the RSSF system are mathematically identical, with $\beta \iff 2V_0$ and $Re^* \iff \tilde{Re}$.

7.4 Comparing SRI and RSSF modes

To further test the correlation between the SRI and RSSF systems, we can compare critical eigenmodes between the two systems. Figure 6.3 is an SRI mode close to the near-solid-body narrow-gap limit, with $\eta = 0.95$, $\mu = 0.95$ and $N = 1.0$. From this we can calculate that $\beta = (1-\mu)/(1-\eta) = 1.0$ and that $\epsilon = 1 - \eta = 0.05$. To compare this mode to the RSSF system, we can calculate the critical RSSF mode for $\beta = 1.0$ and $N = 1.0$, which is shown in figure 7.2.

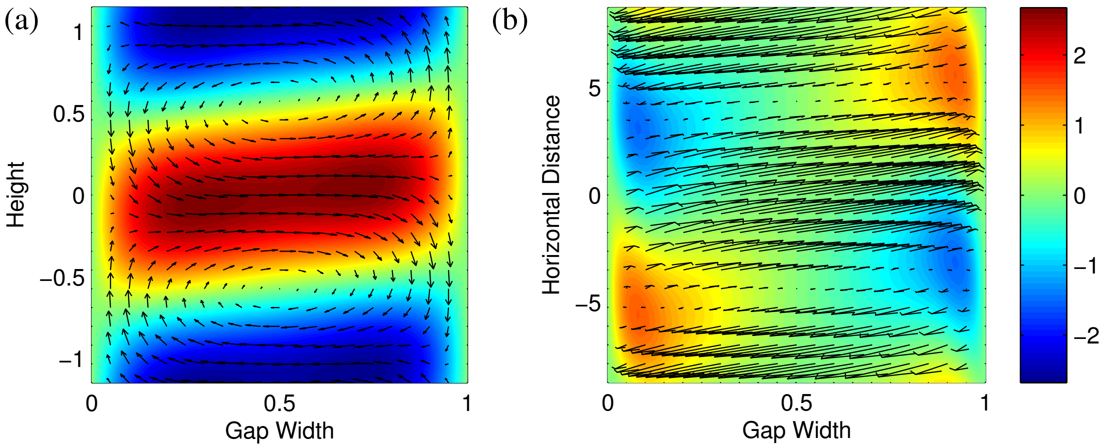

Figure 7.2: An eigenfunction from the rotating shear flow, with $\beta = 1.00, N = 1.0$, with $Re_c^* = 157.4, k_y = 0.36, k_z = 2.74$ and $f^* = -0.180$. This figure uses the same conventions as in chapter 6.

SRI	η	μ	N	ϵm	k	ϵRe	$f - m$
	0.95	0.95	1.0	0.35	2.8	153.1	-0.181
RSSF	ϵ	β	N	k_y	k_z	Re^*	f^*
	0.05	1.0	1.0	0.36	2.74	157.4	-0.180

Table 7.1: Comparing RSSF terms to their derived counterparts from the corresponding SRI mode.

The two eigenmodes are visually very similar. Furthermore, we can compare terms, as from section 7.2 we expect that $k_y \approx \epsilon m$, $k_z \approx k$, $Re_c^* \approx \epsilon Re$ and $f^* \approx f - m$. These terms are compared in table 7.1, and we again see a strong correlation.

7.5 Re* vs. β

Figure 7.3 examines the behaviour of the RSSF system as β is varied. It can be seen that horizontally stationary modes with $k_y = 0$ reach a stability limit at around $\beta = 2$. This correlates with the Rayleigh line stability limit for $m = 0$ modes in the stratified Taylor-Couette system; note that the Rayleigh line in the near-solid-body narrow-gap limit tends towards $\beta = 2$.

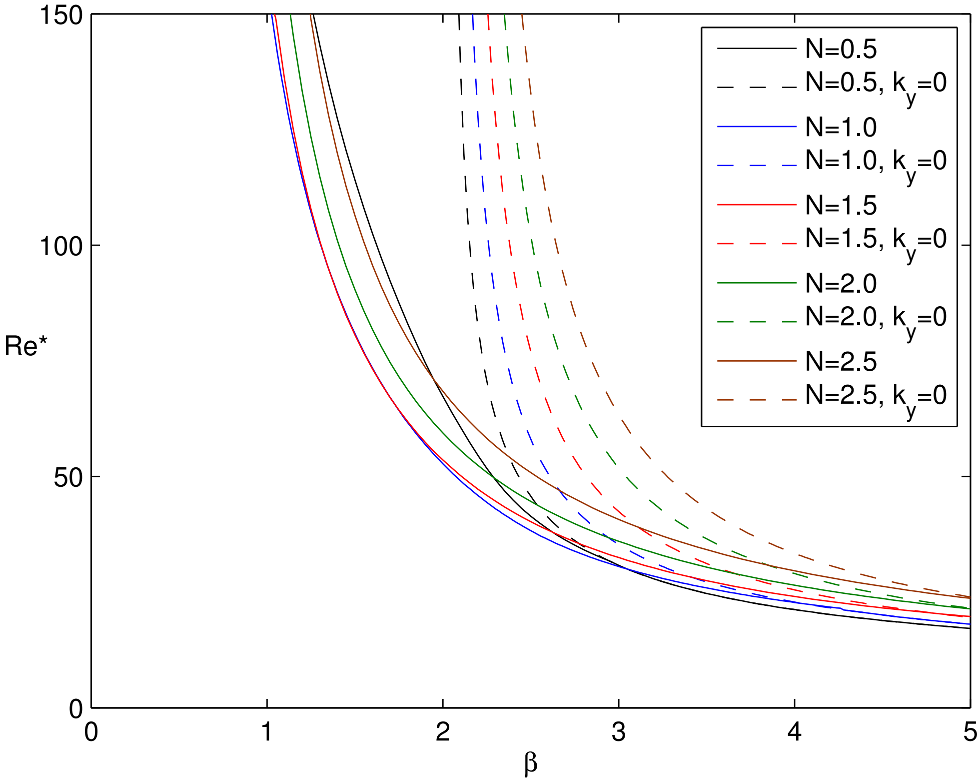

Figure 7.3: A comparison between the critical RSSF Reynolds numbers Re^* for horizontally stationary modes with $k_y = 0$ (dashed lines) and propagating modes for which k_y (solid lines) has been optimised.

However, modes for which k_y is unrestricted persist towards $\beta = 0$, seemingly reaching a stability limit close to $\beta = 0.5$. This presumably corresponds to the $N = 1.0$ stability limit of the SRI taken to the near-solid-body narrow-gap limit. This suggests that the gradient of the SRI stability limit for $N = 1.0$ is approximately tangential to $\mu = 0.5\eta + 0.5$ as the RSSF limit is approached.

7.6 Conclusion

For the SRI to remain relevant, the narrow gap limit of the Taylor-Couette requires that the system also be taken to the near-solid-body limit. This combined limit was shown by Yavneh et al. [2001] to be equivalent to the rotating shear flow system for inviscid flows. We have extended this work to show that this equivalence also holds for viscous flows.

In support of this assertion, we have demonstrated strong similarities between rotating shear flow modes and SRI modes that are close to the limit, both in appearance and in parameter values.

Chapter 8

Conclusions and Future Work

The original motivation for this work was to examine the stability limits of the Strato-Rotational Instability (SRI) in order to provide insight into methods by which a centrifugally stable astrophysical disc might be destabilised.

It should be noted that the classical SRI, which we have dubbed the dual-wave-mode SRI, requires solid boundary walls in order to induce the two wave-like regions upon which the Kelvin wave instability mechanism depends. Such boundary conditions are unlikely to be satisfied within an astrophysical context. However over the course of this work, we have shown that the dual-wave-mode SRI is not the only form of the instability. There is of course the Radiative Instability (RI) of Le Dizès and Riedinger [2010], seen as the critical mode of instability in our figure 6.12. We have also found a wall-mode SRI, a wide-gap-mode SRI, and a pseudo-radiative-mode SRI in the viscous domain. Judging from their eigenmode appearance (figures 6.6 and 6.8), the wide-gap and wall-modes appear to utilise different instability mechanisms compared to the Kelvin wave instability mechanism of the dual-wave-mode SRI. The pseudo-radiative-mode (figure 6.7) is continuously connected to the dual-wave-mode, and presumably uses a combination of the radiative instability mechanism and the Kelvin wave instability mechanism. We propose that the pseudo-radiative-mode continuously transforms into the RI as the gap width is widened, paralleling the inviscid wide-gap limit taken in Le Dizès and Riedinger [2010]. Note that the mode may not necessarily remain as the critical mode as the viscous wide gap limit is taken.

At weak stratifications, we have shown that a region of the parameter space can become viscously unstable when the inviscid system appears to be stable. It is within this region that we have found the RI as critical mode of instability for moderate gap widths. Significantly, the presence of the RI here appears to rely upon the existence of a radial layer for which $\Phi^2 - N^2 = 0$. This same radial layer would cause a singular term within the inviscid system, hence preventing unstable inviscid solutions from being found. We therefore conclude that inviscid analysis may be insufficient for weak stratifications of the Taylor-Couette system.

Experimental verification of the wall-mode SRI and wide-gap-mode SRI would be useful. The instability mechanisms of these two modes should also be further investigated, as they are visibly distinct from the dual-wave-mode SRI that has already been understood as a Kelvin wave instability [Yavneh et al., 2001].

We have extended the domain of viscously unstable stratified Taylor-Couette flow beyond the work of Shalybkov and Rüdiger [2005] and Rüdiger and Shalybkov [2009]. We have also demonstrated the existence of viscous closed domain loops in the $[m, k, Re]$-parameter space. These appear to extend the unstable domain of the viscous dual-wave-mode SRI compared to the inviscid predictions. However they can be computationally problematic to detect, since they only exist for a finite region of the parameter-space and an exhaustive search can be required to find them. The discovery of closed domain loops could be considered an extension of the work of Ibanez et al. [2016], who showed that increasing the Reynolds number could switch off the SRI. We have been able to reasonably reproduce the experimental results of Ibanez et al. [2016] with our computational solver, see figure 5.2.

We have also shown that the inviscid domain of stratified Taylor-Couette flow is unconditionally unstable for co-rotating flows with $\mu < 1$ and $N > 2$. Notably in our choice of units, $N = 2$ is equivalent to a Froude number of $Fr = 0.5$, which is comparable to the estimated Froude number of an astrophysical disc [Shalybkov and Rüdiger, 2005]. We have therefore extended the work of Park and Billant [2013] in order to derive stability limits on η and μ for given N and $\mu < 1$. The conditions originally derived by Park and Billant [2013] are altered slightly for the case $\mu > 1$, however a similar set of conditions should be derivable. It should also be noted that Park and Billant [2013]'s work only applies for the dual-wave-mode SRI; it may be possible to further derive similar inviscid instability conditions for the wall-mode SRI, the wide-gap-mode SRI and the radiative instability, once their instability mechanisms have been better understood.

Examining narrow gap flows, we have shown numerically that axisymmetric perturbations ($m = 0$) are always the critical viscous mode as the limit $\eta \to 1$ is taken with constant μ. However, the joint limit of near-solid-body narrow gap flows, i.e. $[\eta, \mu] \to [1, 1]$, can be taken such that non-axisymmetric perturbations remain as the critical viscous mode. In this context we have shown that the viscous system becomes mathematically equivalent to the perturbation equations of a stratified rotating shear flow. This can be considered an extension of the work of Yavneh et al. [2001], who showed the same equivalence for the inviscid system. It may be useful to experimentally verify the connection between the instability modes of a stratified rotating shear flow, and that of narrow-gap near-solid-body stratified Taylor-Couette flow.

The original inspiration for this work was to investigate methods by which an astrophysical disc could be made unstable. The Magneto-Rotational Instability (MRI) [Balbus and Hawley, 1991] is a viable candidate, but only in cases where the fluid is expected to be ionised. The dual-wave-mode SRI is not thought to be relevant, due to the instability's reliance upon the presence of inner and outer solid boundary conditions. So far the wall-mode and wide-gap-mode SRI have also only been found for the same boundary conditions, although it is not yet known whether they are reliant upon the solid boundary conditions. It has, however, been demonstrated that the radiative instability (RI) does not require an outer boundary condition.

The RI only requires an inner boundary condition. Notably, astrophysical discs do always have an inner boundary conditions. This takes the form of either flow onto the central object, or the form of a central hole between the disc and the central object. It is therefore worth investigating whether the RI can be preserved in the presence of an inner boundary condition corresponding more closely to the astrophysical context. In this regard, the radiative instability can be considered a strong candidate for the destabilisation of astrophysical discs, and is worthy of further study.

Appendices

A Combined Inviscid Equation

We begin with equations (2.42-2.46), restated here for reference:

$$-i\Phi u - 2\Omega v = -\frac{dP}{dr}, \tag{A.1}$$

$$-i\Phi v + \zeta u = -i\frac{m}{r}P, \tag{A.2}$$

$$-i\Phi w = -ikP - \rho, \tag{A.3}$$

$$-i\Phi\rho - N^2 w = 0, \tag{A.4}$$

$$\frac{du}{dr} + \frac{u}{r} + i\frac{m}{r}v + ikw = 0. \tag{A.5}$$

We can rewrite (A.3) as $\rho = i\Phi w - ikP$, and therefore substitute for ρ in (A.4):

$$\left(\Phi^2 - N^2\right) w = k\Phi P,$$

$$\implies w = \frac{k\Phi}{\Phi^2 - N^2}P. \tag{A.6}$$

We can use (A.6) to substitute for w in (A.5):

$$\frac{du}{dr} + \frac{u}{r} + i\frac{m}{r}v + \frac{ik^2\Phi}{\Phi^2 - N^2}P = 0. \tag{A.7}$$

This leaves us with a system of three variables, $[u, v, P]$, with three equations: (A.1), (A.2) and (A.7).

From (A.2) we can write an equation for v:

$$v = \frac{m}{r\Phi}P - i\frac{\zeta}{\Phi}u. \tag{A.8}$$

Substituting (A.8) into (A.1) to eliminate v yields:

$$\begin{aligned}
-ir\Phi^2 u - 2\Omega\left(mP - i\zeta r u\right) &= -r\phi\frac{dP}{dr}, \\
\left(2\Omega\zeta - \Phi^2\right) iru &= 2\Omega mP - r\phi\frac{dP}{dr}, \\
\frac{dP}{dr} + \frac{i\Delta}{\Phi}u - \frac{2\Omega m}{r\Phi}P &= 0. \qquad \text{(A.9)}
\end{aligned}$$

Here we have defined the quantity Δ:

$$\Delta(r) = 2\Omega\zeta - \Phi^2. \qquad \text{(A.10)}$$

Substituting (A.8) into (A.7) to eliminate v yields an equation for P in terms of u:

$$\begin{aligned}
\Phi\frac{du}{dr} + \Phi\frac{u}{r} + i\frac{m}{r}\left(\frac{m}{r}P - i\zeta u\right) + \frac{ik^2\Phi^2}{\Phi^2 - N^2}P &= 0, \\
\Phi\frac{du}{dr} + \left(\Phi + m\zeta\right)\frac{u}{r} + i\left(\frac{m^2}{r^2} - \frac{k^2\Phi^2}{N^2 - \Phi^2}\right)P &= 0, \\
\Phi\frac{du}{dr} + \left(\Phi + m\zeta\right)\frac{u}{r} &= -iQP, \\
P &= \frac{i}{Q}\left(\Phi\frac{du}{dr} + \frac{1}{r}\left(\Phi + m\zeta\right)u\right). \qquad \text{(A.11)}
\end{aligned}$$

Here we have defined the quantity Q:

$$Q(r) = \frac{m^2}{r^2} - \frac{k^2\Phi^2}{N^2 - \Phi^2}. \qquad \text{(A.12)}$$

We can use (A.11) to calculate an equation for dP/dr:

$$\begin{aligned}
\frac{dP}{dr} &= i\left[\frac{d}{dr}\left(\frac{\Phi}{Q}\frac{du}{dr} + \frac{1}{Qr}\left(\Phi + m\zeta\right)u\right)\right], \\
\frac{dP}{dr} &= \frac{i\Phi}{Q}\left[\frac{d^2u}{dr^2} + \frac{Q}{\Phi}\frac{d}{dr}\left(\frac{\Phi}{Q}\right)\frac{du}{dr} + \frac{Q}{\Phi}\frac{d}{dr}\left(\frac{1}{Qr}\left(\Phi + m\zeta\right)u\right)\right], \\
\frac{dP}{dr} &= \frac{i\Phi}{Q}\left[\frac{d^2u}{dr^2} + \frac{Q}{\Phi}\frac{d}{dr}\left(\frac{\Phi}{Q}\right)\frac{du}{dr} + \frac{1}{\Phi}\left(\frac{\Phi + m\zeta}{r}\right)\frac{du}{dr} + \frac{Q}{\Phi}\frac{d}{dr}\left(\frac{\Phi + m\zeta}{Qr}\right)u\right], \\
\frac{dP}{dr} &= \frac{i\Phi}{Q}\left[\frac{d^2u}{dr^2} + \left(\frac{1}{r} + \frac{Q}{\Phi}\frac{d}{dr}\left(\frac{\Phi}{Q}\right) + \frac{m\zeta}{r\Phi}\right)\frac{du}{dr} + \frac{Q}{\Phi}\frac{d}{dr}\left(\frac{\Phi + m\zeta}{Qr}\right)u\right]. \qquad \text{(A.13)}
\end{aligned}$$

We can now use (A.11) and (A.13) to substitute P and dP/dr into (A.9):

$$\begin{aligned}
&\frac{i\Phi}{Q}\left[\frac{d^2u}{dr^2} + \left(\frac{1}{r} + \frac{Q}{\Phi}\frac{d}{dr}\left(\frac{\Phi}{Q}\right) + \frac{m\zeta}{r\Phi}\right)\frac{du}{dr} + \frac{Q}{\Phi}\frac{d}{dr}\left(\frac{\Phi + m\zeta}{Qr}\right)u\right] \\
&\qquad\qquad + \frac{i\Delta}{\Phi}u - \frac{2\Omega m}{r\Phi}\frac{i}{Q}\left(\Phi\frac{du}{dr} + \frac{1}{r}\left(\Phi + m\zeta\right)u\right) = 0,
\end{aligned}$$

This can be written as:

$$\frac{d^2u}{dr^2} + a_1\frac{du}{dr} + a_2 u = 0, \tag{A.14}$$

with:

$$a_1 = \frac{1}{r} + \frac{Q}{\Phi}\frac{d}{dr}\left(\frac{\Phi}{Q}\right) + \frac{m\zeta}{r\Phi} - \frac{2\Omega m}{r\Phi},$$

$$a_2 = \frac{Q\Delta}{\Phi^2} - \frac{2\Omega m\left(\Phi + m\zeta\right)}{r^2\Phi^2} + \frac{Q}{\Phi}\frac{d}{dr}\left(\frac{\Phi + m\zeta}{Qr}\right).$$

The coefficient $a_1(r)$ can be simplified as follows:

$$a_1 = \frac{1}{r} + \frac{Q}{\Phi}\frac{d}{dr}\left(\frac{\Phi}{Q}\right) + \frac{m\zeta}{r\Phi} - \frac{2m\Omega}{r\Phi},$$

$$a_1 = \frac{1}{r} + \frac{1}{\Phi}\frac{d\Phi}{dr} + Q\frac{d}{dr}\left(\frac{1}{Q}\right) + \frac{m\zeta}{r\Phi} - \frac{2m\Omega}{r\Phi},$$

$$a_1 = \frac{1}{r} - \left(\frac{1}{Q}\frac{dQ}{dr}\right) + \frac{m}{r\Phi}\left(\zeta + \frac{r}{m}\frac{d\Phi}{dr} - 2\Omega\right).$$

We know that $d\Phi/dr = -md\Omega/dr$, therefore:

$$a_1 = \frac{1}{r} - \left(\frac{1}{Q}\frac{dQ}{dr}\right) + \frac{m}{r\Phi}\left(\zeta - r\frac{d\Omega}{dr} - 2\Omega\right).$$

We also, from the definition of the vorticity (2.33), know that $\zeta = rd\Omega/dr + 2\Omega$.

$$\therefore a_1 = \frac{1}{r} - \frac{Q'}{Q}.$$

Finally, the coefficient $a_2(r)$ can be expanded as:

$$a_2 = \left[\frac{\Delta}{\Phi^2}\left(\frac{m^2}{r^2} - \frac{k^2\Phi^2}{N^2 - \Phi^2}\right) - \frac{2m\Omega}{r^2\Phi} - \frac{2m^2\Omega\zeta}{r^2\Phi^2} + \frac{Q}{\Phi}\frac{d}{dr}\left(\frac{\Phi + m\zeta}{Qr}\right)\right].$$

Here, note that $2\Omega\zeta = (\Delta + \Phi^2)$. This ultimately allows us to express a_2 as:

$$a_2 = \left[-\frac{k^2}{N^2 - \Phi^2}\Delta - \frac{m^2}{r^2} + \frac{1}{\Phi}\left\{\frac{1}{r}\frac{d\Phi}{dr} + \frac{m}{r}\frac{d\zeta}{dr} - \frac{2m\Omega}{r^2} + mQ\zeta\left(\frac{1}{rQ}\right)'\right\} + Q\left(\frac{1}{rQ}\right)'\right]$$

We can substitute in that $d\Phi/dr = -md\Omega/dr$:

$$a_2 = \left[-\frac{k^2}{N^2 - \Phi^2}\Delta - \frac{m^2}{r^2} + \frac{m}{\Phi}\left\{\frac{1}{r}\frac{d\zeta}{dr} - \frac{1}{r}\frac{d\Omega}{dr} - \frac{2\Omega}{r^2} + Q\zeta\left(\frac{1}{rQ}\right)'\right\} + Q\left(\frac{1}{rQ}\right)'\right]$$

We also have the following equivalence from the definition of the vorticity:

$$-\frac{1}{r}\frac{d\Omega}{dr} - 2\frac{\Omega}{r^2} = -\frac{\zeta}{r^2}.$$

$$\implies a_2 = \left[-\frac{k^2}{N^2 - \Phi^2}\Delta - \frac{m^2}{r^2} + \frac{mrQ}{\Phi}\left\{ \frac{1}{r^2 Q}\frac{d\zeta}{dr} - \frac{\zeta}{r^3 Q} + \frac{\zeta}{r}\left(\frac{1}{rQ}\right)' \right\} + Q\left(\frac{1}{rQ}\right)' \right].$$

Let us define the quantity in the curly brackets as q_1:

$$q_1 = \left\{ \frac{1}{r^2 Q}\frac{d\zeta}{dr} - \frac{\zeta}{r^3 Q} + \frac{\zeta}{r}\left(\frac{1}{rQ}\right)' \right\}.$$

We can simplify q_1 as follows:

$$q_1 = \left\{ \frac{1}{r^2 Q}\frac{d\zeta}{dr} + \zeta\left(\frac{1}{r}\left(\frac{1}{rQ}\right)' - \frac{1}{r^3 Q} \right) \right\}$$

$$q_1 = \left\{ \frac{1}{r^2 Q}\frac{d\zeta}{dr} + \zeta\left(\frac{1}{r^2 Q}\right)' \right\}$$

$$q_1 = \left(\frac{\zeta}{r^2 Q}\right)'$$

Substituting q_1 back into a_2 yields:

$$a_2 = \left[-\frac{k^2}{N^2 - \Phi^2}\Delta - \frac{m^2}{r^2} + \frac{mrQ}{\Phi}\left(\frac{\zeta}{r^2 Q}\right)' + Q\left(\frac{1}{rQ}\right)' \right]$$

Therefore, in (A.14) we have:

$$\frac{d^2 u}{dr^2} + \left[\frac{1}{r} - \frac{Q'}{Q}\right]\frac{du}{dr} + \left[-\frac{k^2}{N^2 - \Phi^2}\Delta - \frac{m^2}{r^2} + \frac{mrQ}{\Phi}\left(\frac{\zeta}{r^2 Q}\right)' + Q\left(\frac{1}{rQ}\right)' \right] u = 0, \tag{A.15}$$

This is the combined inviscid equation as stated by Park and Billant [2013].

B Spectral Methods with Chebyshev Polynomials

For the range $-1 \leq x \leq 1$, the Chebyshev polynomials of the first kind $\mathcal{T}_n$ can be defined with the following trigonometric identity:

$$\mathcal{T}_n(x) = \cos\left(n \cos^{-1} x\right). \tag{B.1}$$

Here we have n as an integer such that $n \geq 0$. The series can alternatively be written as:

$$\mathcal{T}_0 = 1, \quad \mathcal{T}_1 = x, \quad \mathcal{T}_2 = 2x^2 - 1, \quad \mathcal{T}_{n+1} = 2x\mathcal{T}_n - \mathcal{T}_{n-1}. \tag{B.2}$$

Differentiation of the Chebyshev polynomials has the following rule:

$$2\mathcal{T}_n = \frac{\mathcal{T}'_{n+1}}{n+1} - \frac{\mathcal{T}'_{n-1}}{n-1} \quad \text{for} \quad n > 1. \tag{B.3}$$

We also have the Gauss-Lobatto quadrature points, spaced throughout the range $[-1, 1]$:

$$x_j = \cos\left(\pi j / M\right). \tag{B.4}$$

Here i and M are both integers, with i ranging from 0 to M, and $M + 1$ being the total number of points. For these points the following identity holds: $\mathcal{T}_n\left(x_j\right) = \cos\left(nj\pi/M\right)$.

We can use the Chebyshev polynomials to perform spectral expansion on any continuously differentiable function of one real variable, such as $y(x)$, defined over the range $-1 \leq x \leq 1$. The expansion presents itself as an infinite summation over the Chebyshev polynomials, each with a distinct expansion coefficient $\tilde{y}_n$:

$$y(x) = \sum_{n=0}^{\infty} \tilde{y}_n \mathcal{T}_n(x). \tag{B.5}$$

B.1 Collocation matrix

For computational ease, we make two approximations. The first approximation is to truncate the summation after N terms. Note that in the main text of this thesis we label the number of terms as T, to avoid confusion with the buoyancy frequency. Due to the exponential accuracy exhibited by the series, larger values of N will result in better and better approximations of $y(x)$. This exponential accuracy relies upon $y(x)$ being continuously differentiable, as was declared above. Higher degrees of accuracy for larger N is also seen for finite difference methods, however the accuracy for finite difference methods is merely algebraic and not exponential.

The second approximation is to restrict the summation to only being evaluated on a set of collocation points spaced throughout the range of x. These collocation points are chosen to be the same as the Gauss-Lobatto quadrature points of (B.4). These approximations yield a revised form of the Chebyshev summation series:

$$y(x_j) = \sum_{n=0}^{N} \tilde{y}_n \mathcal{T}_n(x_j). \tag{B.6}$$

The expression $\mathcal{T}_n(x_j)$ can be interpreted as a matrix ϕ_{jn}, such that $y(x_j) = \sum_{n=0}^{N} \phi_{jn}\tilde{y}_n$. In this sense, the matrix ϕ_{jn} is a collocation matrix, acting on the expansion coefficients $\tilde{y}_n$ to produce the values of y at the collocation points x_j. The collocation matrix has dimensions $(M+1) \times (N+1)$, and each term obeys the following formula (deduced from the properties of the Gauss-Lobatto quadrature points):

$$\phi_{jn} = \mathcal{T}_n(x_j) = \cos\left(jn\pi/M\right). \tag{B.7}$$

(Note that, unlike standard matrix notation, the indices here range from zero up to their maximum value, i.e. we have $j \in [0, M]$ and $n \in [0, N]$.)

When applying a collocation matrix to a boundary value problem, it may sometimes be required to omit the top and bottom rows of the matrix, which correspond to the collocation points at the boundaries, and replace them with rows that represent the boundary conditions.

B.2 Differentiation matrix

Consider $dy/dx \equiv y'(x)$. As a spectral expansion, this can be written in two equivalent forms:

$$y'(x) = \sum_{n=0}^{\infty} \tilde{y}'_n \mathcal{T}_n(x) = \sum_{n=0}^{\infty} \tilde{y}_n \mathcal{T}'_n(x). \tag{B.8}$$

We begin with expanding the first form, i.e. $y'(x) = \sum_{n=0}^{\infty} \tilde{y}'_n \mathcal{T}_n(x)$. Making use of (B.3), we can write:

$$y'(x) = \tilde{y}'_0 \mathcal{T}_0 + \tilde{y}'_1 \mathcal{T}_1 + \sum_{n=2}^{\infty} \frac{\tilde{y}'_n}{2} \left(\frac{\mathcal{T}'_{n+1}}{n+1} - \frac{\mathcal{T}'_{n-1}}{n-1} \right),$$

$$\implies y'(x) = \tilde{y}'_0 + \tilde{y}'_1 x + \sum_{n=3}^{\infty} \frac{\tilde{y}'_{n-1}}{2} \frac{\mathcal{T}'_n}{n} - \sum_{n=1}^{\infty} \frac{\tilde{y}'_{n+1}}{2} \frac{\mathcal{T}'_n}{n},$$

$$\implies y'(x) = \tilde{y}'_0 + \tilde{u}'_1 x - \frac{1}{2}\tilde{y}'_2 - \tilde{y}'_3 x + \sum_{n=3}^{\infty} \left(\tilde{y}'_{n-1} - \tilde{y}'_{n+1} \right) \frac{\mathcal{T}'_n}{2n}. \tag{B.9}$$

By comparing (B.9) to the second part of (B.8), we can conclude that, for $n \geq 3$:

$$2n\tilde{y}_n = \tilde{y}'_{n-1} - \tilde{y}'_{n+1}.$$

If we assume that this identity holds for $n = 2$ and check the case for $n = 1$, we can further conclude that the following identity holds for all n:

$$2n\tilde{y}_n = c_{n-1}\tilde{y}'_{n-1} - \tilde{y}'_{n+1}, \qquad c_n = (1 + \delta_{0k}). \tag{B.10}$$

(Here introducing the Kronecker delta δ_{ij} which is equal to 1 if both indices are equal, and 0 otherwise.)

Rearranging (B.10) and applying it recursively allows us to conclude the following infinite summation series for $\tilde{y}'_n$:

$$\tilde{y}'_n = \frac{2}{c_n} \sum_{\substack{m=n+1, \\ m+n=\text{odd}}}^{\infty} m\tilde{y}_m.$$

Relying upon the exponential accuracy of spectral methods, we can truncate this series after N terms so that the summation can be applied to a series of truncated Chebyshev coefficients. Also, as before with the collocation matrix, this formula can be written as a matrix equation, introducing the differentiation matrix D_{mn}. This yields:

$$\tilde{y}'_m = \sum_{n=0}^{N} D_{mn}\tilde{y}_n. \tag{B.11}$$

Here D_{mn} is a square matrix of size $(N+1) \times (N+1)$ with the following properties:

$$D_{mn} = \begin{cases} 0 \quad \text{if} \quad (m \geq n) \text{ or } (m+n) \text{ is even,} \\ n \quad \text{if} \quad (m = 0) \text{ and } (m < n) \text{ and } (m+n) \text{ is odd,} \\ 2n \quad \text{if} \quad (m > 0) \text{ and } (m < n) \text{ and } (m+n) \text{ is odd.} \end{cases} \tag{B.12}$$

(Note that, as before with the collocation matrix, the indices here range from zero up to their maximum value, i.e. we have $m \in [0, N]$ and $n \in [0, N]$.)

Since the differentiation matrix is square, it can be applied multiple times to derive the expansion coefficients of higher derivatives. In this way, D_{mn} and ϕ_{jm} can be used together upon $\tilde{y}_n$ to derive the values of the qth derivative $y^{(q)}(x_j)$ at the collocation points:

$$\tilde{y}^{(q)}(x_j) = \sum_{m=0}^{N} \sum_{n=0}^{N} \phi_{jm} D_{mn}^{(q)} \tilde{y}_n. \tag{B.13}$$

Here $D_{mn}^{(q)}$ is the differentiation matrix applied to itself q times. $D_{mn}^{(0)}$ is equivalent to the identity matrix I_{mn}.

C The Kelvin Waves of Dual-Wave-Mode SRI

Kelvin waves are travelling neutral wave-modes moving parallel and adjacent to boundaries in a rotating system. They exhibit exponential decay of amplitude as one moves away from the boundary [Thomson, 1880].

Dual-wave-mode SRI has been described as a Kelvin wave instability by Yavneh et al. [2001], working in the inviscid narrow-gap near-solid-body limit. For a derivation of the viscous form of this limit, see equations (7.18)-(7.22) from section 7.2. The inviscid form can then be attained by letting $Re^* \to \infty$ and dropping the no-slip boundary conditions, yielding:

$$-i\Phi u - 2v = -\frac{dP}{dx}, \tag{C.1}$$

$$-i\Phi v + (2-\beta)\, u = -ik_y P, \tag{C.2}$$

$$-i\Phi w = -ik_z P - \rho, \tag{C.3}$$

$$-i\Phi \rho - N^2 w = 0, \tag{C.4}$$

$$\frac{du}{dx} + ik_y v + ik_z w = 0. \tag{C.5}$$

We also have (setting $\sigma_r = 0$ for neutral waves):

$$\Phi = f^* + k_y \beta x,$$

and the rigid boundary conditions:

$$u(x=0) = u(x=1) = 0.$$

C.1 Shallow water limit

To explore how Kelvin waves would develop in this system, we first need to take the shallow water limit. Rearranging (C.4) for w and substituting into (C.3) yields:

$$-\frac{\Phi^2 \rho}{N^2} = -ik_z P - \rho. \tag{C.6}$$

For the shallow water limit, we make the approximation that $\Phi^2/N^2 \ll 1$, and hence that

$$-ik_z P - \rho = 0. \tag{C.7}$$

This replaces (C.3) in the above system of equations.

C.2 Kelvin mode

Kelvin waves move parallel to the boundaries, and hence have no radial velocity; i.e. $u(x) = 0$. Substituting this into the shallow water system yields:

$$-2v = -\frac{dP}{dx}, \tag{C.8}$$

$$-i\Phi v = -ik_y P, \tag{C.9}$$

$$-ik_z P - \rho = 0, \tag{C.10}$$

$$ik_y v + ik_z w = 0. \tag{C.11}$$

We can derive the following equation for the pressure perturbation, from substituting (C.9) for v into (C.8):

$$2\frac{k_y P}{\Phi} = \frac{dP}{dx}, \tag{C.12}$$

We can also derive a dispersion relation for the Kelvin mode. Using (C.9) and (C.4) to substitute for v and w in (C.5) yields:

$$\frac{k_y^2 P}{\Phi} - \frac{ik_z \Phi \rho}{N^2} = 0.$$

Now using (C.10) to eliminate ρ we get:

$$\frac{k_y^2 P}{\Phi} - \frac{\Phi k_z^2 P}{N^2} = 0,$$

$$\implies \Phi = \pm \frac{k_y}{k_z} N. \tag{C.13}$$

Note that, since Φ is a function of x, (C.13) implies we cannot have $u = 0$ exactly. However, close to each boundary the $u = 0$ assumption approximates the actual behaviour.

Since Φ is a function which grows with x, if there are two wave-like regions then we expect $\Phi < 0$ adjacent to the inner boundary $x = 0$ and $\Phi > 0$ adjacent to the outer boundary $x = 1$. (See appendix D for why we expect two wave-like regions.)

We expect to see exponential decay of perturbation amplitudes as one moves away from either boundary; hence for $P = P_0 \exp(-\gamma x)$ we expect to see $\gamma > 0$ near $x = 0$ and $\gamma < 0$ near $x = 1$. We can verify this using (C.12):

$$2\frac{k_y P}{\Phi} = \frac{dP}{dx} = -\gamma P,$$

$$\implies \gamma = -2\frac{k_y}{\Phi}. \tag{C.14}$$

For $k_y > 0$, this means that γ will always have the opposite sign to Φ. Hence, choosing (as expected) the negative root for Φ on the inner boundary yields exponential decay of amplitude away from the boundary, as required. The same holds for choosing the positive root for Φ on the outer boundary.

Thus Kelvin waves can occur in the inviscid narrow-gap near-solid-body stratified Taylor-Couette system adjacent to either boundary, and have oppositely signed Lagrangian frequencies at each boundary.

The instability mechanism of dual-wave-mode SRI further requires that these Kelvin waves have approximately the same $[k_y, k_z]$-wavenumbers and frequency f^*. Labelling the inner and outer frequencies as $[f_1^*, f_2^*]$ and making use of $f^* = \Phi - k_y\beta x$ from the start of this appendix, we have:

$$f_1^* = \Phi_- = -\frac{k_y}{k_z}N, \qquad f_2^* = \Phi_+ - k_y\beta = \frac{k_y}{k_z}N - k_y\beta.$$

We can therefore achieve $f_1^* \approx f_2^*$ through suitable choice of k_z, such that:

$$k_z \approx \frac{2N}{\beta}.$$

This can be seen to approximately hold in table 7.1.

D Instability Conditions of Park and Billant [2013]

In this appendix we will show the working of Park and Billant [2013] in deriving the instability conditions for the inviscid dual-wave-mode SRI.

D.1 Derivation

Consider the combined inviscid equation (2.48):

$$\frac{d^2u}{dr^2} + \left[\frac{1}{r} - \frac{Q'}{Q}\right]\frac{du}{dr} + \left[-\frac{k^2}{N^2-\Phi^2}\Delta - \frac{m^2}{r^2} + \frac{mrQ}{\Phi}\left(\frac{\zeta}{r^2Q}\right)' + Q\left(\frac{1}{rQ}\right)'\right]u = 0,$$

$$Q(r) = \frac{m^2}{r^2} - \frac{k^2\Phi^2}{N^2-\Phi^2}, \quad \Delta(r) = 2\zeta\Omega - \Phi^2.$$

Using a WKBJ method, and making the assumption that $k \gg 1$, the solution to this equation can be approximated by [Bender and Orszag, 1978]:

$$u_r = \frac{Q^{1/2}}{r^{1/2}\gamma^{1/4}}\left[A_+ \exp\left(ik\int_{r_t}^{r}\sqrt{\gamma(t)}\mathrm{d}t\right) + A_- \exp\left(-ik\int_{r_t}^{r}\sqrt{\gamma(t)}\mathrm{d}t\right)\right], \quad \text{(D.1)}$$

$$\gamma = \frac{\Phi^2 - 2\zeta\Omega}{N^2-\Phi^2}.$$

Here $A_\pm$ are constants and r_t is a turning point for which $\gamma(r_t) = 0$. Positive values of γ correspond to wave-like regions of the mode, whereas negative values of γ correspond to regions that are either exponentially growing or decaying with radius.

If $|N| > \left|\sqrt{2\zeta\Omega}\right|$ for all $r_1 < r < r_2$, and $\mu < \eta^2$, then there will be two distinct regions in the $[f, r]$-parameter space where $\gamma > 0$ and the solutions are wave-like. We define five lines in this parameter space: $f_{N\pm} = m\Omega \pm N$, $f_\pm = m\Omega \pm \sqrt{2\zeta\Omega}$, and $f_c = m\Omega$. These lines, and the two wave-like regions, are shown in figure D.1. For a given frequency, each of these lines can be related to the Lagrangian frequency $\Phi(r)$.

(i) The lines $f = f_{N\pm}$ denote where $\Phi = \pm N$.

(ii) The lines $f = f_\pm$ denote where $\Phi = \pm\sqrt{2\zeta\Omega}$. Wave-like regions, which require $\gamma > 0$, exist between the lines $f_{N\pm}$ and $f_\pm$.

(iii) The line $f = f_c$ denotes where the real component of Φ changes sign, and the sign of Φ controls the direction that the waves propagate in when compared to the basic state flow.

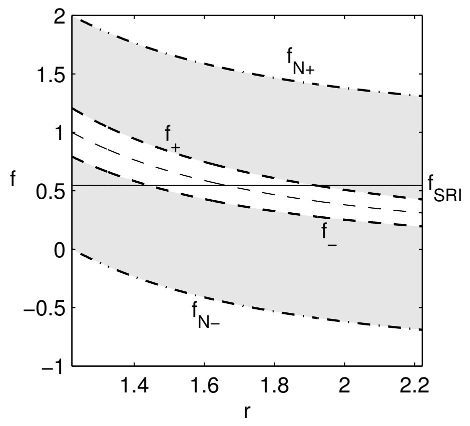

Figure D.1: The lines $f_{N\pm}$ (dot-dashed) and $f_\pm$ (dashed) are plotted for $\eta = 0.55$, $\mu = 0.31$, $m = 1$, and $N = 1.0$. Also plotted is the line f_c (thin dashed line, unlabelled) at which the real part of Φ changes sign. Shaded regions represent where $\gamma > 0$. The constant line $f = f_{SRI} = 0.546$ gives an example frequency for which both regions of positive γ exist. For this frequency, $\Phi(r_c) = 0$ occurs at $r_c = 1.66$, $\Phi(r_-) = -\sqrt{2\zeta\Omega}$ occurs at $r_- = 1.44$, and $\Phi(r_+) = +\sqrt{2\zeta\Omega}$ occurs at $r_+ = 1.92$. Note that this figure correlates with figure 4.2 which uses the same parameters.

Since the line $f = f_c$ is always between the two wave-like regions, then the two wave-like regions always propagate in opposite directions compared to the basic state flow. (In the lab frame, the two wave-modes always move together.)

Figure D.1 specifically shows an example where it is possible for a single modal frequency to pass through both wave-like regions. In this context, the flow exhibits wave-like behaviour adjacent to the cylinder walls, and a region of evanescent behaviour away from the walls where $\gamma < 0$. Note that this is only possible with values of $[\eta, \mu, N]$ which satisfy equations (4.1) and (4.2). Park and Billant [2013] showed that the dispersion relation when this occurred could always be made unstable.

Dispersion relation

The dispersion relation for a frequency which passes through both wave-like regions is: [Park and Billant, 2013]

$$\left(K\left(r_1, r_{t1}\right) + i\alpha\right)\left(K\left(r_{t2}, r_2\right) + i\alpha\right) = \left(1 - \alpha^2\right) K\left(r_1, r_{t1}\right) K\left(r_{t2}, r_2\right), \tag{D.2}$$

$$\alpha = \frac{4 + X\left(r_{t1}, r_{t2}\right)}{4 - X\left(r_{t1}, r_{t2}\right)},$$

with

$$K\left(r_a, r_b\right) = \exp\left(2ik\int_{r_b}^{r_a}\sqrt{\gamma\left(t\right)}\mathrm{d}t\right), \quad X\left(r_a, r_b\right) = \exp\left(-2k\int_{r_b}^{r_a}\sqrt{-\gamma\left(t\right)}\mathrm{d}t\right).$$

Here r_{t1} and r_{t2} correspond to the radial turning points at which $\gamma = 0$, and the frequency is equal to f_+ and f_- respectively.

The approximation is then made that $X\left(r_{t1}, r_{t2}\right) \ll 1$, and hence that $\alpha \simeq 1$. X is made small since the exponent is negative in the evanescent region; however this approximation could potentially break down if the evanescent region was sufficiently small, or if $\sqrt{-\gamma} \simeq 0$ throughout the region.

The small parameter $\epsilon = \sqrt{X\left(r_{t1_0}, r_{t2_0}\right)}$ is defined, with α expanded as $\alpha = 1 + \epsilon^2/2 + O\left(\epsilon^4\right)$. Note that r_{t1_0} and r_{t2_0} represent the radial turning points evaluated at leading order in ϵ.

We now make use of the complex frequency $\omega = i\sigma = f + i\sigma_r$. The complex frequency ω and the wavenumber k are expanded out as:

$$\begin{aligned} \omega &= \omega_0 + \epsilon\omega_1 + \epsilon^2\omega_2 + \ldots \\ k &= k_0 + \epsilon k_1 + \epsilon^2 k_2 + \ldots \end{aligned} \tag{D.3}$$

At leading order with this approximation, the dispersion relation reduces to:

$$\left(K\left(r_1, r_{t1}\right) + i\right)\left(K\left(r_{t2}, r_2\right) + i\right) = 0.$$

This is satisfied by either $K\left(r_1, r_{t1}\right) = -i$ or $K\left(r_{t2}, r_2\right) = -i$. These two cases correspond to neutral waves propagating around the inner and outer cylinders respectively. These can be satisfied simultaneously with the appropriate choice of ω_0 and k_0, which are both real. With this choice, the dispersion relation is also satisfied at $O(\epsilon)$.At $O(\epsilon^2)$ we have:

$$\left[k_1 h\left(r_1, r_{t1}\right) + k_0\omega_1 h_\omega\left(r_1, r_{t1}\right)\right]\left[k_1 h\left(r_{t2}, r_2\right) + k_0\omega_1 h_\omega\left(r_{t2}, r_2\right)\right] = \frac{1}{4}, \tag{D.4}$$

with:

$$h(r_a, r_b) = \int_{r_a}^{r_b}\sqrt{\gamma_0}dt, \quad h_\omega(r_a, r_b) = \int_{r_a}^{r_b}\frac{\partial\sqrt{\gamma_0}}{\partial\omega}dt,$$

$$\gamma_0 = \frac{\Phi_0^2 - 2\zeta\Omega}{N^2 - \Phi_0^2}, \quad \Phi_0 = \omega_0 - m\Omega.$$

Equation (D.4) can be solved to give ω_1 as:

$$\begin{aligned} \omega_1 = &-\frac{k_1}{2k_0}\left(\frac{h\left(r_1, r_{t1}\right)}{h_\omega\left(r_1, r_{t1}\right)} + \frac{h\left(r_{t2}, r_2\right)}{h_\omega\left(r_{t2}, r_2\right)}\right) \\ &\pm\frac{1}{2k_0}\sqrt{\left(\frac{h\left(r_1, r_{t1}\right)}{h_\omega\left(r_1, r_{t1}\right)} - \frac{h\left(r_{t2}, r_2\right)}{h_\omega\left(r_{t2}, r_2\right)}\right)^2 k_1^2 + \frac{1}{h_\omega\left(r_1, r_{t1}\right) h_\omega\left(r_{t2}, r_2\right)}}. \end{aligned} \tag{D.5}$$

It is important to note that:

$$\frac{\partial\sqrt{\gamma_0}}{\partial\omega} = \frac{-\Phi_0\left(2\zeta\Omega - N^2\right)}{\sqrt{\gamma_0}\left(N^2 - \Phi_0^2\right)^2}.$$

We stated earlier that Φ_0 changes sign between the two regions of positive γ; this means that $\partial\sqrt{\gamma_0}/\partial\omega$ has the opposite sign in each region. We can therefore conclude that the quantity $h_\omega\left(r_1, r_{t1}\right) h_\omega\left(r_{t2}, r_2\right)$ is always negative.

This means that ω_1 can be made imaginary by choosing $k_1 = 0$, which yields a real growth rate that can be positive and therefore an unstable mode. It is therefore a sufficient condition for instability that a single modal frequency be able to pass through both wave-like $\gamma > 0$ regions.

D.2 Establishing Instability Conditions

We have established that a sufficient condition for inviscid instability is that, at a single frequency, two wave-like regions exist at the inner and outer boundaries, with an evanescent region in between.

For this to be possible, the $\gamma > 0$ regions must exist within the $[f, r]$-parameter space, and be adjacent to each cylinder. This requirement implies that (A) max$(f_{N-}) <$ max$\left(f_-\right)$ and (B) min$(f_+) <$ min$\left(f_{N+}\right)$.

To guarantee that both regions exist for a single value of the frequency f, we require that (C) max$(f_-) >$ min$\left(f_+\right)$. Finally, to guarantee that this frequency can begin in one region and end in another without crossing either of the lines $f_{N\pm}$, we also require that (D) min$(f_{N+}) >$ max$\left(f_{N-}\right)$.

Note that the maxima and minima of all of these functions are always at either $r = r_1$ or $r = r_2$.

First Condition for Instability

For the case $\mu < 1$, we can state (A) as $f_{N-}(r_1) < f_-(r_1)$, i.e.:

$$m - N < m - 2\sqrt{A},$$

$$\implies N > 2\sqrt{A},$$

$$\implies 2\sqrt{\frac{\mu - \eta^2}{1 - \eta^2}} < N.$$

Here we have recovered (4.1) for the case $\mu < 1$.

We can also state (B) as $f_+(r_2) < f_{N+}(r_2)$, i.e.:

$$m\mu + N > m\mu + 2\sqrt{\mu A},$$

$$\implies N > 2\sqrt{\mu A}.$$

It can therefore be concluded that (B) is satisfied for $\mu < 1$ if (A) is satisfied.

For the case $\mu > 1$, we can state (A) as $f_{N-}(r_2) < f_-(r_2)$, i.e.:

$$m\mu - N < m\mu - 2\sqrt{\mu A},$$

$$\implies N > 2\sqrt{\mu A},$$

$$\implies 2\sqrt{\frac{\mu\left(\mu - \eta^2\right)}{1 - \eta^2}} < N.$$

Here we have recovered (4.1) for the case $\mu > 1$.

We can also state (B) as $f_+(r_1) < f_{N+}(r_1)$, i.e.:

$$m + N > m + 2\sqrt{A},$$

$$\implies N > 2\sqrt{A}.$$

As before, it can be concluded that (B) is satisfied for $\mu > 1$ if (A) is satisfied.

Second Condition for Instability

Let us consider (C) for the case $\mu < 1$. In this case, we can state (C) as $f_-(r_1) > f_+(r_2)$, i.e.:

$$m\mu + 2\sqrt{\mu A} < m - 2\sqrt{A},$$

$$\implies 2\sqrt{A}(1+\sqrt{\mu}) < m(1-\mu),$$

$$\implies \frac{2}{1-\sqrt{\mu}}\sqrt{\frac{\mu-\eta^2}{1-\eta^2}} < m.$$

Here we have recovered the lower bound on m from (4.2) for the case $\mu < 1$.

Let us now re-consider (C) for the case $\mu > 1$. Here we can state (C) as $f_-(r_2) > f_+(r_1)$, i.e.:

$$m + 2\sqrt{A} < m\mu - 2\sqrt{\mu A},$$

$$\implies 2\sqrt{A} + 2\sqrt{\mu A} < m(\mu - 1),$$

$$\implies 2\sqrt{A}(\sqrt{\mu}+1) < m(\mu-1),$$

$$\implies 2\sqrt{\frac{\mu-\eta^2}{1-\eta^2}}\left(\frac{\sqrt{\mu}+1}{\mu-1}\right) < m,$$

$$\implies \frac{2}{\sqrt{\mu}-1}\sqrt{\frac{\mu-\eta^2}{1-\eta^2}} < m.$$

Here we have recovered the lower bound on m from (4.2) for the case $\mu > 1$.

Now let us consider (D) for the case $\mu < 1$, for which we can express (D) as $f_{N+}(r_2) > f_{N-}(r_1)$, i.e.:

$$m - N < m\mu + N,$$

$$\implies m < \frac{2N}{1-\mu}.$$

Here we have recovered the upper bound on m from (4.2) for the case $\mu < 1$.

Re-considering (D) for the case $\mu > 1$, we have $f_{N+}(r_1) > f_{N-}(r_2)$, i.e.:

$$m\mu - N < m + N,$$

$$\implies m(\mu - 1) < 2N,$$

$$\implies m < \frac{2N}{\mu - 1}.$$

Here we have recovered the upper bound on m from (4.2) for the case $\mu > 1$.

We can therefore state the second condition for instability for any $\mu \neq 1$ as:

$$\frac{2}{|1-\sqrt{\mu}|}\sqrt{\frac{\mu-\eta^2}{1-\eta^2}} < m < \frac{2N}{|1-\mu|}.$$

This is equation (4.2).

E Conditions for instability if $\mu < 1$ and $N < 2$

In this appendix we will show that equations (4.1) and (4.3) can be rearranged to give sufficient conditions for instability on η and μ for any given N in the range $0 < N < 2$. The case $N \geq 2$ is shown to always be unstable in section 4.2.1. We restrict ourselves to the range $\eta^2 < \mu < 1$, since $\mu < \eta^2$ is known to be unstable to inviscid axisymmetric modes. This work can be considered to be an extension of Park and Billant [2013].

We repeat equations (4.1) and (4.3) here for ease of reading. Both are expressed for the case $\mu < 1$:

$$2\sqrt{\frac{\mu - \eta^2}{1 - \eta^2}} < N,$$

$$\frac{2}{1 - \sqrt{\mu}}\sqrt{\frac{\mu - \eta^2}{1 - \eta^2}} + 1 < \frac{2N}{1 - \mu}.$$

Reversible Operations upon Inequalities

In the following analysis we will be individually manipulating each of the two equations above, in order to find a set of conditions upon η and μ for which the equations are mutually satisfied. To this end, all operations performed on the inequalities are intended to be fully reversible. We will therefore here review the set of reversible operations that can be performed on an inequality.

Addition or subtraction of any quantity to both sides of an inequality requires no adjustment of the inequality sign, and is therefore a reversible operation. Multiplication through by a positive quantity also requires no adjustment of the inequality sign and is therefore reversible. Multiplication by a negative quantity merely requires that the direction of the inequality sign be switched, and is nonetheless a reversible operation.

Squaring both sides of an inequality, or taking the positive square-root, is more complicated. If both sides of the inequality can be shown to be positive, then neither of these two operations requires any adjustment of inequality sign, and therefore either operation is reversible by applying the other operation. If both sides of the inequality can be shown to be negative, then one can first multiply through by -1, switching the inequality sign as mentioned above, to reach the case where both sides of the inequality are positive, and operations of squaring or rooting are applicable and reversible.

If one of side of the inequality is positive whereas the other side is negative, then squaring or rooting operations cannot be performed. However, in this context it is clearly possible to tell whether or not the inequality has been satisfied. If reversible operations have been used to reach such a point, then this will reveal either a necessary or sufficient condition for the original inequality to be satisfied.

E.1 First Condition for Instability

We have equation (4.1):

$$2\sqrt{\frac{\mu-\eta^2}{1-\eta^2}} < N.$$

This can be squared since the both sides are demonstrably positive:

$$\frac{\mu-\eta^2}{1-\eta^2} < \frac{N^2}{4}.$$

Since $(1-\eta^2) > 0$, we can write :

$$\mu < \mu_0, \quad \text{with } \mu_0 \text{ defined as:} \quad \mu_0 = \eta^2 + \frac{1-\eta^2}{4}N^2. \tag{E.1}$$

This is our first condition for instability on μ.

Second Condition for Instability

Rearranging (4.3) is considerably more involved. We have:

$$\frac{2}{1-\sqrt{\mu}}\sqrt{\frac{\mu-\eta^2}{1-\eta^2}} + 1 < \frac{2N}{1-\mu}.$$

Subtracting 1 from both sides, and then multiplying through by $\left(1-\sqrt{\mu}\right)/2$ (positive in our chosen domain) yields:

$$\sqrt{\frac{\mu-\eta^2}{1-\eta^2}} < \frac{N}{1+\sqrt{\mu}} - \frac{1-\sqrt{\mu}}{2}. \tag{E.2}$$

Since $\mu > \eta^2$ and $\eta^2 < 1$, we can guarantee that the LHS of (E.2) is positive. Therefore we can conclude the following weaker but necessary condition for instability on μ:

$$\begin{aligned} 0 &< \frac{N}{1+\sqrt{\mu}} - \frac{1-\sqrt{\mu}}{2}, \\ \implies 0 &< \frac{N}{1-\mu} - \frac{1}{2}, \\ \implies \mu &> 1 - 2N. \end{aligned} \tag{E.3}$$

Note that this inequality is automatically satisfied if $N \geq 1/2$, since we have already declared that $\mu > 0$.

If (E.3) is false then the system is stable with respect to the dual-wave-mode SRI. If (E.3) holds true however, then both sides of (E.2) are positive, and we can square both sides of the condition:

$$\frac{\mu - \eta^2}{1-\eta^2} < \left(\frac{N}{1+\sqrt{\mu}} - \frac{1-\sqrt{\mu}}{2}\right)^2 .$$

$$\implies 1 - \frac{1-\mu}{1-\eta^2} < \frac{N^2}{\left(1+\sqrt{\mu}\right)^2} + \frac{\left(1-\sqrt{\mu}\right)^2}{4} - \frac{1-\sqrt{\mu}}{1+\sqrt{\mu}} N.$$

We now multiply through by $4\left(1-\eta^2\right)\left(1+\sqrt{\mu}\right)^2$. This is a positive quantity, so the inequality sign is not affected:

$$\begin{aligned} 4\left(1-\eta^2\right)(1+\sqrt{\mu})^2 - 4(1-\mu)(1+\sqrt{\mu})^2 &< \dots \\ \dots 4N^2\left(1-\eta^2\right) - 4N(1-\mu)\left(1-\eta^2\right) + \left(1-\eta^2\right)(1-\mu)^2 . \end{aligned}$$

We can now collect the equation in terms of $(1-\eta^2)$, yielding:

$$\begin{aligned} 4(1-\mu)(1+\sqrt{\mu})^2 &> \dots \\ \dots - \left(1-\eta^2\right)\left[4N^2 - 4N(1-\mu) - 4(1+\sqrt{\mu})^2 + (1-\mu)^2\right] . \end{aligned} \tag{E.4}$$

Let us rewrite (E.4) as $4(1-\mu)\left(1+\sqrt{\mu}\right)^2 > (1-\eta^2)\, f_1$, with f_1 defined as:

$$f_1 = -\left[4N^2 - 4N(1-\mu) - 4(1+\sqrt{\mu})^2 + (1-\mu)^2\right] .$$

The LHS of (E.4) is guaranteed to be positive for $\eta^2 \leq \mu < 1$, as is the quantity $(1-\eta^2)$. Therefore if $f_1 \leq 0$ then (E.4) is automatically satisfied. However, if $f_1 > 0$, then (E.4) must be consulted further to ascertain the condition for instability.

We can factorise f_1 as follows:

$$\begin{aligned} f_1 = -\left(\sqrt{\mu} - 1 + \sqrt{2\,(2-N)}\right)\left(\sqrt{\mu} - 1 - \sqrt{2\,(2-N)}\right) \\ \times\left(\sqrt{\mu} + 1 + i\sqrt{2N}\right)\left(\sqrt{\mu} + 1 - i\sqrt{2N}\right). \end{aligned} \tag{E.5}$$

For $\eta^2 < \mu < 1$ with real μ, then $\eta < \sqrt{\mu} < 1$, and $\sqrt{\mu}$ is also real. Therefore in our chosen range, f_1 only changes sign when $\sqrt{\mu} = \sqrt{\mu}_1 = 1 - \sqrt{2\,(2-N)}$.

Note also that for $\mu \to 1$, we have $f_1 = -\left(4N^2 - 16\right) = 4\left(4 - N^2\right)$. Therefore for $0 < N < 2$, then $f_1(\mu \to 1) > 0$. This allows us to conclude the following:

$$\begin{aligned} f_1 > 0 \quad \text{for} \quad \sqrt{\mu_1} < \sqrt{\mu} < 1, \\ f_1 \leq 0 \quad \text{for} \quad \sqrt{\mu} \leq \sqrt{\mu}_1. \end{aligned} \tag{E.6}$$

Returning to (E.4), we have the form $4\,(1-\mu)\left(1+\sqrt{\mu}\right)^2 > \left(1-\eta^2\right) f_1$. If $f_1 \leq 0$ this is automatically satisfied. Therefore, our second condition for instability is satisfied if $\sqrt{\mu} \leq \sqrt{\mu}_1$.

If $\sqrt{\mu_1} < \sqrt{\mu} < 1$, then $f_1 > 0$. Dividing both sides of (E.4) by f_1 and rearranging yields:

$$\eta^2 > \frac{1}{f_1}\left[f_1 - 4\,(1-\mu)\,(1+\sqrt{\mu})^2\right].$$

Defining $f_2 = f_1 - 4\,(1-\mu)\left(1+\sqrt{\mu}\right)^2$, this can be written as:

$$\frac{f_2}{f_1} < \eta^2. \tag{E.7}$$

We know that f_1 and η^2 are both positive, which means (E.7) is automatically satisfied if $f_2 \leq 0$. If $f_2 > 0$ then we can take the square root of both sides to proceed. We can factorise f_2 as follows:

$$\begin{aligned} f_2 = \frac{1}{3}\left(\sqrt{\mu} + 1 - \sqrt{2N}\right)\left(\sqrt{\mu} + 1 + \sqrt{2N}\right) \\ \times\left(3\sqrt{\mu} + 1 + \sqrt{2\,(2-3N)}\right)\left(3\sqrt{\mu} + 1 - \sqrt{2\,(2-3N)}\right). \end{aligned} \tag{E.8}$$

Note that for $\mu \to 1$, we have $f_2(\mu \to 1) = 17 - 4N - (2N-1)^2$. Therefore for $0 < N < 2$, we have $f_2(\mu \to 1) > 0$.

We also now define the following quantities where f_2 changes sign:

$$\begin{aligned}\sqrt{\mu}_2 &= \left(-1+\sqrt{2\,(2-3N)}\right)/3,\\ \sqrt{\mu}_3 &= \sqrt{2N}-1,\\ \sqrt{\mu}_4 &= -\sqrt{2N}-1,\\ \sqrt{\mu}_5 &= \left(-1-\sqrt{2\,(2-3N)}\right)/3.\end{aligned} \tag{E.9}$$

Note that $\sqrt{\mu}_4 < 0$ and $\sqrt{\mu}_5 < 0$ for all N. Both terms are therefore outside the range $\eta < \sqrt{\mu} < 1$ and can be ignored.

However $\sqrt{\mu}_2 > 0$ if $N < 1/2$, and $\sqrt{\mu}_3 > 0$ if $N > 1/2$. Therefore f_2 will change sign at either $\sqrt{\mu} = \sqrt{\mu}_2$ or $\sqrt{\mu} = \sqrt{\mu}_3$, depending on whether $N < 1/2$ or $1/2 < N$ respectively. For the case $N = 1/2$, f_2 will only change sign at $\sqrt{\mu} = 0$; however, since we have declared that $0 < \eta < \sqrt{\mu}$, in that context we have $f_2 > 0$ throughout our chosen domain.

We can therefore conclude the following set of conditions on the sign of f_2:

$$f_2(\mu)\begin{cases}\text{If } \left(N < \frac{1}{2}\right) \text{ then } \begin{cases}\sqrt{\mu_2} < \sqrt{\mu} < 1 \implies f_2 > 0,\\ \eta < \sqrt{\mu} \leq \sqrt{\mu_2} \implies f_2 \leq 0.\end{cases}\\ \text{If } \left(N = \frac{1}{2}\right) \text{ then } f_2 > 0 \text{ for } \eta < \sqrt{\mu} < 1,\\ \text{If } \left(N > \frac{1}{2}\right) \text{ then } \begin{cases}\sqrt{\mu_3} < \sqrt{\mu} < 1 \implies f_2 > 0,\\ \eta < \sqrt{\mu} \leq \sqrt{\mu_3} \implies f_2 \leq 0.\end{cases}\end{cases} \tag{E.10}$$

From (E.7), if $f_2 \leq 0$, then our second condition for instability is satisfied, whereas if $f_2 > 0$ then our second condition for instability is only satisfied if:

$$\sqrt{\frac{f_2}{f_1}} < \eta. \tag{E.11}$$

E.2 Summary

We now have a set of conditions on η and μ which determine whether a stratified flow with buoyancy frequency N is unstable to dual-wave-mode SRI. The following equations make up the relevant set of conditions: (E.1), (E.3), (E.6), (E.10), (E.11).

For a summary of how these conditions fit together, see figure 4.3. As part of these conditions we've defined the following quantities:

$$\begin{aligned}
\mu_0 &= \eta^2 + \left(\frac{1-\eta^2}{4}\right) N^2, \\
\sqrt{\mu}_1 &= 1 - \sqrt{2\left(2-N\right)}, \\
\sqrt{\mu}_2 &= \frac{1}{3}\left(-1 + \sqrt{2\left(2-3N\right)}\right), \\
\sqrt{\mu}_3 &= -1 + \sqrt{2N}, \\
f_1 &= -\left[4N^2 - 4N\left(1-\mu\right) - 4\left(1+\sqrt{\mu}\right)^2 + \left(1-\mu\right)^2\right], \\
f_2 &= 3\mu^2 + 8\mu\sqrt{\mu} - 2\left(2N-3\right)\mu - \left(2N-1\right)^2.
\end{aligned}$$

Bibliography

C. D. Andereck, S. S. Liu, and H. L. Swinney. Flow regimes in a circular Couette system with independently rotating cylinders. *Journal of Fluid Mechanics*, 164:155–183, 1986.

S. A. Balbus and J. F. Hawley. A powerful local shear instability in weakly magnetized disks. I-Linear analysis. II-Nonlinear evolution. *The Astrophysical Journal*, 376:214–233, 1991.

G. K. Batchelor. *An introduction to fluid dynamics*. Cambridge University Press, 1991.

C. M. Bender and S. A. Orszag. *Advanced mathematical methods for scientists and engineers*. McGraw-Hill, 1978.

J. P. Boyd. *Chebyshev and Fourier Spectral Methods*. Dover, 2001.

A. Brandenburg and B. Dintrans. Nonaxisymmetric stability in the shearing sheet approximation. *Astron. Astrophys.*, 450:437–444, 2006.

C. Canuto, M. Y. Hussaini, A. Quarteroni, and T. A. Zang. *Spectral Methods: Fundamentals in Single Domains*. Scientific Computing. Springer, 2006.

S. Chandrasekhar. *Hydrodynamic and hydromagnetic stability*. Oxford University Press, 1961.

P. G. Drazin and W. H. Reid. *Hydrodynamic stability*. Cambridge University Press, 1981.

B. Dubrulle, L. Marié, C. Normand, D. Richard, F. Hersant, and J. P. Zahn. A hydrodynamic shear instability in stratified disks. *Astron. Astrophys.*, 429:1–13, 2005.

M. Gellert and G. Rüdiger. Stratorotational instability in Taylor-Couette flow heated from above. *Journal of Fluid Mechanics*, 623:375–385, 2009.

D. Gottlieb and S. A. Orszag. *Numerical Analysis of Spectral Methods: Theory and Applications*. SIAM, 1977.

W. Hillebrandt and J. C. Niemeyer. Type Ia supernova explosion models. *Annual Review of Astronomy and Astrophysics*, 38(1):191–230, 2000.

R. Ibanez, H. L. Swinney, and B. Rodenborn. Observations of the stratorotational instability in rotating concentric cylinders. *Physical Review Fluids*, 1(5):053601, 2016.

P. J. Kushner, M. E. McIntyre, and T. G. Shepherd. Coupled Kelvin-wave and mirage-wave instabilities in semigeostrophic dynamics. *J. Phys. Oceanogr.*, 28:513–518, 1998.

M. Le Bars and P. Le Gal. Experimental analysis of the stratorotational instability in a cylindrical Couette flow. *Phys. Rev. Lett.*, 99,(064502), 2007.

S. Le Dizès and P. Billant. Radiative instability in stratified vortices. *Physics of Fluids*, 21(9):096602, 2009.

S. Le Dizès and X. Riedinger. The strato-rotational instability of Taylor-Couette and Keplerian flows. *Journal of Fluid Mechanics*, 660:147–161, 2010.

C. Leclercq, F. Nguyen, and R. R. Kerswell. Connections between centrifugal, stratorotational, and radiative instabilities in viscous Taylor-Couette flow. *Physical Review E*, 94(4):043103, 2016.

M. J. Molemaker, J. C. McWilliams, and I. Yavneh. Instability and equilibrium of centrifugally stable stratified Taylor-Couette flow. *Phys. Rev. Lett.*, 86(23):5270–5273, 2001.

C. Normand. Finite gap effects on the instability of stratified circular Couette flow. *European Journal of Mechanics-B/Fluids*, 29(3):192–200, 2010.

K. Ooyama. On the stability of the baroclinic circular vortex: A sufficient condition for instability. *J. Atmos. Sci.*, 23:43–53, 1966.

G. Oster. Density gradients. *Scientific American*, 213:70–76, 1965.

J. Park and P. Billant. The stably stratified Taylor-Couette flow is always unstable except for solid-body rotation. *Journal of Fluid Mechanics*, 725:262–280, 2013.

Lord Rayleigh. On the dynamics of revolving fluids. *Proceedings of the Royal Society of London. Series A*, 93(648):148–154, 1917.

X. Riedinger, S. Le Dizès, and P. Meunier. Viscous stability properties of a Lamb-Oseen vortex in a stratified fluid. *Journal of Fluid Mechanics*, 645:225–278, 2010.

X. Riedinger, S. Le Dizès, and P. Meunier. Radiative instability of the flow around a rotating cylinder in a stratified fluid. *Journal of Fluid Mechanics*, 672:130–146, 2011.

G. Rüdiger and D. A. Shalybkov. Stratorotational instability in MHD Taylor-Couette flows. *Astronomy & Astrophysics*, 493(2):375–383, 2009.

G. Rüdiger, T. Seelig, M. Schultz, M. Gellert, C. Egbers, and U. Harlander. The stratorotational instability of taylor-couette flows with moderate reynolds numbers. *Geophysical & Astrophysical Fluid Dynamics*, pages 1–19, 2017.

D. Shalybkov and G. Rüdiger. Stability of density-stratified viscous Taylor-Couette flows. *Astron. Astrophys.*, 438:411–417, 2005.

G. I. Taylor. Stability of a viscous liquid contained between two rotating cylinders. *Philosophical Transactions of the Royal Society of London. Series A*, 223:289–343, 1923.

W. Thomson. 1. On gravitational oscillations of rotating water. *Proceedings of the Royal Society of Edinburgh*, 10:92–100, 1880.

O. M. Umurhan. On the stratorotational instability in the quasi-hydrostatic semi-geostrophic limit. *Mon. Not. R. Astron. Soc.*, 365:85–100, 2006.

J. Vanneste and I. Yavneh. Unbalanced instabilities of rapidly rotating stratified shear flows. *Journal of Fluid Mechanics*, 584:373–396, 2007.

E. P. Velikhov. Stability of an ideally conducting liquid flowing between rotating cylinders in a magnetic field. *J. Exptl. Theoret. Phys.*, 36:1398–1404, 1959.

I. Yavneh, J. C. McWilliams, and M. J. Molemaker. Non-axisymmetric instability of centrifugally stable stratified Taylor-Couette flow. *Journal of Fluid Mechanics*, 448: 1–21, 2001.